

Modification and Application of Gold Nanorods in Surface Enhanced  
Raman Scattering Based Assays

by  
Shereen Abdelhakeim Tawfik Elbayomy

A thesis submitted in partial fulfillment of the requirements for the degree  
Of

Doctor of Philosophy

Department of Chemistry  
University of Alberta

© Shereen Abdelhakeim Tawfik Elbayomy, 2015

## Abstract

Surface enhanced Raman scattering (SERS) is an ultrasensitive vibrational spectroscopic technique to detect molecules on or near the surface of plasmonic nanoparticles. More recently, this technique has been used to design novel nanoprobe named “SERS labels” that combine metallic nanoparticles and specific organic Raman reporter molecules. Such SERS labels can be conjugated to capture probes of biological molecules to be used to indirectly sense the target biological molecules by using laser Raman spectroscopy. Various metal nanoparticles act as a Raman signal amplifier for engineering of nanoprobe. In general, their size, geometry, chemical composition, and surface chemistry can influence the Raman enhancement ability.

Recently, interest in gold nanorods (GNRs) has increased, as they possess unique optical and electronic properties. Many of the targeted applications for GNRs require their surface modification, but it can often be a challenge due to their cetyltrimethylammonium bromide (CTAB) coating, which is a stabilizing agent used during GNR synthesis. The work presented in Chapter 2 of this thesis explored spectroscopic and electronic microscopy characterization of GNRs after CTAB replacement with a mixed thiolate layer of a Raman reporter such as 4-nitrobenzenethiol (tNB) and 2-(2-{2-[2-(2-[2-(11-mercapto-undecyloxy)-ethoxy]-ethoxy)-ethoxy]-ethoxy}-ethoxy)-ethoxy-acetic acid (HSC<sub>11</sub>(EO)<sub>6</sub>-COOH). This HSC<sub>11</sub>(EO)<sub>6</sub>-COOH linker provides; steric stability

through hydrophobic alkyl chain; water solubility due to presence of an ethoxy moiety that improves ligand exchange in aqueous solution; and anchor points such as carboxylic acid or amino groups for further conjugation with biological molecules. Chapter 3 presents the SERS response of the  $-\text{SC}_{11}(\text{EO})_6\text{-COO}^-/\text{tNB}$  modified GNRs of four different aspect ratios and 30 nm diameter spherical gold nanoparticles, the characteristic Raman spectrum of 4-nitrobenzenethiol was measured for five gold nanoparticle solutions.

The capability of using the  $-\text{SC}_{11}(\text{EO})_6\text{-COO}^-/\text{tNB}$  modified GNRs of aspect ratio 2.4, which were covalently linked to immunoglobulin G (IgG) through terminal-carboxylic acid group of thiolate linker were explored with a chip-based SERS immunoassay in Chapter 4. The sensitivity of SERS based sandwich immunoassay utilizing gold nanorods of aspect ratio 2.4 for goat IgG detection was translated to a limit of detection (LOD) of 15 fM.

The detection and quantification of small metabolite molecules is being targeted as a promising diagnostic method in disease assessment. Chapter 5 in this thesis presents an indirect competitive SERS based assay for the analysis of the thyroid hormone thyroxine in its free form ( $\text{fT}_4$ ). In this assay, we used  $\text{fT}_4$  conjugated SERS labels of GNRs to compete with  $\text{fT}_4$  standard solutions for monoclonal antibody binding sites. Lower levels of free thyroxine than threshold, that accompanies hypothyroidism disease, can be detected and the results were correlated well with the results from a commercial enzyme-linked immunosorbent assay (ELISA) kit.

## **Preface**

This thesis is an original work by Shereen Elbayomy under the supervision of Professor Mark McDermott. No part of this thesis has been previously published.

## **Acknowledgements**

The university of Alberta has been my home for more than five years during my Ph.D. studies. Although, I am glad to move on with my life, I will miss all the remarkable people here in U of A. Finishing my thesis has truly been a milestone, which could not have been achieved without the help of so many great friends and co-workers. Thank you to each every one of you, for all the support and help over the years.

First and foremost, I am grateful to my Ph.D. supervisor, Professor Mark McDermott. Your guidance and help throughout the years in my graduate school has been invaluable. Thank you for your continuous patience and support.

Also, thanks to my fellow group members: Rongbing Du, Greg Kaufman, Ahmed Mahmoud, Sunil Rajput, Kenny Xu, and Albert Cao. You guys have always been available help and advice. Special thanks to a few former group members; Lars Laurentius, Ibrahim Bushnak, Ni Yang, and Cici Cao, for all help in early years of my graduate studies, when I desperately needed help getting started with my research.

In addition, I would like to thank all the staff in the Department of Chemistry and at National Institute for Nanotechnology (NINT) for their assistance over the years. Special thanks to Anita Weiler, Lynne Lechelt, Ryan Lister and Gregory Kiema. Furthermore, thanks to all the staff at the Alberta Centre for Surface Engineering and Science (ACSES) for sample analysis and

data interpretation. I would like to express my gratitude to the following collaborators for their time and effort: Adam Johan Bergren, Rhett Clark, and Gareth Lambkin. Lastly, I am indebted to Jonathan Veinot for providing access to his facilities at Chemistry Department.

Outside the lab and the University, I would like to acknowledge a few close friends who support me throughout my studies and have continuously provided a life outside academia: Amr Mahmoud and Ensaf Almoni. Thank you for always being there for me.

Last but not least, I am thankful to have such a great family that has supported me over the many years spent at the University of Alberta. The ones close to my heart are my mother, Amal; my dad, Abdelhakeim; my sister; Neveen; and my Kids, Rawaan, Abdelrahman, and Ahmed. Special thanks to my husband, Mohamed; you have kept encouraging me right from the start and all the way to the end. I could not have come this far without your help!

## Table of Contents

---

<b>1</b>	<b>CHAPTER I</b>	<b>1</b>
1.1	GENERAL OVERVIEW AND RESEARCH OBJECTIVES	1
1.2	OPTICAL PROPERTIES OF NOBLE METAL NANOPARTICLES	5
1.3	TYPES OF METAL NANOPARTICLES	8
1.4	GOLD NANOPARTICLES IN BIOLOGICAL SENSING	12
	<i>1.4.1 Label-free LSPR-based biosensing.</i>	13
	<i>1.4.2 Fluorescence quenching biosensing</i>	14
	<i>1.4.3 Electrochemical biosensing utilizing GNPs</i>	14
	<i>1.4.4 SERS biosensing</i>	15
1.5	SURFACE MODIFICATION OF METAL NANOPARTICLES	19
	<i>1.5.1 Preparation of ERLs</i>	23
1.6	MOTIVATIONS AND GOALS	24
<b>2</b>	<b>CHAPTER II</b>	<b>28</b>
2.1	INTRODUCTION	28
2.2	EXPERIMENTAL	32
	<i>2.2.1 Reagents and Materials</i>	32
	<i>2.2.2 Preparation of GNRs as SERS labels</i>	33
	<i>2.2.3 Instrumentation</i>	34
2.3	RESULT AND DISCUSSION	37
	<i>2.3.1 Tracking the replacement of CTAB with <math>-SC_{11}(EO)_6\sim COO^-</math></i>	

<i>and 4-nitrobenzenethiol</i>	38
2.3.2 <i>Sites of exchange</i>	46
2.3.3 <i>Colloidal stability</i>	48
2.3.4 <i>Surface enhanced Raman scattering (SERS)</i>	50
2.4 CONCLUSION	56
<b>3 CHAPTER III</b>	<b>57</b>
3.1 INTRODUCTION	57
3.2 EXPERIMENTAL	60
3.2.1 <i>Reagents and Materials</i>	60
3.2.2 <i>Preparation of GNRs as SERS labels</i>	60
3.2.3 <i>Instrumentation</i>	62
3.3 RESULT AND DISCUSSION	65
3.3.1 <i>Colloidal stability</i>	66
3.3.2 <i>Surface enhanced Raman scattering (SERS) study</i>	69
3.4 CONCLUSION	77
<b>4 CHAPTER IV</b>	<b>79</b>
4.1 INTRODUCTION	79
4.2 EXPERIMENTAL	83
4.2.1 <i>Reagent and Materials</i>	83
4.2.2 <i>Substrate Preparation</i>	84
4.2.3 <i>Preparation of extrinsic Raman labels (ERLS) of GNRs</i>	

4.2.4	<i>Substrate modification</i>	86
4.2.5	<i>Preparation of blank sample</i>	87
4.2.6	<i>Instrumentation</i>	87
4.3	RESULTS AND DISCUSSION	90
4.3.1	<i>Characterization and monitoring of gold nanorods conjugated with anti-goat IgG</i>	90
4.3.2	<i>Further characterization of anti-goat IgG conjugated GNRs performance in SERS-based sandwich immunoassay by scanning electron microscopy (SEM)</i>	100
4.4	CONCLUSION	105
<b>5</b>	<b>CHAPTER V</b>	<b>106</b>
5.1	INTRODUCTION	106
5.2	EXPERIMENTAL	111
5.2.1	<i>Surface enhanced Raman scattering (SERS) study</i>	111
5.2.2	<i>Enzyme-linked immunosorbent assay (ELISA) study</i>	115
5.2.3	<i>Instrumentation</i>	119
5.3	RESULT AND DISCUSSION	120
5.3.1	<i>SERS-based competitive assay study</i>	121
5.3.2	<i>Comparison using indirect competitive ELISA platform</i>	126
5.3.3	<i>Langmuir adsorption isotherm fits for competitive assay responses</i>	128
5.3.4	<i>Colloidal stability of fT<sub>4</sub>-conjugated GNRs</i>	130

5.4	CONCLUSION	136
<b>6</b>	<b>CHAPTER VI</b>	<b>137</b>
6.1	CHAPTER CONCLUSIONS	137
6.2	FUTURE WORK	140

## List of Figures

<b>Figure 1.01</b>	Schematic representation of sandwich and competitive bioassays	2
<b>Figure 1.02</b>	Localized surface plasmon extinction spectra of 40 nm diameter spherical silver and gold NPs	9
<b>Figure 1.03</b>	Schematic representation shows transverse and longitudinal LSPR absorbance of gold nanorod	11
<b>Figure 1.04</b>	Localized surface plasmon extinction spectra of 40 nm gold nanosphere and gold nanorods of three-different aspect ratios	12
<b>Figure 1.05</b>	Schematic illustration of spontaneous self-assembly of thiol ligand on gold surface forming a well-ordered thiolate monolayer	22
<b>Figure 1.06</b>	Schematic illustration of three types of ERLs	25

<b>Figure 2.01</b>	Schematic representation of the two-step procedure proposed to produce SERS labels of GNRs	31
<b>Figure 2.02</b>	High-resolution XPS spectra for Br 3d, N 1s and S 2p peaks collected from the GNR samples before and after modification	41
<b>Figure 2.03</b>	Bright field HRTEM images of CTAB coated GNR, and $-\text{SC}_{11}(\text{EO})_6\text{-COO}^-$ coated GNR	45
<b>Figure 2.04</b>	HRTEM images show atomic structure of the (110) face and (111) end of a single GNR	47
<b>Figure 2.05</b>	UV-visible extinction spectra collected for GNRs, aspect ratio 2.4 before and after modification with $-\text{SC}_{11}(\text{EO})_6\text{-COO}^-$ and tNB and a SEM image of $-\text{SC}_{11}(\text{EO})_6\text{-COO}^-$ /tNB modified GNRs	51
<b>Figure 2.06</b>	SERS spectra on CTAB capped, $-\text{SC}_{11}(\text{EO})_6\text{-COO}^-$ and $-\text{SC}_{11}(\text{EO})_6\text{-COO}^-$ /tNB coated GNRs of aspect ratio 2.4	53

<b>Figure 3.01</b>	Atomic force microscopy (AFM) image of one gold nanorod of aspect ratio 2.4 with line scans are marked across the width of the GNR	64
<b>Figure 3.02</b>	The experimentally measured extinction spectra for citrate capped 30 nm diameter GNPs and GNRs of four-different aspect ratios 2.1, 2.4, 2.8, and 3.2 before and after labeling with tNB in a mixed thiolate layer with $-\text{SC}_{11}(\text{EO})_6\sim\text{COO}^-$	68
<b>Figure 3.03</b>	SEM images show gold nanorods of aspect ratio 2.4 and 2.8	70
<b>Figure 3.04</b>	SERS spectra for 30 nm diameter GNPs and four-different size GNRs of aspect ratios 2.1, 2.4, 2.8 and 3.2 after labeling with tNB in a mixed monolayer with $-\text{SC}_{11}(\text{EO})_6\sim\text{COO}^-$	72
<b>Figure 3.05</b>	Plots of SERS intensity magnitudes of the symmetric stretching of the nitro group at $1337\text{ cm}^{-1}$ versus surface area $\times$ number of	73

particles/mL for 30 nm GNPs and GNRs of four-different aspect ratios 2.1, 2.4, 2.8 and 3.2

- Figure 4.01** Schematic diagram illustrates the preparation of anti-goat IgG modified gold substrate, conjugation of anti-goat IgG to  $-\text{SC}_{11}(\text{EO})_6\sim\text{COO}^-/\text{tNB}$  modified GNRs and SERS sandwich immunoassay platform 89
- Figure 4.02** HRTEM images show  $-\text{SC}_{11}(\text{EO})_6\sim\text{COO}^-$  coated GNRs of aspect ratio 2.4, and anti-goat IgG conjugated GNRs 93
- Figure 4.03** The extinction spectra of  $-\text{SC}_{11}(\text{EO})_6\sim\text{COO}^-/\text{tNB}$  coated GNRs and anti-goat conjugated GNRs of aspect ratio 2.4 95
- Figure 4.04** SERS spectra for tNB were collected from bioassay chips used for detection of different concentration of goat IgG 1, 2, 5, 10, 15, 20 pM, and blank and a magnified SERS spectrum of blank 97

<b>Figure 4.05</b>	SEM images show anti-goat IgG conjugated GNRs of aspect ratio 2.4 used in SERS-based sandwich immunoassay for detection of 1 nM goat IgG at two-different magnifications	98
<b>Figure 4.06</b>	A plot of SERS intensity of the symmetric stretch of the nitro group at $1337\text{ cm}^{-1}$ versus goat IgG concentration (1 pM to 1 nM) and a plot of SERS intensity at $1337\text{ cm}^{-1}$ versus goat IgG concentration from 1 to 20 pM	100
<b>Figure 4.07</b>	SEM image shows anti-goat IgG conjugated GNRs of aspect ratio 2.4 used in a SERS-based sandwich immunoassay for detection of 100 pM goat IgG	103
<b>Figure 4.08</b>	Side view SEM images show anti-goat IgG conjugated GNRs of aspect ratio 2.4 used in a sandwich immunoassay for detection of 1 nM goat IgG at two-different magnifications	105
<b>Figure 5.01</b>	Illustrations show the chemical structure for	109

thyroxine ( $T_4$ ) hormone and changes in free  $T_4$  normal range during hypo or hyper thyroid disorder

- Figure 5.02** Schematic illustration shows preparation of  $fT_4$ -conjugated GNR 115
- Figure 5.03** Schematic diagram shows SERS-based bioassay platform:  $fT_4$ -conjugated GNRs compete with  $fT_4$  standard solution for  $T_4$ -monoclonal antibody binding sites. 117
- Figure 5.04** Schematic diagram shows ELISA indirect competitive assay platform 119
- Figure 5.05** SERS spectra of 4-nitrobenzenethiol collected from SERS-based assay chips and a plot of SERS response versus  $fT_4$  concentration 124
- Figure 5.06** SEM imaging of indirect competitive SERS-based assay utilizing  $fT_4$ -conjugated GNRs 126

<b>Figure 5.07</b>	A plot of absorbance versus $fT_4$ concentration for ELISA assay.	128
<b>Figure 5.08</b>	Plots of $\Delta SERS_{max}/\Delta SERS$ and $\Delta abs_{max}/\Delta abs$ versus $fT_4$ concentrations for competitive SERS-based and ELISA assays, respectively	132
<b>Figure 5.09</b>	Extinction spectra of CTAB coated GNRs and $fT_4$ conjugated Raman labeled GNRs	134
<b>Figure 5.10</b>	SEM image of the $-SC_{11}(EO)_6-NH_2/tNB$ modified GNRs after conjugation with $fT_4$	136

## List of Tables

<b>Table 2.1</b>	XPS atomic concentrations of Br, N, S and O for the CTAB capped GNRs and after CTAB replacement with $-\text{SC}_{11}(\text{EO})_6\sim\text{COO}^-$ and $-\text{SC}_{11}(\text{EO})_6\sim\text{COO}^- / \text{tNB}$	43
<b>Table 2.2</b>	SERS peak frequencies and assignments for 4-nitrobenzenethiol from pure powder and after adsorption on GNRs	55
<b>Table 3.1</b>	Summary of specific characterization measurements for 30 nm spherical GNPs and GNRs of four different aspect ratios	61
<b>Table 3.2</b>	Summary of linear least squares fit equations for 30 nm GNPs and GNRs of four different aspect ratios studied in SERS comparison	77

## List of Abbreviations

a.u.	Arbitrary unit
AFM	Atomic force microscopy
Asym	Asymmetric
BSA	Bovine serum albumin
CCD	Charge coupled device
CE	Chemical enhancement
CTAB	Cetyltrimethylammonium bromide
cts	Counts
DDA	Discrete dipole approximation
DNA	Deoxyribonucleic acid
EDC	N-(3-dimethylaminopropyl)-N'-ethylcarbodiimide
EF	Enhancement factor
EGFR	Epidermal growth factor receptor
ELISA	Enzyme-linked immunosorbent assay
EM	Electromagnetic enhancement
EO	Ethoxy group
ERLs	Extrinsic Raman Labels
fT <sub>4</sub>	Free thyroxine
FWHM	Full-width-half-maximum

GNPs	Gold nanoparticles
GNRs	Gold nanorods
HER2	Human epidermal growth factor receptor
HRP	Horseradish peroxidase
HSC <sub>11</sub> (EO) <sub>6</sub> ~COOH	2-(2-{2-[2-(2-[2-(11-mercapto-undecyloxy)-ethoxy]-ethoxy)-ethoxy]-ethoxy}-ethoxy)-ethoxy-acetic acid
HRTEM	High resolution transmission electron microscopy
Ig	Immunoglobulin
IgE	Immunoglobulin E
IgG	Immunoglobulin G
IR	Infra-red
LBL	Layer-by-layer
LOD	Limit of detection
LSPR	Localized surface plasmon resonance
MB	Methylene blue
mPEG	Methoxypolyethyleneglycol
NHS	N-hydroxysuccinimide
NIR	Near infra-red
NPs	Nanoparticles
PBS	Phosphate buffered saline
PDMS	Polydimethylsiloxane

PEG	Polyethyleneglycol
PVP	Physical vapor deposition
QD	Quantum dots
RIA	Radioimmunoassay
RNA	Ribonucleic acid
SAMs	Self-assembled monolayers
SEM	Scanning electron microscopy
SERS	Surface enhanced Raman scattering
SPR	Surface plasmon resonance
sym	Symmetric
STEM	Scanning transmission electron microscopy
TEM	Transmission electron microscopy
TMB	3, 3', 5, 5'-tetramethylbenzidine
tNB	4-nitrobenzenethiol
UV-vis	Ultraviolet-visible
XPS	X-ray photoelectron spectroscopy

## List of Symbol

$^{\circ}\text{C}$	Degree Celsius
$\text{cm}^{-1}$	Wavenumber
$c$	Speed of light in vacuum
$d$	Adsorbate layer thickness (nm)
Da	Dalton
$E_{loc}$	Local electric field
$E_{inc}^*$	Incident field
$E_o$	Amplitude of incident field
$F(\omega)$	Electromagnetic field enhancement factor
$h$	Planck's constant
$\nu$	Frequency
$k$	Wave vector
$l_d$	Electric field decay length (nm)
$m$	$n/n_m$ (Complex index of refraction of particle / Real index of refraction of surrounding medium)
$n$	Refractive index
$n_{adsorbate}$	Refractive index of adsorbate
$n_{medium}$	Refractive index of medium
$P_i$	Induced dipole polarization
$R^2$	Correlation coefficient

rpm	Revolutions per minute
SD	Standard deviation
w	Weak
$\alpha_i$	Polarizability
$\delta$	Bending
$\Delta\lambda$	Wavelength shift
$\epsilon_1$	Real component of dielectric function
$\epsilon_2$	Imaginary component of the dielectric function
$\epsilon_m$	Dielectric function of the surrounding medium
$\lambda_{\max}$	Absorption band maximum
$\sigma_{\text{abs}}$	Absorbance cross section
$\sigma_{\text{ext}}$	Extinction cross section
$\sigma_{\text{sca}}$	Scattering cross section
$\nu$	Stretching
$\nu_s$	Symmetric stretching
V	$4/3 \pi r^3$
$\omega$	Angular frequency

# 1 Chapter I

---

## Introduction

### 1.1 General Overview and Research Objectives

The detection of biological molecules plays a fundamental role in biomedical science.<sup>1,2</sup> Bioassay techniques dominate the market for protein and small molecule assays. Assay kits utilize antibodies designed to selectively bind to the target analytes. Typically, the traditional competitive assay scheme will consist of a plate onto which the antibody probe is immobilized and the sample of interest is passed over the plate surface along with an aliquot of labeled target analyte, the sample and the labeled standard will compete for the binding site of the capture probe. Another approach uses a sandwich assay platform that consists of a plate onto which the capture probe is immobilized and another probe that is linked to a label, both probes will sandwich the target analyte (Figure 1.01). The types of labels used includes radiochemical (radioimmunoassay, RIA)<sup>3</sup>, enzyme (enzyme-linked immunosorbent assay, ELISA)<sup>4</sup>, fluorophore<sup>5</sup> or noble metal nanoparticles (NPs) in surface enhanced Raman scattering (SERS) based assay.<sup>6</sup> ELISA is typically carried out on a microtiter plate, allowing for multiple analyses to be carried out simultaneously. The capability of a small number of enzymes to catalyze large amounts of substrate has afforded ELISA detection limits in the picomolar range. The good sensitivity, and wide applicability to most analytes have made ELISA the “gold standard” in biomolecule detection.<sup>7,8</sup>

Nevertheless, researchers have investigated other sensing schemes in hope of simplifying the assay and employing more stable labels. One such alternative replaces the enzyme label with fluorophore exploiting fluorescence detection, but also here drawbacks involving susceptibility of fluorophore to photobleaching and detection requires expensive instrumentation.<sup>8</sup> The drive towards new labels has been accelerated with the applications of nanoparticles.

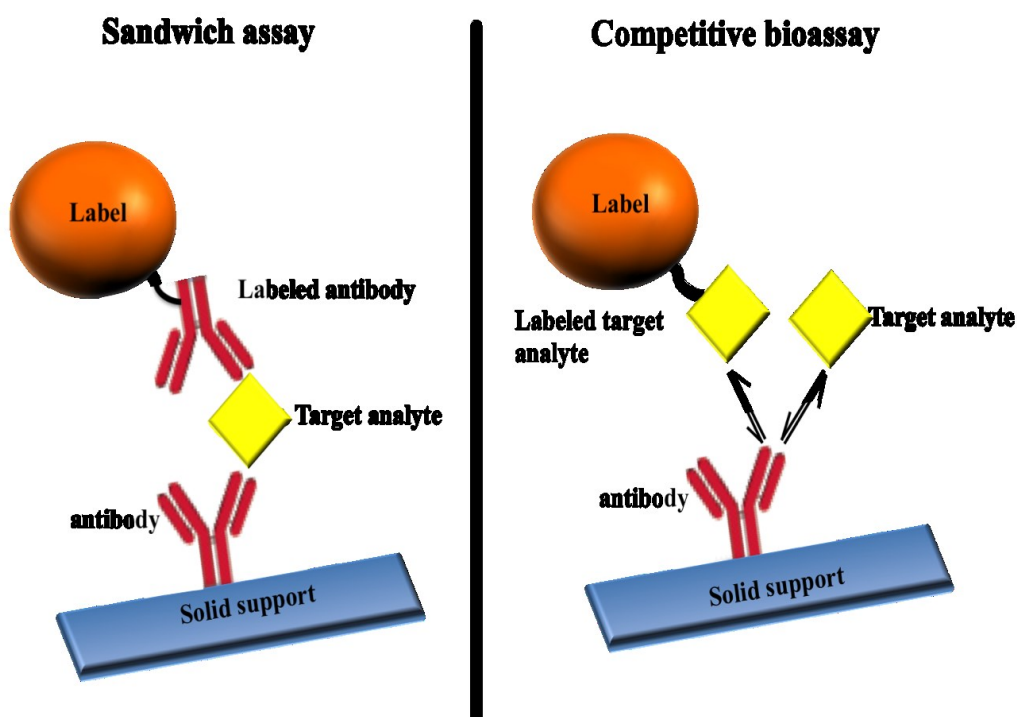


**Figure 1.01.** Schematic representation of sandwich and competitive bioassays.

Nanoparticles have generated a great deal of interest as potential building blocks for biosensing.<sup>2</sup> Gold and silver NPs are of particular interest, as they

feature unique optical properties that can be of great utility in creating new recognition and transduction processes for biological sensors, such as a phenomenon called localized surface plasmon resonance (LSPR).<sup>9-13</sup> This phenomenon refers to the oscillation of conduction electrons over the surface of the metal NP induced by the absorption of visible light. These properties can be readily tuned by varying their size, shape, and the surrounding chemical environment.<sup>14</sup> In addition, gold nanoparticles (GNPs) provide high surface to volume ratio and offer a suitable platform for multi-functionalization with a wide range of organic or biological ligands for selective binding and detection of biological targets.<sup>15, 16</sup>

In the past decade of research, the advent of GNPs as a sensory element has provided a broad spectrum of innovative approaches for detection of small molecules,<sup>17</sup> protein,<sup>18</sup> nucleic acids,<sup>19</sup> and cancer cells<sup>20</sup> rapidly and efficiently. Recently, the merits of surface-enhanced Raman scattering (SERS) as a rapid, sensitive tool for biosensing have been reported.<sup>21</sup> The basis of SERS relies on the use of roughened metal surfaces to amplify scattering and observed enhancement was up to  $10^{14}$  times.<sup>22, 23</sup> Laser excitation on or off resonance with LSPR band of GNPs significantly influences electromagnetic fields, which are generated at the GNP surface.<sup>24</sup> SERS takes advantage of these localized electric fields for signal enhancement of molecules adsorbed in close proximity to the GNP surface. Currently, gold nanorods (GNRs) have a great deal of interest due to their anisotropic shape, presence of corners and a tunable longitudinal LSPR

band.<sup>25</sup> Although the GNRs are an excellent candidate for SERS,<sup>26</sup> the strategies employed in the functionalization of high cross-section Raman reporter molecules for maximum SERS enhancement is still a challenge due to the presence of a densely packed bilayer of cetyltrimethylammonium bromide (CTAB).<sup>27</sup> The CTAB is a structure-directing agent that is used during the synthesis of GNRs and is difficult to replace during the functionalization of GNRs without consequent aggregation of GNRs.

This chapter will introduce the relevant subject areas that are vital to the understanding of the optical properties of the GNPs including gold nanorods in particular, their surface modification and application in biosensors. The first aspect of my work focuses on functionalization of GNRs for biosensing applications using SERS-based assays. We are introducing a rational design of GNRs coated with a mixed thiolate layer of Raman reporter and stabilizing linker, which provides terminal functional groups for further conjugation with biological molecules, this design will be characterized with different techniques in Chapter 2. The SERS efficiency of GNRs with four-different aspect ratio and 30 nm diameter spherical gold nanoparticles (GNPs) suspended in solutions will be investigated in Chapter 3.

Another aspect of my research aims to design SERS based immunoassays that utilize functionalized GNRs (Chapter 2) as extrinsic Raman labels (ERLs). In Chapter 4, A SERS based sandwich immunoassay for detection of goat immunoglobulin G (IgG) utilizing GNRs as ERLs will be presented and the

detection limit of goat IgG will be investigated. Lastly, an indirect competitive SERS-based assay for detection of small metabolite molecule such as free thyroxine (fT<sub>4</sub>) utilizing ERLs of fT<sub>4</sub>-conjugated GNRs will be discussed in Chapter 5. My goal is that the ideas brought forward by this thesis will provide new insights in the design of SERS-based biosensor development.

## **1.2 Optical properties of noble metal nanoparticles**

Faraday is credited with developing the initial understanding of GNPs in 1857, although colloidal gold has been used since the 4<sup>th</sup> century to make a Lycurgus cup, which changes color depending on the direction of light.<sup>28</sup> Later gold NPs were used in stained glass windows of cathedrals throughout Europe, providing a vivid characteristic red color. The past couple of decades have witnessed an exponential growth of scientific reports detailing the synthesis, study of the optical, electrical and other physical properties of new nanoparticles of different sizes and shapes, the surface modification of nanoparticles and their incorporation into different applications. The major driving force behind the use of NPs in biosensing is their unique optical properties resulting from LSPR effects.<sup>29, 30</sup> These effects result in extremely high absorption and scattering (extinction) of light. The molar extinction coefficients of gold NPs are several orders of magnitude higher than organic dyes and outperform fluorescent molecules as well, thus exhibiting promising applications as labels.<sup>31</sup>

In 1908 Gustav Mie formulated an approach derived from Maxwell's equations to predict the influence of electromagnetic radiation on colloids.<sup>32</sup>

When light interacts with a particle the likelihood of an interaction taking place is summed up in the extinction cross section  $\sigma_{\text{ext}}$ , which is made up of two terms, namely  $\sigma_{\text{abs}}$  (absorbance) and  $\sigma_{\text{sca}}$  (scattering), as shown by equation 1-01.

$$\sigma_{\text{ext}} = \sigma_{\text{abs}} + \sigma_{\text{sca}} \quad (1-01)$$

The extinction cross section can be calculated from equation 1-02


$$\quad (1-02)$$

Close examination of the expression for  $\sigma_{\text{ext}}$  in equation 1.02 reveals that the extinction cross section is dependent on the particle volume ( $V$ ), the complex dielectric function of the particle ( $\epsilon_1$  and  $\epsilon_2$ ), and the real dielectric function of the surrounding medium ( $\epsilon_m$ ). The dependence on  $V$  implies that larger nanoparticles have a higher extinction cross section and result in greater absorption/scattering of light.

However, solving Maxwell's equations accurately for particles other than spheres is numerically tedious.<sup>33</sup> The difficulty is especially serious for NPs with sharp points because of strong field gradients. In parallel, a number of theoretical approaches have been developed such as the discrete dipole approximation (DDA) to study extinction and Raman enhancement for NPs of arbitrary shape.<sup>34</sup> In 1973, DDA method was originally proposed by Purcell and Pennypac, and has been extensively applied in the astrophysics community in application to the extinction spectra of grains in interstellar medium.<sup>35</sup> A particularly useful implementation of this method has been developed by Draine and co-workers.<sup>36</sup>

<sup>37</sup> In the DDA, the object of interest is represented as a cubic array of  $N$  polarizable elements. The response of this array to an applied electromagnetic field is then described by self-consistently determining the induced dipole moment in each element. The induced dipole polarization  $P_i$  in each element is determined from equation 1-03

$$P_i = \alpha_i \cdot E_{loc}(r_i) \quad (1-03)$$

Where  $\alpha_i$  and  $r_i$  are the polarizability and location of the  $i$ th dipole, and  $E_{loc}$  is the local electric field. The local electric field at each dipole  $E_{loc,i}$  is given by equation 1-04



$$\quad (1-04)$$

Where  $E_o$  and  $k=\omega/c$  is amplitude and wave vector of the incident field, respectively, and  $A$  is an interaction matrix. By solving a number of complex linear equations, polarization vectors are calculated, and with these, extinction cross sections ( $\sigma_{ext}$ , equation 1.-05), local fields and Raman enhancement can be calculated.<sup>38</sup>



$$\quad (1-05)$$

Where  $E_{inc}^*$  is an incident field. The electromagnetic contribution to the SERS intensity can be determined by evaluating the local field  $E_{loc,i}(\omega)$  on the exposed surfaces of each of the cubes using equation 1-06. The electromagnetic field

enhancement factor  $F(\omega)$  is then determined by averaging the square of  $E_{loc,i}$  over the exposed surfaces, and normalizing by the incident field



(1-06)

### 1.3 Types of metal nanoparticles

Gold and silver spherical NPs are the most widely used biosensor labels. The LSPR absorption band for both silver and gold spherical NPs is found between 400-600 nm, and red shifts with increasing particle size.<sup>39, 40</sup> Figure 1.02 shows the extinction spectra for spherical silver and gold spherical NPs of the same size (40 nm diameter) and an image of their colloidal solutions. The yellowish color for silver colloidal solution indicates absorbance of light at shorter wavelength in the visible spectrum compared to gold spherical NPs that yield a red colored solution. The extinction spectra of 40 nm silver and gold spherical NPs exhibit LSPR peaks at 415 and 533 nm, respectively.

The size of both gold and silver spherical NPs<sup>41, 42</sup> plays a crucial role in SERS signal enhancement ability.<sup>43, 44</sup> The intensity of the electromagnetic (EM) field is strongly dependent on the number of electrons excited and, thus, on the volume of the nanoparticles.<sup>45</sup> It should be noted that using a particle that is too large (>250 nm diameter) is not appropriate because the increased size results in larger radiation damping effects, decreasing the SERS enhancement factor. The

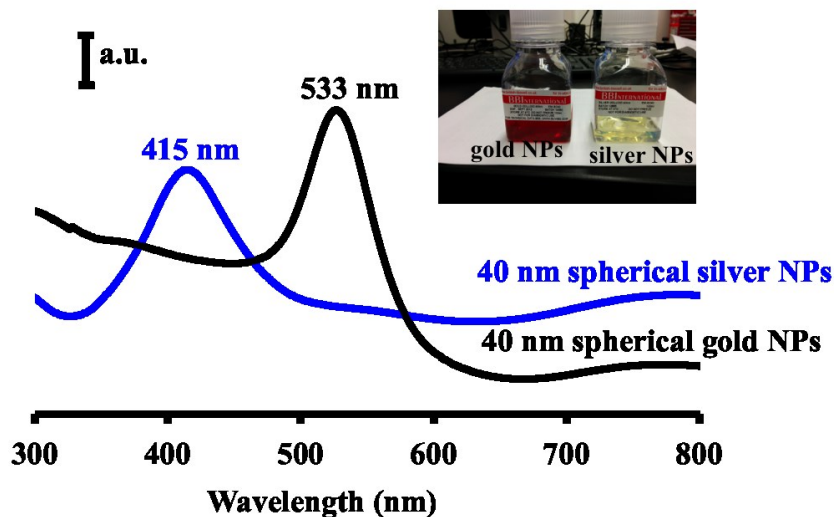


**Figure 1.02.** Localized surface plasmon extinction spectra of 40 nm diameter spherical silver and gold NPs. The spectra were offset for clarity.

optimum size range is 30-100 nm.<sup>46</sup> The LSPR effect is influenced not only by size but also by solvent, ligand, temperature, and interparticle distance.<sup>47, 48</sup>

Generally, silver NPs are much more efficient Raman signal-enhancing material and give rise to SERS signals that are 10-fold to 100-fold higher than those for similar sized spherical GNPs.<sup>45</sup> The choice of NP is affected by other factors beside its SERS capability. For instance, silver NPs have poor biocompatibility and limiting their use in living cells, short-term stability preventing practical utilization in real applications.<sup>49</sup> Hence, silver is often difficult to be substituted for gold in designing SERS labels, especially those for living species labeling. Typically, spherical gold NPs are synthesized by the reduction of  $\text{HAuCl}_4$  with citrate acid as described by Frens.<sup>50</sup> This method for

synthesizing spherical NPs has many advantages, including having an easily controlled size distribution and long-term stability. Therefore, basic studies or biosensing applications are usually carried out by using spherical GNPs.<sup>51, 52</sup>

GNRs exhibit two LSPR bands: a weak transverse band in the visible region with a position similar to that of spherical GNPs that corresponds to electron oscillations along the short axis and a strong longitudinal band at longer wavelengths that corresponds to electron oscillation along the long axis.<sup>53</sup> These bands are depicted in Figure 1.03. The longitudinal LSPR can be engineered by changing the GNR ratio of length (l) to width (d), which is called the aspect ratio (l/d).<sup>54</sup> By simply varying the silver nitrate concentration which is used as a growth directing agent during the growth process of GNRs, the longitudinal LSPR shifts from the visible to the NIR region as the rod's aspect ratio increases from 2.4 to 3.2 as shown in Figure 1.04.<sup>55</sup> Besides, GNRs have a high theoretical extinction coefficient that is more than an order of magnitude higher than that of a nanoshell<sup>56</sup> and approximately 20 times greater for nanorods compared to nanospheres.<sup>57</sup> These advantages have driven GNRs to be used in bioapplications, including tumor detection,<sup>58</sup> molecular and cell imaging,<sup>59</sup> and photothermal therapy.<sup>60</sup> Furthermore, the aspect ratio plays an important role in the Raman enhancement effect. The SERS signal of 4-mercaptopyridine physisorbed on the GNR surface can be maximized by plasmon resonance with excitation wavelength, effectively optimizing contributions from the localized electric field for a given aspect ratio.<sup>61</sup>

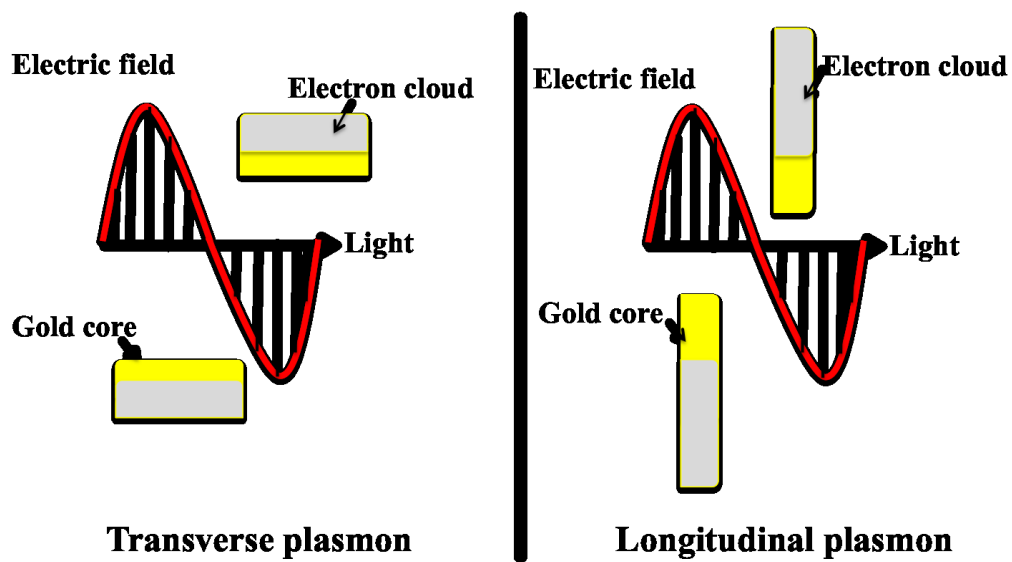


**Figure 1.03.** Schematic representation shows transverse and longitudinal LSPR absorbance of gold nanorod.

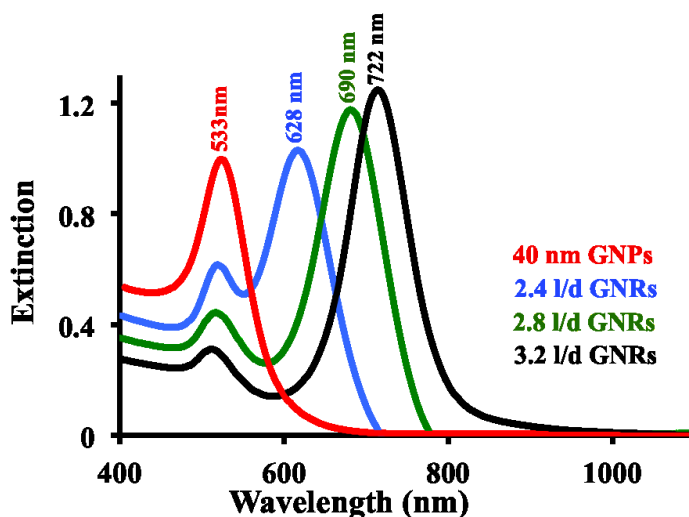


**Figure 1.04.** Localized surface plasmon extinction spectra of 40 nm spherical gold NPs and GNRs of three-different aspect ratios ( $l/d = 2.4, 2.8$  and  $3.2$ ).

#### 1.4 Gold nanoparticles in biological sensing

In the past decade, there has been an increasing number of scientific reports detailing the modification of nanoparticles and their incorporation into bioassays.<sup>62-64</sup> At the forefront, the application of spherical GNPs has continuously received attention, and several reviews are dedicated to these noble metal nanoparticles.<sup>14, 62, 64</sup> Potential applications of GNPs in biosensing have required the design of a new class of nanomaterials commonly known as bio-nanoparticle conjugates. Formation of bio-nanoparticle conjugates by immobilization protocols was first demonstrated in 1990s with enzyme-conjugate gold nanoparticles.<sup>65</sup> Different approaches have been reported towards GNP surface modification and conjugation with a variety of biological molecules such

as nucleic acids,<sup>66</sup> enzymes,<sup>67</sup> antibodies<sup>68</sup> and others. The details of biomolecule conjugation to NPs will be covered in section 1.5.

#### *1.4.1 Label-free LSPR-based biosensing.*

Recently, LSPR-based biosensors have been developed to complement surface plasmon resonance (SPR) sensors.<sup>69</sup> The LSPR peak wavelength of noble metal nanoparticles is sensitive to their surface-bound molecules and the surrounding environment. There are several research areas that utilize this sensitivity in LSPR sensing that typically consist of NPs immobilized on a substrate such as a glass slide and serve as a sensing platform to detect binding events by monitoring the extent of  $\lambda_{\max}$  shift.<sup>70-73</sup> A UV-vis spectrophotometer is normally employed to measure the LSPR extinction spectrum of GNPs. Another type of LSPR sensor can be fabricated simply by suspending NPs in a solution to form a solution phase LSPR sensor. In this format, the aggregation of GNPs of appropriate sizes (diameter > 3.5 nm) induces inter-particle surface plasmon coupling, resulting in a visible color change from red to blue at nanomolar concentrations that can be readily monitored by conventional UV/vis spectrophotometry.<sup>74</sup> Many LSPR sensors using metal nanospheres have been developed for detection of large molecules, such as DNA and proteins.<sup>11, 75</sup> However, detection of small organic molecules based on LSPR sensors is still a challenge because the dielectric constant changes induced by small molecules are much lower than that by large molecules. For this reason exploring elongated GNPs such as GNRs is a way to improve sensitivity factor.<sup>76</sup>

#### *1.4.2 Fluorescence quenching biosensing*

GNPs can serve as excellent fluorescence quenchers due to their high molar extinction coefficients and broad energy bandwidth.<sup>77</sup> Tang and co-workers have designed a fluorescence quenching-based cholesterol sensor by using  $\beta$ -cyclodextrin functionalized GNPs.<sup>78</sup> Ni and co-workers have shown that single strand oligonucleotide functionalized GNPs with fluorophore terminal can assemble into a constrained arch-like conformation.<sup>79</sup> In this conformation the fluorophore is efficiently quenched by GNPs due to close donor and acceptor distance. Upon binding with the target DNA, the constrained conformation opens and the fluorophore is separated from the GNPs, resulting in fluorescence turn on.

#### *1.4.3 Electrochemical biosensing utilizing GNPs.*

GNPs feature an excellent conductivity, a high surface area and catalytic properties that make them a great material for the electrochemical detection of a wide range of analytes.<sup>80, 81</sup> GNPs have been used for enhanced electrochemical detection of numerous small molecules including glucose, dopamine, uric acid, etc. For example, Wang and co-workers have electrocatalytically detected epinephrine using a self assembled dithiothreitol–dodecanethiol-gold colloid modified gold electrode. The electrode reaction of epinephrine is significantly improved at the nanogold electrode, providing a detection limit of 60 nM.<sup>82</sup> DNA sensing has likewise been performed using GNPs-DNA conjugates on graphite carbon electrode using methylene blue as an electroactive label by applying

differential pulse voltammetry<sup>83</sup>. The resulting system enhanced the response signal during immobilization and hybridization by increasing the density of redox active sites.<sup>84</sup> Numerous examples of determining IgG<sup>85</sup> as well as IgE<sup>86</sup> via GNPs-based electrochemical immunosensors can be found in the literature, providing an IgG detection limit of picomolar, competitive with ELISA.

#### *1.4.4 SERS biosensing.*

Surface-enhanced Raman scattering is a vibrational spectroscopic technique used to detect molecules on or near the surface of plasmonic nanoparticles with high sensitivity, which greatly increased the role of standard Raman spectroscopy.<sup>87</sup> Since its discovery in the 1970s,<sup>88-90</sup> SERS has been applied to many analyses, especially in biochemistry and life science.<sup>91-93</sup> The physical phenomenon behind Raman spectroscopy is the inelastic scattering of photons by a molecule having quantized vibrational signature.<sup>83</sup> Raman scattering is sensitive to different vibrational modes and consequently can provide a “fingerprint” of the target molecules.<sup>94</sup> However, the direct application of this technique in sensitive detection and identification of analyte molecules is severely restricted owing to the low efficiency of inelastic photon scattering by molecules such as biological molecules leading to a weak signal.<sup>95</sup> The inherent limitation of low scattering intensity arises from the fact that the Raman scattering cross sections for molecules are usually small typically  $10^{-30}$ - $10^{-25}$  cm<sup>2</sup> molecules, 10-15 orders of magnitude smaller than that of a fluorescence cross section. In the presence of plasmonic nanoparticles, however the Raman

scattering intensity from a molecule can be enhanced by up to  $10^{14}$ .<sup>88, 89, 96</sup> This phenomenon has been attributed to two primary theoretical models, electromagnetic (EM) enhancement and chemical enhancement (CE).

It is commonly thought that EM enhancements are the major contributor to the SERS phenomenon. When incident light illuminates noble metal NPs, it causes collective oscillations of the nanoparticle surface electrons (LSPR). When the frequency of incident light is resonant with a plasmon, then the metal NP will generate a dipolar field. A molecule near or adsorbed at the nanoparticle surface will experience much-enhanced incident intensity that excites its Raman modes. This enhancement has a strong molecule distance dependence feature: Only molecules on or very close to the metal surface experience the enormous field enhancement.<sup>97-99</sup> The EM enhancement mechanism does not totally explain all the aspects of the SERS phenomenon. Researchers have only proposed a CE mechanism, which is responsible for an order or two of magnitude of enhancement to the Raman signal intensity. CE refers to the interaction between adsorbed molecules and a metal surface. This is explained by the molecule surface interaction inducing a novel charge transfer intermediate that has a higher Raman scattering cross section than do those of the free Raman molecules that are not adsorbed onto the NP surface.<sup>100, 101</sup>

In two separate studies, the observation of a single molecule SERS for dye molecules in silver colloid was reported. In the single molecule detection cases, the combined Raman signal enhancement was nearly 14 orders of

magnitude greater than those obtained in the absence of a metal nanoparticles.<sup>101</sup>,  
<sup>102</sup> This high sensitivity laid the foundation for SERS labels of GNPs. The development of these SERS labels is a significant step forward in biosensor applications. These SERS labels exploit intrinsically strong Raman scattering of aromatic compounds called Raman reporters, preparation of these SERS labels will be discussed in details later in this chapter. These SERS labels offer some main advantages over other optical probes, such as organic fluorescence dyes and quantum dots (QDs).<sup>103</sup> For example, each label is coated with a large number of reporters ( $10^3$ - $10^5$ ).<sup>104</sup> Consequently, the response to an individual binding event is therefore markedly amplified. Raman vibrational bands exhibits narrow line width (<1 nm) compared to fluorescent bands (50 nm) thus, Raman based probes are inherently suitable for multiplex analysis. The extremely short lifetimes of Raman scattering prevent photobleaching, energy transfer, or quenching of Raman reporters in the excited state<sup>105</sup>, rendering high photostability to SERS labels. Optimal contrast can be achieved using visible to near infrared (NIR) excitation to minimize the disturbing fluorescence of cells and tissues, enabling SERS labels to be used for noninvasive imaging in living objects.<sup>106</sup>

Mirkin and co-workers developed the quantitative SERS-based multiplexed detection of DNA and RNA targets by employing GNP probes functionalized with oligonucleotides and Raman active dyes.<sup>107</sup> For this quantitative assay, dye-labeled GNP probes were captured by the target oligonucleotide strands, followed by silver enhancement, generating detectable

SERS signals exclusively from the Raman dyes immobilized on the particles, with a limit of detection of 20 fM. GNPs functionalized with either protein ligands or antibodies and Raman dyes to perform multiplexed screening of protein-small molecule interactions and protein-protein interactions in a microarray format was also reported.<sup>108</sup>

Biosensing applications of SERS labels of NPs were extended to in vivo biosensing. One key for the use of SERS labels in living cells is sensitive detection of cancer biomarkers on the cell membrane, demonstrating the potential for high-throughput screening of cancer cells. Sha and co-workers reported detecting circulating breast cancer cells in the blood by using a combination of epithelial cell-specific, antibody-conjugated, magnetic probes anti HER2 antibody-conjugated SERS labels. Because the HER2 receptor is highly expressed on the breast cancer cell membrane, SERS labels will specifically recognize these tumor cells. Thus, the cancer cells could be detected rapidly, with good sensitivity and calculated limit of detection of less than 10 cells/mL.<sup>109</sup> SERS-based rapid screening of pathogenic bacteria has also been achieved utilizing GNPs.<sup>68, 110</sup> Light scattering, absorption, and fluorescence arising from biological samples limit the choice of Raman excitation wavelength to the near-infrared (NIR) spectral region.<sup>111, 112</sup> In this spectral region (700-1100 nm), GNPs can be used as effective SERS-active nanoparticles as they exhibit a tunable longitudinal LSPR band.<sup>113</sup>

Several aspects of SERS-based immunoassay utilizing SERS labels of GNPs have to be carefully controlled to achieve quantitative and reproducible results.<sup>104</sup> The SERS response of GNPs is size and shape dependent, which affects the overall intensity of the SERS signal.<sup>104</sup> For this, uniform size and shape of GNPs after any modification step should be assured. The colloidal stability of functionalized GNPs is the other factor that needs to be strictly controlled. The nanoparticle surface needs to be designed in such way that prevents aggregation by maintaining a highly negative or positive surface charge.<sup>104</sup> This is because aggregation of GNPs remarkably enhances SERS signals in a manner that may result in irreproducible results.<sup>114</sup> Further, the antibody needs to be covalently linked to the surface to prevent desorption during the assay, which could lead to a reduction in the signal.<sup>115</sup> Stable covalent bonds can be formed by coating the GNPs utilizing thiolate ligands with a terminal functional group such as carboxylic acid and with the aid of coupling reagents such as N-(3-dimethylaminopropyl)-N'-ethylcarbodiimide hydrochloride (EDC) and N-hydroxysuccinimide (NHS), carboxylic acid groups are activated for the reaction with the amino groups from biomolecules such as antibodies forming an amide linkage.<sup>116,117</sup>

## **1.5 Surface modification of metal nanoparticles**

The surface plays an important role in the properties of metal nanoparticles, including the solubility, colloidal stability, and electronic

structure.<sup>118</sup> At the same time, the surface plays a vital role in the conjugation with target molecules for biosensing application. During growth of the metal NPs, stabilizing agents are present to prevent nanoparticles aggregation and precipitation. Various organic and inorganic materials have been utilized as capping materials on the NP surface through covalent or ionic interactions.<sup>119, 120</sup> These capping molecules can preserve the colloidal stability of the nanoparticles in solution. Tuning the surface capping materials of the nanoparticles allow one to tailor the optical and electronic properties and so the application of these nanoparticles.

Nanoparticle-based SERS labels are created by attaching Raman reporters to the surface of metal NP that results in a known SERS spectrum of the Raman reporter. Attaching Raman reporters onto metal NP surface can produce probes with SERS signal that are ready for biological labeling. A simple metal nanoparticle-Raman conjugates usually lack colloidal stability. Hence, carefully designed coating materials are essential to maintain colloidal stability, reduce non-specific binding of interfering molecules in the biological sample and provide terminal functional group available for further conjugation with biological molecule.<sup>104, 121</sup> Once this basic structure is established, a bio-recognition element such as an antibody may be added to render the label with stability and a selective binding feature. This conjugate of biological molecules with NP modified with Raman reporter is called extrinsic Raman label (ERLs).

A variety of surface coating materials and encapsulation methods have been proposed for surface modification of GNPs. In general, there are two strategies applied for this purpose: (1) ligand exchange and (2) surface covering. Ligand exchange can be used to replace the original coating of the GNP with a different ligand. Since there is a strong affinity between sulfur and gold, molecules containing thiol or disulfide functional groups are often used. These are allowed to self-assemble at the GNP surface as a result of the specific interaction of the sulfur end-group with the gold surface.<sup>122, 123</sup>

Spontaneous self-assembly of n-alkyl thiolate ligands on gold surface form a well-ordered monolayer is illustrated in Figure 1.05. The benefits of employing thiolates to modify gold surfaces include ease of use, reproducible film formation, and wide compatibility due to the flexibility of the terminal group. The adsorption process consists of several steps that include diffusion to the surface and re-arrangement into a crystalline film.<sup>124</sup> It is generally understood that thiols and disulfides adsorb to gold as thiolates.<sup>124</sup> Typically, the crystallinity of the adlayer is dependent on the type of thiol used. Long alkanethiols ( $C \geq 8$ ) produce more densely packed, organized structures through van der Waals interactions between the alkyl chains which aids in monolayer packing.<sup>125</sup> Further, it was determined that the molecule orientation at the gold surface is typically tilted with respect to the surface normal in order to maximize intermolecular forces.<sup>126, 127</sup> The thiol-terminated polyethyleneglycol (PEG) is

another popular ligand that is commonly used for GNP surface modification.<sup>128,</sup>

129

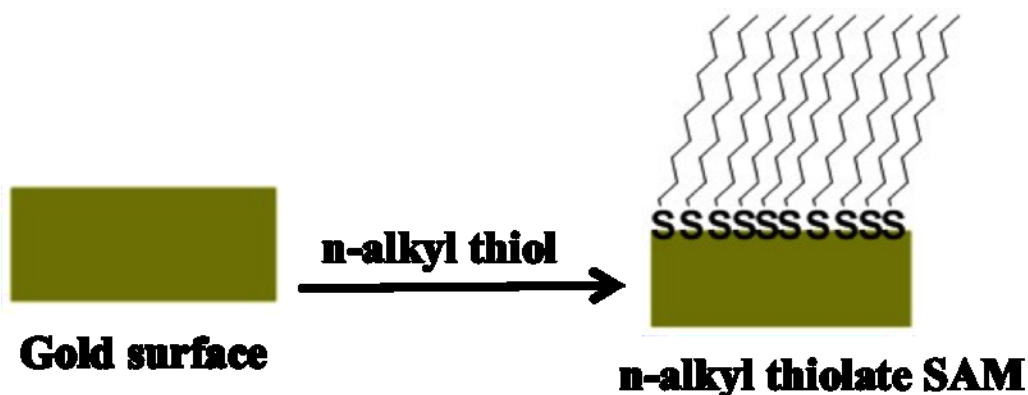


**Figure 1.05.** Schematic illustration of spontaneous self-assembly of thiol ligands on gold surface forming a well-ordered thiolate monolayer.

There are many advantages of using thiolated PEG may include for example, PEG is nontoxic, a water-soluble polymer so that the modification of GNPs can be conducted in an aqueous solution, a weak affinity to interference molecules, and an excellent biocompatibility.<sup>106, 130, 131</sup> Other polymers have been also explored such as polyvinylpyrrolidone polymer<sup>132</sup> and chitosan.<sup>133, 134</sup>

GNP surface coating is another approach in NP surface modification, which aims to introduce an additional coating to cover the entire surface of NP. Liposome coating for NPs was reported because of their ability to self-assemble into organized structures. Furthermore, the stability and targeting properties of liposomes can be provided by the lipid vesicle itself and by the targeting molecules bound to lipid anchors.<sup>135, 136</sup> Silica coating is another attractive

coating method that provides colloidal stability, water solubility, low nonspecific binding, and ease of further modification in biological systems.<sup>105, 137</sup> In 2003, two groups simultaneously reported creating silica-coated, dye-linked, GNPs for use as SERS labels by hydrolysis of sodium silicate.<sup>105, 137</sup> However, it requires time-consuming pretreatment steps such as dialysis, ion exchange, and a preparation time exceeding 30 hours.<sup>138</sup> Caruso and co-workers have demonstrated an easy way of surface covering is to coat the charged surface of GNPs with oppositely charged polyelectrolytes through the use of electrostatic absorption, this method is called layer-by-layer (LBL). In this method, electrostatic attraction between alternately deposited charged species of proteins and polyelectrolytes is used to form multilayers on the gold colloid surface.<sup>139</sup> However, coating of NPs prepared by this electrostatic force method normally suffers from poor stability and poor uniformity.

### *1.5.1 Preparation of ERLs.*

In 1999, Porter and co-worker pioneered SERS-based immunoassays that utilized bio-conjugated spherical gold NPs. The method exploited the SERS derived signal from Raman reporter molecules that are co-adsorbed with capture antibodies on the GNP surface to serve as ERLs.<sup>140</sup> Porter and his research group developed three types of ERLs. Figure 1.06 illustrates the three proposed schemes for ERLs fabrication. The first scheme is for the first introduced type of ERLs used co-adsorbed antibodies and Raman reporter molecules in a mixed

monolayer. The second scheme is for ERLs modified with a bifunctional molecule that has a large scattering cross section and a reactive moiety (e.g. succinimidyl group) to covalently couple a capture antibody. A number of bifunctional molecules were tested such as 5,5'-dithiobis (succinimidyl-2-nitrobenzoate). This molecule has an aromatic nitro group, which has a large scattering cross-section and disulfide moiety that reacts with gold by cleaving and forming a thiolate layer. The third scheme depicts designed ERLs with a mixed thiolate layer of antibody linkers and Raman reporter molecules. An example of an antibody linker is dithiobis (succinimidyl propionate) that has a small scattering cross section. Thus, the second thiolate is selected to have a large Raman cross-section (e.g. 4-nitrobenzenethiol).<sup>115</sup>

## **1.6 Motivations and goals**

As introduced in this chapter, there are a tremendous number of biosensing applications utilizing spherical GNPs. In parallel, there are a considerable number of studies proved that when spherical nanoparticles are transformed into one of arbitrary shape of NPs such as GNRs, the LSPR of these rods are significantly affected, typically red-shifting and generating stronger electric field at the rod surface especially at the corners. Because of the challenge of GNR surface modification, a limited number of research groups exploited the biosensing application of GNRs. This is the drive towards modifying the GNR surface, and preparing SERS labels of GNRs (Chapter 2) to be tested in SERS-

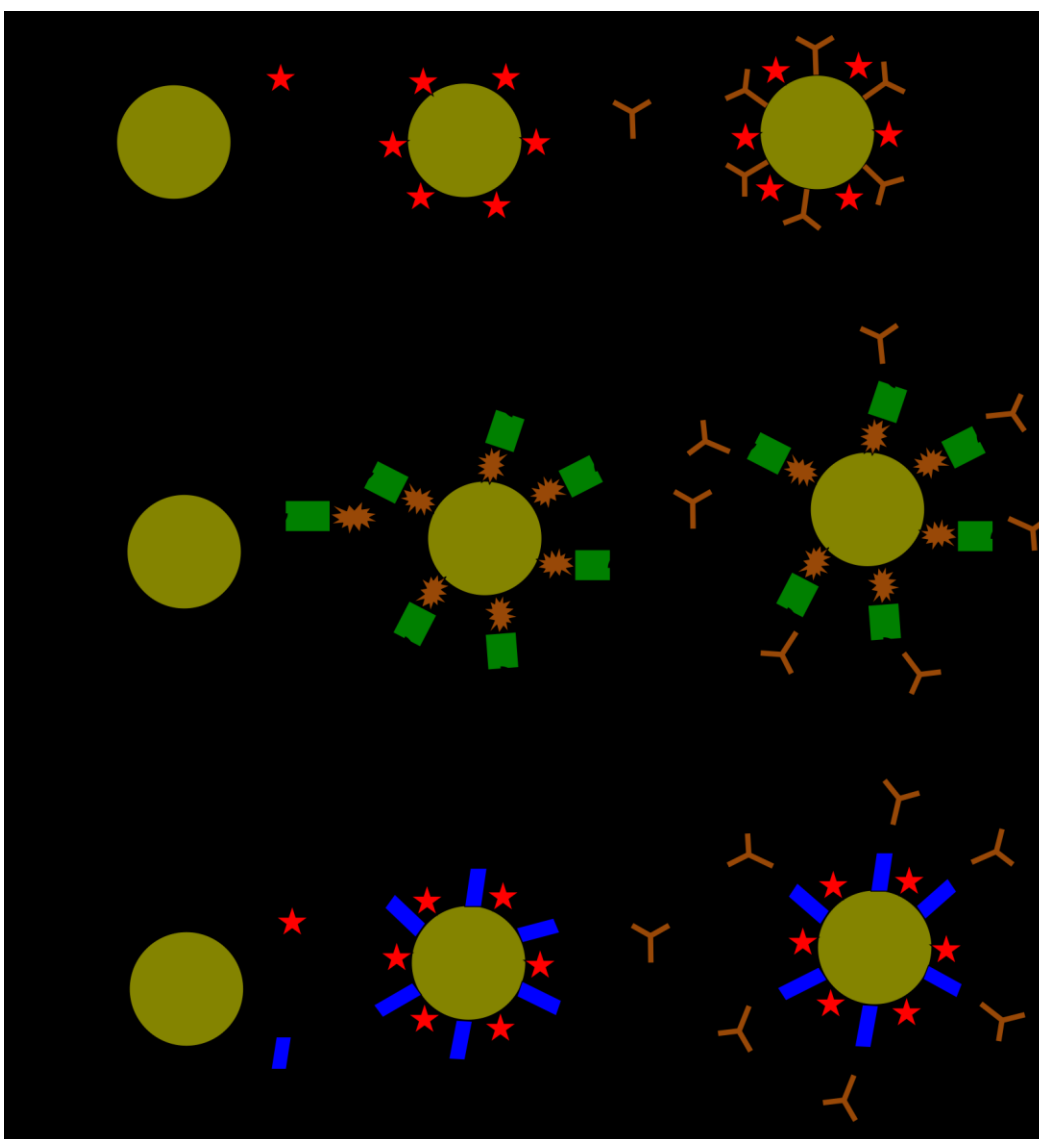


**Figure 1.06.** Schematic illustration of three types of ERLs; ERLs based on co-adsorption of antibodies and Raman reporter molecules (Scheme I), ERLs with a monolayer of bifunctional coating (Scheme II), and ERLs with a mixed monolayer of Raman reporter and antibody linker (Scheme III).

based assays (Chapter 4 and 5).

In Chapter 2, the goal is to replace cetyltrimethylammonium bromide (CTAB) coating of GNRs with a mixed thiolate monolayer of a Raman reporter such as 4-nitrobenzenethiol (tNB) and a thiol linker that provides terminal functional group for further conjugation with a biomolecule as well as preserves the colloidal stability of the GNRs in solution. Chapter 3 serves as an extension to the previous chapter and is meant to provide an experimental investigation of SERS intensity of 30 nm diameter spheres of GNPs and GNRs of four-different aspect ratios. These GNPs will be prepared as SERS labels and be examined in solution to show the benefits of employing nanorods over spherical NPs.

Building upon the knowledge acquired from Chapter 2 and 3, the motivation behind Chapter 4 and 5 was to take advantage of the richness of Raman signatures and terminal functionality of modified GNRs, and applying this to prepare bioconjugate of these rods to be used as extrinsic Raman labels (ERLs) in SERS based-assays. A SERS-based sandwich immunoassay with ERLs of GNRs was developed for quantitative analysis of goat IgG as a model system for IgG detection (Chapter 4). Indirect competitive SERS based-assay utilizing thyroxine-conjugated GNRs is developed for quantitative analysis of free thyroxine ( $fT_4$ ) as a model system for detection of a small metabolite molecule (Chapter 5). ELISA will be used to benchmark our SERS-based assay for  $fT_4$ . The constructed SERS calibration curve for these six standard solutions of  $fT_4$  will be compared to the ELISA calibration curve for the same standards to

compare the analytical performance of a SERS-based competitive assay utilizing fT<sub>4</sub>-conjugated GNRs to an already established detection technique.

## 2 Chapter II

---

### Formation of SERS active mixed monolayer of gold nanorods

#### 2.1 Introduction

This chapter explores the surface modification of cetyltrimethylammonium bromide (CTAB) capped gold nanorods (GNRs) to serve as water-soluble surface enhanced Raman scattering (SERS) labels for biosensing applications. Other laboratories have reported the use of either gold or silver nanorods as SERS substrates. Nikoobakht and coworkers reported surface enhancement factors of  $\sim 10^5$  for 2-aminothiophenol on individual and aggregated GNRs.<sup>114, 141</sup> Murphy and coworkers use GNRs and other nanoparticles morphologies immobilized on self-assembled monolayers on planar substrates to sandwich Raman reporter molecules via electrostatic interaction. While enhancement factor of  $10^8$  were estimated for 4-mercaptobenzoic acid monolayer using nanorods in this geometry, the nanorods aspect ratio dependence on SERS response was not observed due to plasmon coupling between the nanoparticles and the gold surface.<sup>142</sup> Recent studies on SERS with the GNRs based on Raman reporter molecules, which were separated at a fixed distance from the surface of the GNRs and this was accomplished by employing an ultra-thin silica shell.<sup>138</sup> Murphy incorporated a Raman dye such as methylene blue (MB). The MB molecules were then trap-coated by an additional polyallylamine hydrochloride following a layer-by-layer (LBL) method.<sup>143</sup> All of these studies proved that the

GNRs are promising SERS candidates. However, the chemistry for replacement of CTAB and surface functionalization with high cross section Raman molecules for maximum SERS enhancement are still challenges.

Commercially available GNRs are typically synthesized in the presence of CTAB surfactant. CTAB forms a tightly packed bilayer on the side faces of GNRs and leaves the ends of the rods more exposed for anisotropic growth along the longitudinal axis.<sup>144, 145</sup> The CTAB plays two important roles. Firstly, CTAB is widely employed to control and direct the growth of the GNRs into the desired sizes and shapes that are correlated to the desired wavelength of light that these nanorods can absorb and scatter.<sup>145, 146</sup> Secondly, the CTAB bilayer provides a positively charged surface that repels the individual nanorods from each other and prevents aggregation in solution.<sup>147</sup> Despite the high stability of the CTAB capped GNRs in aqueous solution. The CTAB lacks functionalization sites, which hampers the GNRs application in chemical and biological sensing.<sup>148</sup> A number of groups have studied CTAB displacement and exchange with other gold binding ligands such as alkane thiols. However, direct exchange of the CTAB with alkane thiols has, so far, not been achieved without significant irreversible aggregation of the GNRs.<sup>149, 150</sup> Complex protocols have been developed including a strict procedure with precise temperature control and modification within an ionic exchange resin to move towards complete coverage of the GNR surface with alkane thiols.<sup>151, 152</sup> In recent work, biocompatible polymers have been explored as simple models to maintain colloidal stability and

provide specific functionality to the GNRs. For instance, thiolated polyethyleneglycol (PEG),<sup>153</sup> carbohydrate-based polymer (Chitosan),<sup>154</sup> lipid bilayer,<sup>155</sup> and phospholipids<sup>156</sup> have been demonstrated to replace the CTAB bilayer. It is unknown how much CTAB is left on the GNR surface after modification. Murphy and coworkers initially reported an alternative method that is commonly used for functionalization of the GNRs. They utilized LBL deposition of polyelectrolytes directly on to the CTAB bilayer surrounding the GNRs.<sup>143, 157</sup>

Herein, we are studying functionalization of GNRs to be used as SERS labels for future biosensing applications. We looked for a rational design based on exchange of the CTAB cap with ligands to serve as a Raman reporter, maintain the colloidal stability of the GNRs and provide anchor points to be ready for linking to biological molecules. Figure 2.01 presents the proposed two-step scheme for functionalization of the GNR surface. The first step included displacement of the CTAB bilayer with 2-(2-{2-[2-(2-[2-(11-mercapto-undecyloxy)-ethoxy] ethoxy)-ethoxy]-ethoxy}-ethoxy)-ethoxy)-acetic acid (HSC<sub>11</sub>(EO)<sub>6</sub>~COOH). Based on previous work, the -SC<sub>11</sub>(EO)<sub>6</sub>~COO<sup>-</sup> molecules initially adsorb on the ligand-free (111) ends of the GNRs.<sup>158</sup> Then the -SC<sub>11</sub>(EO)<sub>6</sub>~COO<sup>-</sup> exchanges with the CTAB molecules on the (110) or (100) crystal faces<sup>25, 158</sup> due to the higher affinity of thiolate than bromide ions towards gold. The second step includes incubation of the -SC<sub>11</sub>(EO)<sub>6</sub>~COO<sup>-</sup> modified GNRs in 4-nitrobenzenethiol (tNB) solution.

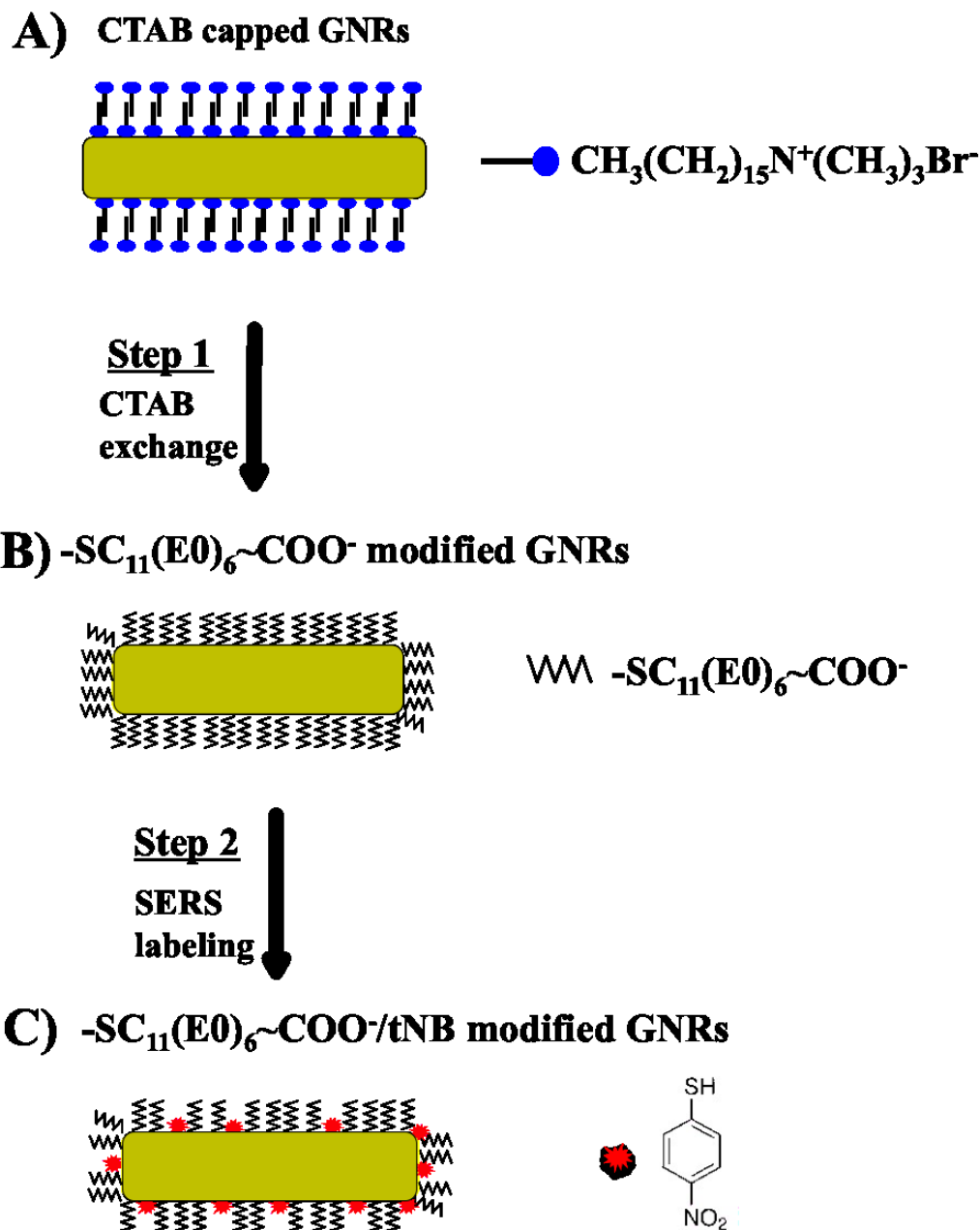


**Figure 2.01.** Schematic representation of the two-step procedure proposed to produce SERS labels of GNRs. A) CTAB capped GNRs, B)  $-\text{SC}_{11}(\text{EO})_6\text{-COO}^-$  modified GNRs and C)  $-\text{SC}_{11}(\text{EO})_6\text{-COO}^-/\text{tNB}$  modified GNRs.

In this work, we characterized the GNRs before and after each modification step in Figure 2.01. X-ray photoelectron spectroscopy, Zeta potential and high resolution transmission electron microscopy (HRTEM) measurements were utilized to track replacement of the CTAB capping material with  $\text{-SC}_{11}(\text{EO})_6\text{-COO}^-$  and tNB. Also, HRTEM images for GNR crystal face were used to study sites of ligands exchange. UV-visible extinction spectra coupled with scanning electron microscopy (SEM) images were used to study colloidal stability of GNRs. SERS spectra were collected for the GNRs before and after each modification step to show the replacement of the gold bromide Raman signal of CTAB capped GNRs with the Raman fingerprint. To the best of our knowledge, these are the first CTAB-free GNRs reported as SERS labels with these characteristic activated surface features.

## 2.2 Experimental

### 2.2.1 Reagents and Materials

Cetyltrimethylammonium bromide (CTAB) capped GNRs were purchased from NanoPartz, Loveland Colorado, U.S.A. Purchased solutions contained  $8.31 \times 10^{10}$  GNRs per mL with  $60 \pm 5$  nm length,  $25 \pm 5$  nm width and an aspect ratio of 2.4. 2-(2-{2-[2-(2-[2-(11-mercapto-undecyloxy)-ethoxy] ethoxy)-ethoxy]-ethoxy}-ethoxy)-ethoxy)-acetic acid ( $\text{HSC}_{11}(\text{EO})_6\text{-COOH}$ , MW= 526.73 g/mol) was from ProChimia, Poland. A solution of 40 mM

HSC<sub>11</sub>(EO)<sub>6</sub>~COOH was prepared in deionized water. 4-nitrobenzenethiol (98%) was from Aldrich. 4 mM 4-nitrobenzenethiol (tNB) solution was freshly prepared in 20% anhydrous ethanol (Quantum Chemical, Victoria, Australia) and 80% deionized water with a Millipore Milli-Q Plus purification system. The reason for preparation of tNB in a mixture of 4: 1, water: ethanol was to avoid GNR aggregation. El-Sayed and coworkers demonstrated induction of GNRs aggregation when absolute alcohol was used as solvent.<sup>114</sup> Although, a considerable amount of black precipitate of aggregated GNRs was observed when 10 mM of HSC<sub>11</sub>(EO)<sub>6</sub>~COOH was tried first to replace the CTAB cap of GNRs, these aggregates were not observed at higher concentrations of 40 mM HSC<sub>11</sub>(EO)<sub>6</sub>~COOH. UV-visible extinction spectroscopy and SEM imaging confirmed these observations.

### 2.2.2 Preparation of GNRs as SERS labels

Replacement of the CTAB cap with -SC<sub>11</sub>(EO)<sub>6</sub>~COO/tNB. The commercial GNR solution contained excess free CTAB, CTAB-capped GNR solutions were purified from excess CTAB by centrifugation once at 8000 rpm for 10 min and 25 °C in an Eppendorf a5417R microcentrifuge. The pellets of GNRs were dispersed in 1 mL of 40 mM HSC<sub>11</sub>(EO)<sub>6</sub>~COOH, sonicated for 1 min and allowed to stand with intermittent gentle shaking for 24 h for the exchange reaction to take place at room temperature. After 24 h, GNRs were sonicated for 1 min and centrifuged once at 8000 rpm for 10 min then the

supernatant of excess  $\text{HSC}_{11}(\text{EO})_6\text{-COOH}$  was removed without disturbing the pellets. The pellets were either resuspended in 1 mL of deionized water for characterization or in 4 mM tNB for further modification as discussed below.

Incorporation of Raman reporter (tNB) molecules onto the GNR surface.

The  $\text{-SC}_{11}(\text{EO})_6\text{-COO}^-$  modified pellets were resuspended in 1 mL of 4 mM tNB in a mixture of 4: 1, water: ethanol. The GNR suspension was sonicated for 1 min and allowed to stand for 24 h at room temperature with intermittent gentle shaking. The excess of tNB and any  $\text{HSC}_{11}(\text{EO})_6\text{-COOH}$  in the solution were removed by centrifugation once at 8000 rpm for 10 min and the pellets were resuspended to 1mL in deionized water for surface characterization to confirm modification. The modified GNRs were stable and stored at 7 °C until use.

### 2.2.3 Instrumentation

UV-vis extinction spectroscopy. UV-visible extinction spectra for GNRs in aqueous solutions were measured on a Perkin-Elmer Lambda 35 UV/VIS/NIR spectrometer with a 10 mm optical path length and 1 nm bandwidth. Deionized water was used as the blank.

Scanning electron microscopy (SEM). SEM images were performed firstly to explore the degree of GNR dispersion after modification. SEM sample was prepared by drop casting 20  $\mu\text{L}$  of the modified GNRs on a clean gold-coated substrate (200 nm thick films) and left to air-dry. Secondly, SEM images were collected to count the density of GNRs dried on (1 in.  $\times$  1 in.) fused silica wafers and examined by XPS and SERS. SEM images were collected using a

Hitachi S4800 FE-SEM system (Hitachi Scientific Equipment). Image acquisition on the Hitachi SEM was carried out with a 20.00 kV accelerating voltage and a 15  $\mu$ A emission current. The working distance was approximately 10-15 mm.

High resolution transmission electron microscopy (HRTEM). HRTEM imaging was used to examine the atomic structure of the GNR crystal surfaces and to characterize the film thickness. Nanopartz GNRs were centrifuged three times at 8000 rpm for 10 min to remove excess CTAB molecules in solution and the pellets were resuspended in deionized water. The CTAB bilayer was removed from the GNR surface on the TEM grid using ozone treatment (UVO-Cleaner, Model No. 42, Jelight Company Inc.) for 20 min. High-resolution TEM images were captured using a JEOL ARM200F TEM/STEM microscope with a 200 kV cold field emission gun. Spherical aberration corrector for electron optic system has achieved a scanning transmission image (STEM-HAADF) resolution of 0.08 nm instruments. Secondly, HRTEM images were taken to measure the coating thickness after modification. TEM grids (carbon coated copper grid) were prepared by drop casting 2  $\mu$ L of CTAB capped GNR and  $-\text{SC}_{11}(\text{EO})_6\sim\text{COO}^-$  modified GNR solutions on the TEM grids. The solutions were wicked through the grid by touching the underside to filter paper, and then left to air-dry before analysis. This method was used to avoid forming specific patterns of GNRs on the grid surface due to water evaporation.<sup>159</sup> These HRTEM images were

obtained with a JEOL 2200FS TEM/STEM microscope with a 200 kV field emission gun and in-column energy filter (Omega Filter).

X-ray Photoelectron Spectroscopy (XPS). XPS samples of CTAB capped,  $-\text{SC}_{11}(\text{EO})_6\text{-COO}^-$  and  $-\text{SC}_{11}(\text{EO})_6\text{-COO}^-/\text{tNB}$  coated GNR solutions were prepared by placing 20  $\mu\text{l}$  of each GNR solution  $\times 4$  onto 1 in.  $\times$  1 in. fused silica wafers and left to air-dry. The XPS analysis was performed at the Alberta Centre for Surface Engineering and Science (ACSES) using an Axis-Ultra Spectrometer (Kratos Analytical). The monochromatic Al  $K\alpha$  source ( $h\nu = 1486.6$  eV), was operated at a power of 210 W, and the analytical chamber were maintained a base pressure lower than  $\sim 4 \times 10^{-7}$  Pa. The spot size was 400  $\times$  700  $\mu\text{m}$ . High-resolution spectra were collected for N 1s, Br 3d, O 1s and S 2p with pass energy of 20 eV and a step size of 0.1 eV. All spectra were referenced to the C 1s peak at 284.8 eV. The XPS data was processed with CasaXPS version 2.3.15.

Zeta potential measurements. 1 mL solution of CTAB capped solution,  $-\text{SC}_{11}(\text{EO})_6\text{-COO}^-$  and  $-\text{SC}_{11}(\text{EO})_6\text{-COO}^-/\text{tNB}$  coated GNR solutions were measured with a Malvern Zetasizer Nano ZS with 633 nm laser at 25  $^{\circ}\text{C}$  for 10 seconds and 3 runs for each sample. The three samples were prepared in deionized water with pH 7.

Surface enhanced Raman scattering (SERS). Three GNR samples prepared similarly to the GNRs samples examined by XPS were drop cast on silica wafers and further characterized by SERS silica wafers were used in these experiments because they are relatively inert to interactions with CTAB. SERS

spectra were recorded with a Renishaw inVia Raman Microscope equipped with a high performance near IR diode (785 nm with a  $40 \times 2 \mu\text{m}$  spot size, 1200 l/mm) laser, and a CCD detector. Laser power at the sample was 14 mW, 50 $\times$ microscope objective, and the integration time was 10 s.

### 2.3 Result and Discussion

There has been significant interest in functionalizing the GNR surface through displacement of the CTAB cap to obtain GNRs with specific functionality for biosensing applications. Although different coating materials have been reported to modify GNRs, direct proof to support complete displacement of the CTAB capping molecules has been limited. In addition, SERS applications of GNRs are still confined to preferentially adsorbed Raman reporter molecules at the (111) free ends of GNR and/or the weak Raman signal of the CTAB bilayer.<sup>59, 114, 160</sup> Recently, methylene blue has been incorporated within the CTAB bilayer via electrostatic interactions and SERS spectra for methylene blue were obtained.<sup>161</sup> Our approach is to modify the surface of synthesized CTAB capped GNRs to prepare SERS labels in an aqueous solution with maintaining their colloidal stability and the ability to further functionalize via terminal carboxylic acid group.<sup>162, 163</sup> The modified surface of the GNRs was characterized with different spectroscopic techniques and electron microscope imaging.

### 2.3.1 Tracking the replacement of CTAB with $-SC_{11}(EO)_6\sim COO^-$ and 4-nitrobenzenethiol

X-ray photoelectron spectroscopy (XPS) characterization. XPS is a surface sensitive method for surface characterization, in which information on chemical bonding and elemental composition is provided.<sup>164, 165</sup> For this work we are mainly interested in the degree of CTAB replacement by  $-SC_{11}(EO)_6\sim COO^-$  and tNB. XPS were collected for three samples CTAB capped GNRs,  $-SC_{11}(EO)_6\sim COO^-$  modified GNRs and  $-SC_{11}(EO)_6\sim COO^-$ /tNB modified GNRs. Representative spectra are shown in Figure 2.02. Table 2.1 summaries the XPS data for three XPS samples, presents: the experimental calculated O/N ratio, the number of the GNRs counted manually from SEM images for three XPS samples, and the zeta potential measurements for three GNR solutions. It was previously reported that CTAB is bound to the surface through electrostatic interaction between cationic quaternary amine head and bromide ions that has a good affinity to gold.<sup>166</sup> Thus, the detected features for the XPS spectrum of CTAB capped GNRs are the presence of Br 3d and N 1s peaks. Figure 2.02A presents high-resolution Br 3d XPS spectra recorded for CTAB capped,  $-SC_{11}(EO)_6\sim COO^-$  and  $-SC_{11}(EO)_6\sim COO^-$ /tNB coated GNRs. XPS spectrum for CTAB capped GNRs exhibit a significant peak at 67.8 eV due to bromide ions from CTAB.<sup>167, 168</sup> Second peak at 68.3 eV was assigned by other research groups to AgBr because AgBr was used during GNRs synthesis and found in commercially available CTAB capped GNRs.<sup>169</sup> A sharp decrease of the Br 3d

signal was observed for  $-\text{SC}_{11}(\text{EO})_6\sim\text{COO}^-$  modified GNRs. Importantly, no Br 3d signal was detected at 67.8 eV for  $-\text{SC}_{11}(\text{EO})_6\sim\text{COO}^-/\text{tNB}$  GNR modified GNRs, which demonstrated displacement of the residual CTAB molecules on the GNR surface after modification.

Figure 2.02B presents high-resolution N 1s XPS spectra taken for three GNR samples and shows the characteristic signal located at 400.1 eV assigned for N 1s quaternary amine head of CTAB. The energy of the N 1s peak was consistent with that of a protonated amine group assigned by previous reports.<sup>170</sup> Close examination of the high resolution N 1s spectrum from the  $-\text{SC}_{11}(\text{EO})_6\sim\text{COO}^-$  modified GNRs produces a lower intense peak at 400.1 eV that assigned to a quaternary amine head of the CTAB molecules, and a second broad peak at 402.4 eV could be corresponding to N 1s peak for inner layer of CTAB capped GNRs.<sup>171</sup> This up-shift in the N 1s peak binding energy value corresponds to the decrease in charge transfer from the bromide ion to the positively charged  $\text{N}^+$  center of tetra-methylammonium head of inner CTAB layer due to the presence of Br-Au. However, this new N 1s peak at 402.4 eV could not be seen with the CTAB capped GNR sample. This observation can be reasoned by highly intense signal of CTAB well packed out layer that may shield N 1s signal from inner layer. Although, no signal from the N 1s signal CTAB was observed after incubation of  $-\text{SC}_{11}(\text{EO})_6\sim\text{COO}^-$  modified GNRs with tNB, a very small atomic concentration of N was detected. This could correspond to a the nitro group of tNB.

Another piece of supporting evidence is Figure 2.02C, which is the high-resolution XPS S 2p spectra, collected from three GNR samples. Typically, the S 2p peak is absent in the CTAB capped GNR sample. The  $-\text{SC}_{11}(\text{EO})_6\text{-COO}^-$  modified GNR XPS spectrum shows a single doublet with peaks at 162.2 and 163.4 eV due to the presence of bound  $-\text{SC}_{11}(\text{EO})_6\text{-COO}^-$  ligand. The S 2p spectrum acquired for this SAM had a doublet structure due to the presence of the S 2p<sub>3/2</sub> and S 2p<sub>1/2</sub> peaks. This doublet peaks could be fit using 2:1 peak area ratio and a 1.2 eV splitting. The binding energy of the S 2p<sub>3/2</sub> peak was 162.2 eV, consistent with sulfur atoms bound to the GNRs as a thiolate species. This agreed with the S 2p binding energy reported in the SAMs of alkane thiols.<sup>172, 173</sup> However, sulfur species with S 2p<sub>3/2</sub> binding energy above 165 eV were unbound thiols. These unbound thiols could be either lying on top of the SAM or partially penetrating into the SAM.<sup>174</sup> It was noticeable weak XPS signal of S 2p, which can be explained by the attenuation of sulfur signal due to inelastic scattering from the long hydrocarbon chains of SAM as has been reported by Whitesides and coworkers.<sup>175</sup>

Table 2.1 presents sharp drop in Br and N atomic concentrations was also recorded from 2.4 and 4%, respectively for CTAB capped GNRs to 0.01 and 0.06%, respectively for  $-\text{SC}_{11}(\text{EO})_6\text{-COO}^-/\text{tNB}$  modified GNRs. A slight

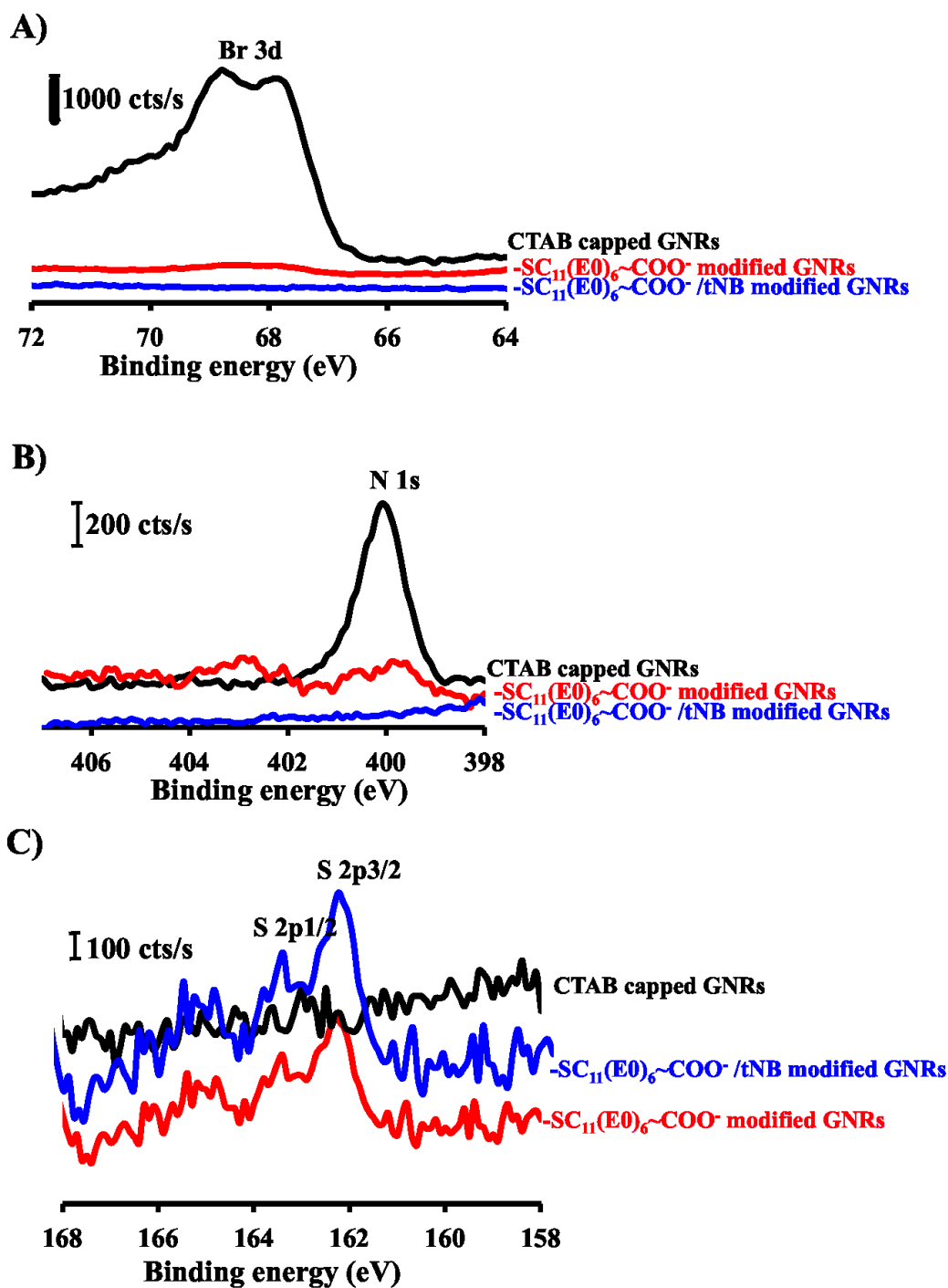


**Figure 2.02.** High-resolution XPS spectra for A) Br 3d, B) N 1s and C) S 2p peaks collected from the GNR samples before and after modification.

increase of sulfur atomic concentration was detected after tNB labeling from 1.47 to 1.67%, which can be attributed to incorporation of the tNB. The increasing ratio of O/N for GNR modified samples confirmed exchange of CTAB with thiolate ligands. The density of the GNR sampled was calculated by counting the average number of the GNRs measured by SEM micrographs to help in interpretation of the differences in the elemental composition related to how many GNRs has been examined. Zeta potential measurements for three GNR solutions were collected to track CTAB replacement with thiol ligands, which is discussed below.

Zeta potential characterization. The sign and the magnitude of the zeta potential are directly proportional to the sign and the magnitude of the surface charge density of a particle.<sup>143, 176</sup> In this work, we utilized zeta potential measurements coupled with XPS results to show successful CTAB coating exchange by the negatively charged  $-\text{SC}_{11}(\text{EO})_6\text{COO}^-$  ligand. The zeta potential measurements of the GNRs before and after modification are presented in Table 2.1. The zeta potential of the CTAB capped GNR solution after modification with  $-\text{SC}_{11}(\text{EG})_6\text{COO}^-$  changed from a highly positive (+36 mV) to a negative value (-16 mV), indicating the successive exchange of the positively charged CTAB by negatively charged  $-\text{SC}_{11}(\text{EO})_6\text{COO}^-$ . Although, the number of CTAB molecules left on the surface was not determined in this study, the lowering of zeta potential indicates that it is possible to displace most of the CTAB.

**Table 2.1.** XPS atomic concentrations of Br, N, S and O for the CTAB capped GNRs and after CTAB replacement with  $-\text{SC}_{11}(\text{EO})_6\sim\text{COO}^-$  and  $-\text{SC}_{11}(\text{EO})_6\sim\text{COO}^-/\text{tNB}$ .

System	Atomic concentration (%)				O/N	<sup>a</sup> GNR density/ $\mu\text{m}^2$	Zeta potential mV
	Br 3d	N 1s	S 2p	O 1s			
CTAB capped GNRs	2.4 ± 0.7	4 ± 1	0.01	5.2 ± 0.3	1.2 ± 0.2	$60 \pm 8$	$+37 \pm 2$
$-\text{SC}_{11}(\text{EO})_6\sim\text{COO}^-$ modified GNRs	0.42 ± 0.05	1.19 ± 0.07	1.5 ± 0.1	23 ± 3	21 ± 2	$55 \pm 6$	$-16 \pm 2$
$-\text{SC}_{11}(\text{EO})_6\sim\text{COO}^-$ /tNB modified GNRs	0.01	0.06	1.8 ± 0.2	25 ± 2	410 ± 2	$49 \pm 9$	$-33 \pm 2$

<sup>a</sup>The listed values are averages based on n=3 measurements for number of GNRs counted manually from SEM images. SEM images were collected for XPS samples before being examined by XPS analysis.

Incubation of the  $-\text{SC}_{11}(\text{EO})_6\sim\text{COO}^-$  modified GNRs in tNB solution provides particles with a more negative zeta potential,  $-33$  eV. This corresponds to near complete displacement of the CTAB as indicated by the XPS. Particles with a zeta potential of  $-33$  eV are expected to maintain colloidal stability in solution, which is observed as discussed below.

HRTEM film thickness measurements. CTAB capped gold nanorods and  $-\text{SC}_{11}(\text{EO})_6\sim\text{COO}^-$  modified GNRs were imaged with HRTEM to quantitatively measure the layer thickness. Previously, HRTEM has been used to image aliphatic thiols,<sup>177</sup> PEG coating<sup>58</sup> and polyelectrolyte films on GNRs.<sup>123, 143</sup> So far there has been no direct visualization of the CTAB coating by HRTEM. Our experiments agree with this. Figure 2.03A is a HRTEM image of a CTAB coated GNRs. No evidence of the coating is observed. Estimates for the thickness of CTAB bilayer on the GNR surface are generally not reported because of its non-covalent binding to the gold surface and dynamic equilibrium of CTAB bilayer with free CTAB molecules in solution.<sup>27, 148, 178, 179</sup> Gómez-Graña and coworkers recently used small angle X-ray (SAXS) and neutron (SANS) scattering to estimate the thickness of CTAB bilayer as 4-5 nm, which is less than a fully extended bilayer thickness of 5-6 nm. This is due to the partial intercalation between the two CTAB layers.<sup>180</sup>

Part B and C of Figure 2.03 are the HRTEM images of GNRs after reaction with  $\text{HSC}_{11}(\text{EO})_6\sim\text{COOH}$ . A faint layer with a thickness of  $2.2 \pm 0.6$  nm

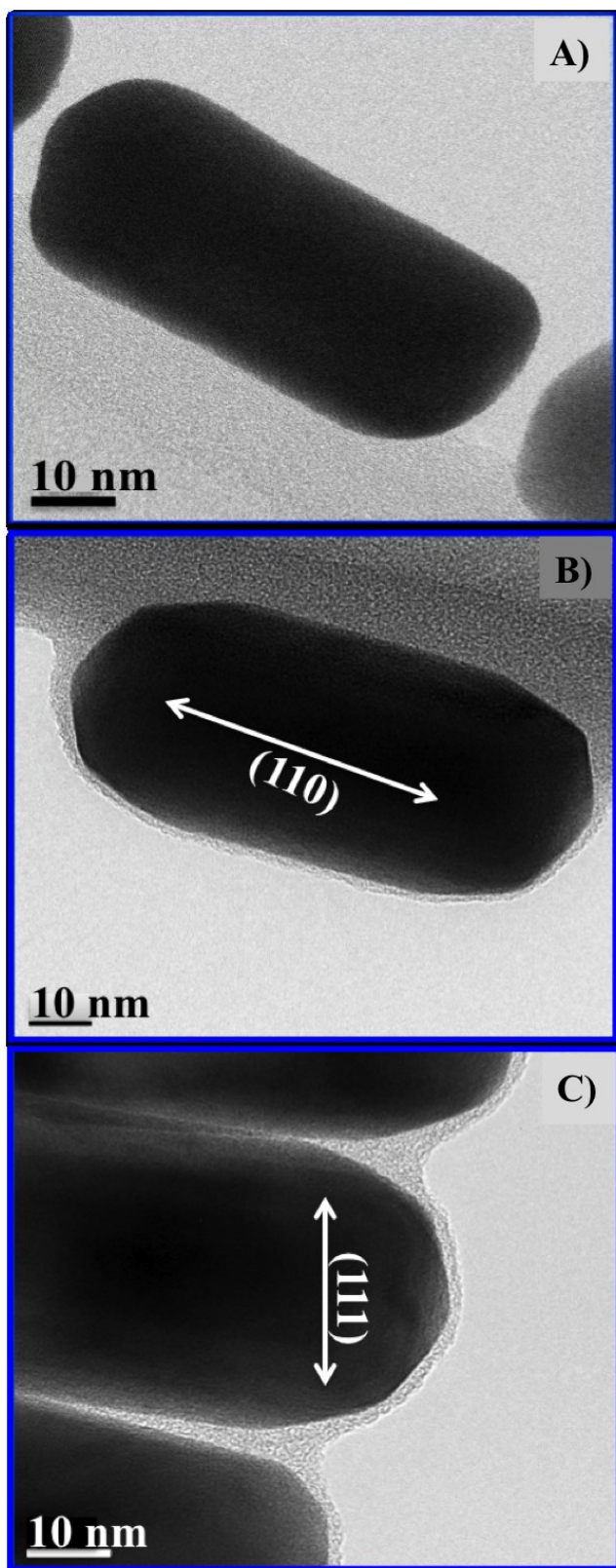


**Figure 2.03.** Bright field HRTEM images of (A) CTAB coated GNR, (B) and (C)  $-\text{SC}_{11}(\text{EO})_6\sim\text{COO}^-$  coated GNR. The thickness of the  $-\text{SC}_{11}(\text{EO})_6\sim\text{COO}^-$  layer was measured to be  $2.2 \pm 0.6$  nm.

is observed on the (110) and (111) crystal faces. The theoretical monolayer thickness for alkane thiol with C<sub>16</sub> to C<sub>25</sub> is in range of 2 – 3 nm,<sup>181, 182</sup> in comparable agreement with our HRTEM thickness of 2.2 ± 0.6 nm. Importantly, the thin film of -SC<sub>11</sub>(EO)<sub>6</sub>-COO<sup>-</sup> is observed on both the (111) and (110) crystal faces, consistent with the replacement of the CTAB.

### 2.3.2 Sites of exchange

HRTEM characterization of a single GNR crystal faces. Atomic scale defect structures of GNR surface were reported by Harmer and coworkers using HRTEM images and electron diffraction of a single GNR.<sup>183</sup> They observed that the (110) faces are uneven or ridged. This has important implications in modification of GNR surface and exchange of molecules on the (110) GNR faces in order to be used in sensing applications.<sup>183</sup> We investigated the atomic structure of the GNR surface using HRTEM. The HRTEM images in Figure 2.04 show that both (110) and (111) crystal surfaces are not atomically flat. These images reveal atomic scale step sites on both the (110) and (111) crystal faces of the GNRs. The existence of these step sites can lead to packing defects in the CTAB bilayer and therefore provide a site for replacement with -SC<sub>11</sub>(EO)<sub>6</sub>-COO<sup>-</sup>. These steps can also serve as insertion points for the tNB. In addition, long chain n-alkyl thiol SAMs (n ≥ 18) on gold nanoparticle surfaces are not perfectly crystalline, as revealed by the He diffraction in previous

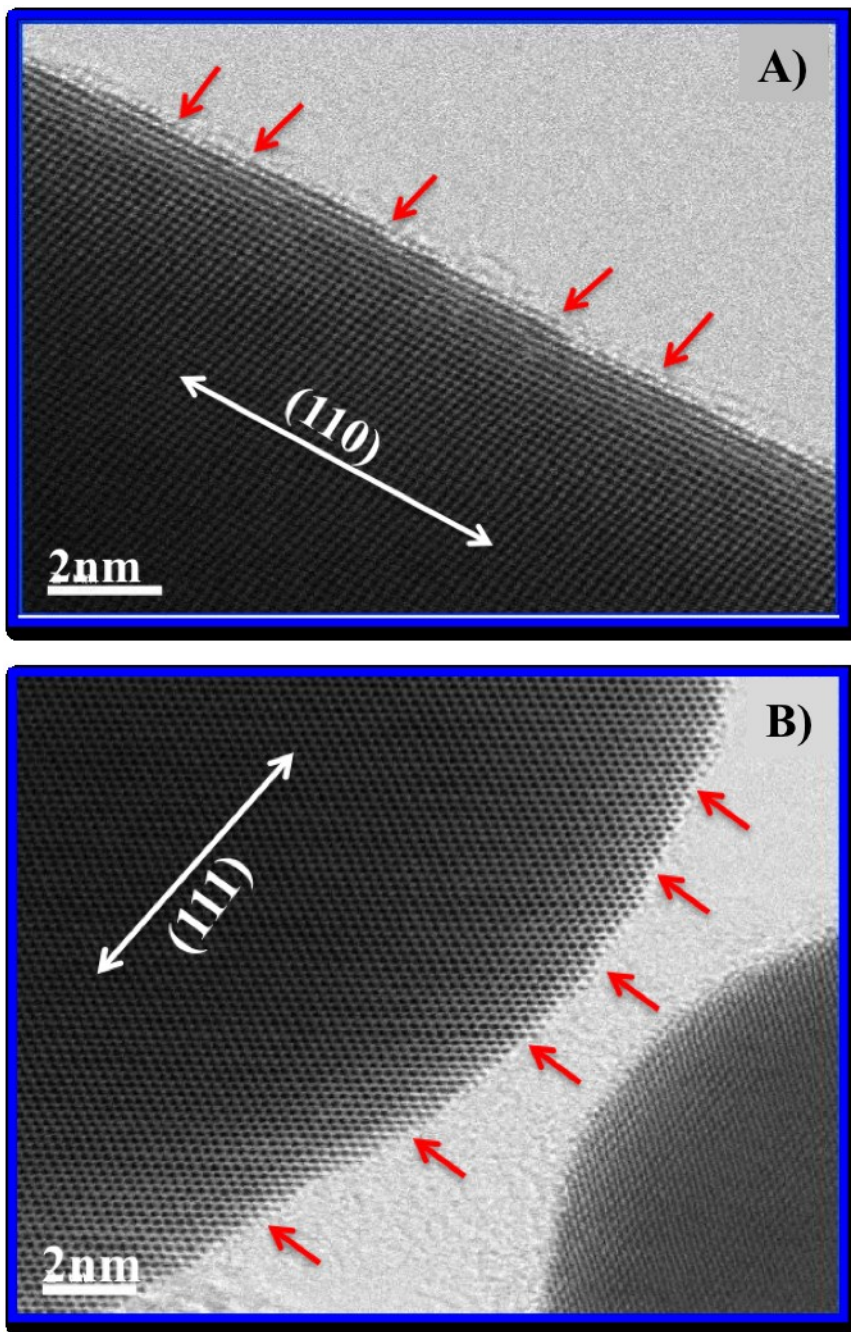


**Figure 2.04.** HRTEM images show atomic structure of a single GNR A) (110) face and B) (111) end. Non-atomically flat surface is visible due to structure defects. Red arrows points to atomic step sites on the GNR crystal faces.

studies.<sup>184, 185</sup> Similar disorder in the  $-\text{SC}_{11}(\text{EO})_6\sim\text{COO}^-$  monolayer could also facilitate incorporation of the tNB molecules into the GNR surface in the second step of our method.

### 2.3.3 Colloidal stability

Extinction spectroscopy analysis and Scanning electron microscopy (SEM) characterization. A commonly used technique to monitor gold nanoparticles modification is extinction spectroscopy.<sup>69, 75</sup> The position of the extinction band is influenced by the nanoparticle size,<sup>186, 187</sup> shape,<sup>186, 187,</sup> flocculation,<sup>188</sup> and dielectric constant of the particles and medium.<sup>177, 187, 188</sup> In the modification of the nanoparticle surface with organic molecules the dielectric constant of the surrounding medium is changed, which in turn affects the LSPR band position. This sensitivity towards changes in the dielectric constant of the surrounding medium upon addition of organic molecules to the nanoparticle surface can be employed as a diagnostic tool to verify a successful surface modification. This is demonstrated by equation 2-01 that describes the effect of changes in refractive index and adsorbed molecules thickness on the surface on the shift in  $\lambda_{\text{max}}$ .<sup>75</sup> The dielectric constant is the square of the complex refractive index.<sup>189</sup>

$$\Delta\lambda \approx m (n_{\text{adsorbate}} + n_{\text{medium}}) (1 - e^{-2d/\lambda d}), \quad (2-01)$$

Here,  $\Delta\lambda$  is the wavelength shift,  $m$  is the sensitivity factor (nm /refractive index units),  $n$  refer to the refractive index of either the adsorbate or the surrounding

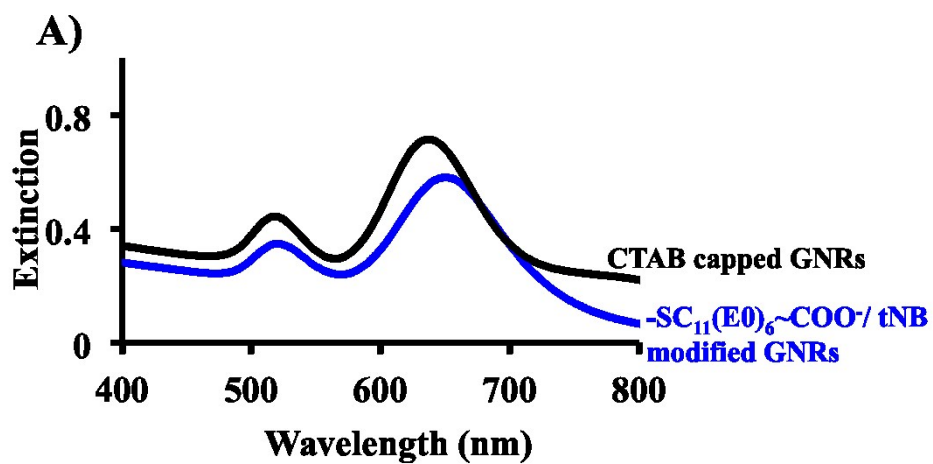
medium,  $d$  is the adsorbed molecules thickness (nm) and  $l_d$  is the electromagnetic field decay length (nm). Typically, the refractive index of an organic monolayer is 1.5-1.6<sup>125, 190</sup>

Extinction spectroscopic results provide evidence for successful replacement of CTAB with a mixed thiolate layer of  $-\text{SC}_{11}(\text{EO})_6\sim\text{COO}^-/\text{tNB}$  as well as an indication of the colloidal stability of the modified GNRs. Figure 2.05A contains the extinction spectra of CTAB coated and mixed thiolate layer coated GNRs. The CTAB coated rods exhibit a transverse plasmon band at 523 nm and a longitudinal band at 646 nm. These same bands were observed at 526 nm and 654 nm, respectively, for the  $-\text{SC}_{11}(\text{EO})_6\sim\text{COO}^-/\text{tNB}$  coated GNRs. The shifts in the localized surface plasmon resonance bands clearly indicated a variation in the organic coating. However, the exact origin of the shift was unclear. We hypothesized that the stronger interaction of the thiolate layer, along with the tighter chain packing, results in a film with a slightly higher refractive index. Also, the rapid exchange of CTAB molecules on the surface with those in solution may result in a lower refractive index. The spectra in Figure 2.05A also show that the full width at half-maximum (FWHM) of the longitudinal LSPR bands for the CTAB coated and  $-\text{SC}_{11}(\text{EO})_6\sim\text{COO}^-/\text{tNB}$  modified GNR samples are  $30 \pm 2$  nm and  $35 \pm 3$  nm, respectively. This result confirmed that the mixed thiolate coated GNRs maintained their colloidal stability. As it is known that aggregation of GNRs dramatically increases the bandwidth of the longitudinal band.

SEM imaging can also assess the aggregation for nanoparticles at various stages of surface modification.<sup>191-193</sup> For example, previous studies presented SEM images showing the tendency for the nanorods to self-assemble particularly in a side-to-side fashion which was driven by reducing the CTAB concentration during sample drying.<sup>194</sup> The self-assembly is theorized to be driven by the hydrophobic force of the coating molecules to minimize their exposure to water.<sup>195-197</sup> The SEM image in Figure 2.05B image investigates the degree of dispersion of the mixed thiolate coated GNRs. Figure 2.05B does not reveal a particular pattern of self-assembly of the GNRs due to CTAB exchange and / or drying. Thus, we can conclude that the  $-\text{SC}_{11}(\text{EO})_6\sim\text{COO}^-/\text{tNB}$  coated GNRs are not aggregated and maintained their colloidal stability, likely by steric interactions between the alkyl chains and / or electrostatic repulsion of dissociated  $\sim\text{COO}^-$  groups. These results support the zeta potential electrostatic stability.

#### 2.3.4 *Surface enhanced Raman scattering (SERS)*

To further characterize the GNR surface, SERS spectra were recorded for three GNR samples including; CTAB capped GNRs,  $-\text{SC}_{11}(\text{EO})_6\sim\text{COO}^-$  modified GNRs and  $-\text{SC}_{11}(\text{EO})_6\sim\text{COO}^-/\text{tNB}$  modified GNRs, which are left to air-dry on silica wafers. In this work, SERS spectra for three GNRs samples were collected to study the replacement of Raman signals of CTAB cap with the



B)

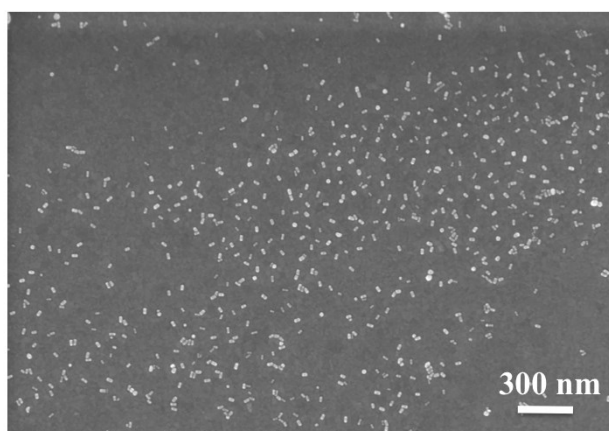


**Figure 2.05.** A) UV-visible extinction spectra collected for GNRs, aspect ratio 2.4 before and after modification with  $-\text{SC}_{11}(\text{EO})_6\sim\text{COO}^-$  and tNB. B) SEM image of  $-\text{SC}_{11}(\text{EO})_6\sim\text{COO}^-/\text{tNB}$  modified GNRs.

Raman fingerprint of tNB. Previously, it was reported that the SERS spectrum of CTAB capped GNRs displayed three specific Raman bands with an intense Au-Br band at  $183\text{ cm}^{-1}$  and two bands at  $760$  and  $1444\text{ cm}^{-1}$  for  $\text{H}_2\text{CN}^+(\text{CH}_3)_3$  symmetric stretching vibration and  $(\text{CH}_2)_n$  scissoring vibration respectively, but they were significantly weak.<sup>114, 198, 199</sup>

Figure 2.06 presents SERS spectra for three GNR samples before and after each modification step. An intense Raman signal of Au-Br at  $183\text{ cm}^{-1}$  was recorded for the CTAB capped GNR sample. This strong Au-Br Raman signal for the CTAB was significantly decreased for  $-\text{SC}_{11}(\text{EO})_6\sim\text{COO}^-$  modified GNRs. However, no characteristic vibration modes for the CTAB were observed in the SERS spectrum for the  $-\text{SC}_{11}(\text{EO})_6\sim\text{COO}^-/\text{tNB}$  modified GNRs. Intense Raman fingerprint signals for tNB molecule were observed for the modified  $-\text{SC}_{11}(\text{EO})_6\sim\text{COO}^-/\text{tNB}$  GNR sample. This data demonstrates significant exchange of the CTAB by  $-\text{SC}_{11}(\text{EO})_6\sim\text{COO}^-$  molecules at the first step and then exchange of the residual CTAB by tNB at the second step of the modification scheme. These results were in agreement with XPS analysis (Figure 2.02).

Comparing the peak position for both Raman spectra of powder tNB and  $-\text{SC}_{11}(\text{EO})_6\sim\text{COO}^-/\text{tNB}$  modified GNRs supports the modification method. Table 2.2 summarizes the Raman peak assignments for tNB in powder and after being incorporated into the GNR surface. Many of the bands in the powder spectrum

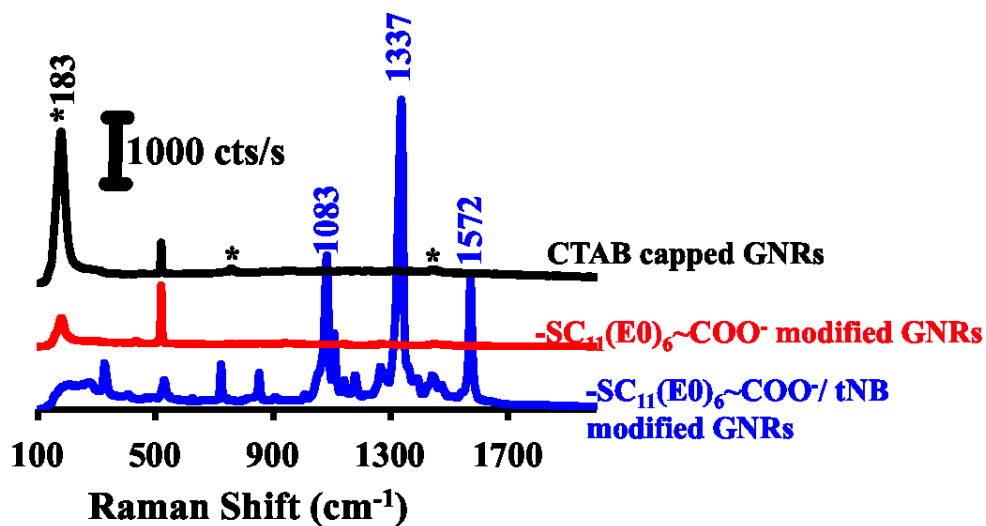


**Figure 2.06.** SERS spectra on CTAB capped,  $-\text{SC}_{11}(\text{EO})_6\text{-COO}^-$  and  $-\text{SC}_{11}(\text{EO})_6\text{-COO}^-/\text{tNB}$  coated GNRs of aspect ratio 2.4. Three GNR samples were drop casting to air-dry on silica wafer. A 785 nm laser was used to collect the SERS spectra at 14 mW laser power and integration time of 10 s. Star bands at 760 and 1444  $\text{cm}^{-1}$  are assigned for  $\text{H}_2\text{CN}^+(\text{CH}_3)_3$  symmetric vibration and  $(\text{CH}_2)_n$  scissoring vibration respectively. The spectra were offset for clarity.

were assigned in the spectrum after incubation of  $-\text{SC}_{11}(\text{EO})_6\sim\text{COO}^-$  modified GNR in tNB solution, though some have undergone a small change in position. For instance, the symmetric stretch of the nitro group has shifted from 1342 to 1337  $\text{cm}^{-1}$ , and the ring vibration mode has moved from 1576 to 1572  $\text{cm}^{-1}$ .<sup>115, 200-202</sup> The C-S bending mode at 325  $\text{cm}^{-1}$  and C-S stretching mode at 438  $\text{cm}^{-1}$  in the normal Raman spectrum of tNB powder have been shifted to 330  $\text{cm}^{-1}$  and 433  $\text{cm}^{-1}$ . These shifts were indicative of interactions between the adsorbates and with the gold surface.<sup>203</sup>

This suggests that  $-\text{SC}_{11}(\text{EO})_6\sim\text{COO}^-$  adsorbs first on (111) crystal faces of the GNR, which is free from any CTAB molecules. After that,  $-\text{SC}_{11}(\text{EO})_6\sim\text{COO}^-$  displaces CTAB on other faces. In the second step of the modification scheme, tNB molecules displace the remaining of the CTAB on (110) crystal faces. Also, tNB molecules could be incorporated into the defaults of  $-\text{SC}_{11}(\text{EO})_6\sim\text{COO}^-$  self-assembled monolayer (SAM).

The previously reported SERS signals were collected from tNB<sup>142, 204</sup> and other Raman reporters<sup>59, 205</sup> incorporated into the GNR surface directly in presence of CTAB. However, in this work CTAB was replaced by a mixed thiolate layer of  $-\text{SC}_{11}(\text{EO})_6\sim\text{COO}^-$  and tNB. The thiolate ligand such as  $-\text{SC}_{11}(\text{EO})_6\sim\text{COOH}$  introduced anchor points to the GNR surface to be further conjugated with biological molecules via its terminal carboxylic acid groups as will be discussed in the Chapter 4.

**Table 2.2.** SERS peak frequencies and assignments for 4-nitrobenzenethiol from pure powder and after adsorption on GNRs,  $\delta$ = bending,  $\nu$ = stretch and  $\nu_s$ = symmetric stretch.

Peak frequency/cm <sup>-1</sup> Pure powder	Peak frequency/cm <sup>-1</sup> tNB on gold nanorods	Mode
-	275	Au-S
325	330	$\delta$ (C-S)
737	724	C-H & C=C wagging
856	853	(NO <sub>2</sub> ) scissoring
933 (w)	933 (w)	C-H and C-C wagging
1010 (w)	1010 (w)	Ring breathing
1089	1083	$\nu$ (C-S)
1111	1109	Ring $\nu$ (NO <sub>2</sub> )
1179	1176	$\delta$ (C-H)
1342	1337	$\nu_s$ (NO <sub>2</sub> )
1576	1572	$\nu$ (C=C)

## 2.4 Conclusions

A method has been developed to displace the CTAB layer on GNRs with a mixed thiolate layer that provides enhanced Raman signals. The degree of the CTAB exchange was demonstrated by XPS analysis and supported by zeta potential measurements. HRTEM images were used to measure the thickness of the  $-\text{SC}_{11}(\text{EO})_6\text{-COO}^-$  coating. The high-yield of the functionalized GNRs was confirmed by the colloidal stability, which was examined by UV-visible extinction spectroscopy and SEM. Moreover, the characteristic SERS spectrum of tNB incorporated onto the GNR surface as well as disappearance of Raman bands from CTAB illustrated replacement of CTAB and incorporation of tNB molecules onto the GNR surface. The strong SERS potential of the  $-\text{SC}_{11}(\text{EO})_6\text{-COO}^-/\text{tNB}$  modified GNR and the simplicity of their preparation following the proposed scheme could guarantee their integration as SERS labels in biosensing applications as discussed in Chapter 4 and 5.

### 3 Chapter III

---

## Effect of aspect ratio on the surface enhancement Raman scattering of 4-nitrobenzenethiolate adsorbed on gold nanorods

### 3.1 Introduction

In Chapter 2 the modification of gold nanorods (GNRs) with 2-(2-{2-[2-(2-[2-(11-mercapto-undecyloxy) -ethoxy] -ethoxy) -ethoxy] -ethoxy} -ethoxy) -ethoxy -acetic acid ( $\text{HSC}_{11}(\text{EO})_6\sim\text{COOH}$ ) and 4-nitrobenzenethiol (tNB) was introduced. The replacement of CTAB coating of GNRs with  $-\text{SC}_{11}(\text{EO})_6\sim\text{COO}^-$  and tNB was thoroughly characterized, and the surface enhanced Raman scattering (SERS) of tNB was measured. This chapter will serve as an extension that compares the SERS response of four-different aspect ratio GNRs and 30 nm diameter spherical gold nanoparticles prepared following the scheme illustrated in Figure 2.01. The motivation behind this study is to identify a suitable aspect ratio of GNR for optimal sensing in a variety of biosensing applications.<sup>59, 76, 206</sup>

The longitudinal localized surface plasmon resonance (LSPR) band of GNRs can be tuned by different aspect ratios.<sup>145, 158, 207, 208</sup> This promotes the experimental investigation of the SERS enhancement due to the influence of the combination of the three factors. First is the LSPR extinction peak position when it is red-shifted towards the laser excitation wavelength. This is because the on-resonance field enhancement at the surface of nanoparticles (NPs) can increase

the Raman signal intensity of localized molecules by several orders of magnitude.<sup>94, 158, 209-212</sup> Second is the shape of gold nanorods (GNRs) and the presence of corners.<sup>213</sup> The theoretical calculated electric field distribution around gold nanoparticles (GNPs) of arbitrary shape demonstrated stronger localized electric field than that for spherical GNPs<sup>24, 38, 214, 215</sup> Because SERS enhancement is proportional to the fourth power of the localized electric field, molecules within ~10 nm of the metal surface can have their Raman active band intensities increase by 6-10 orders of magnitude.<sup>90, 98</sup> Third is the larger excitation coefficient calculated for GNRs than that for nanospheres.<sup>216</sup>

Orendorff and coworkers demonstrated that overlapping of the excitation wavelength with the longitudinal LSPR contributed an additional 10-10<sup>2</sup> enhancement in SERS intensity.<sup>217</sup> However, they used GNRs with only two-different aspect ratios for their study. For that, their study was limited to present the SERS enhancement factor for on and off resonance and lacked the study of aspect ratio effect on SERS enhancement. Other studies of the SERS response of metal NPs employ surface coatings such as silica or polyelectrolytes layers (as introduced in Chapter 1) to trap the Raman reporter molecules on the surface, and provide stability of the nanoparticles.<sup>56, 105, 132, 217-219</sup> For example, Murphy and coworkers synthesized GNRs of six-different aspect ratios in order to obtain longitudinal LSPR bands in the range of 600-800 nm.<sup>219</sup> Methylene blue (MB) trapped-coated with polyelectrolyte multilayer, generated the Raman spectra used to study the SERS dependence on aspect ratio. The authors noted differences

between simulated and experimental SERS spectra. The area of concern regarding this surface coating approach was uncertainty of the location of the Raman reporter molecules within the coating thickness. In the molecular trapping process, some Raman reporter (MB) molecules may be located at different distance from the GNRs than others. There is a strong dependence of SERS intensity on distance from the surface as shown in

$$I_{\text{SERS}} = (a + r / a)^{-10}, \quad (3-01)$$

Where  $I_{\text{SERS}}$  is the intensity of Raman mode,  $a$  is the average magnitude of the electromagnetic field enhancing, and  $r$  is the distance between the Raman scatter and the surface.<sup>24, 220</sup> Thus any variation in the distance between the Raman reporter molecules and the GNR surface will lead to large variations in the SERS intensities.

Here, we utilized tNB molecules directly attached to the GNR surface of four-different aspect ratios following the scheme in Figure 2.01. In our scheme, we overcome the variation in SERS enhancement due to uneven deposits for coating material<sup>219</sup> over the CTAB capped GNR surface that may result in significant difference in the study of aspect ratio dependence on SERS. We will investigate the SERS dependence on longitudinal LSPR frequency by using GNRs of four-different aspect ratios, which provide longitudinal LSPR bands at wavelength ranging from 617 nm to 714 nm in order to study the optimal Raman intensity using a 780 nm laser excitation wavelength. The results will be compared with Raman intensity for 30 nm spherical GNPs with LSPR ~524 nm.

## 3.2 Experimental

### 3.2.1 Reagents and Materials

Cetyltrimethylammonium bromide (CTAB) capped GNRs with aspect ratios (l/d) of 2.1, 2.4, 2.8, and 3.2 were from NanoPartz, Loveland CO, U.S.A. The specific characterization of these GNRs, including the number of particles per each mL, LSPR peak position, molar extinction coefficient, length (l) and diameter (d) for each GNR is summarized in Table 3.1. Citrate capped  $30 \pm 2$  nm diameter spherical gold nanoparticles were purchased from BBInternational (Grand Forks, U.S.A.) with a concentration of  $1.04 \times 10^{10}$  particles/mL. 2-(2-{2-[2-(2-[2-(11-mercapto-undecyloxy)-ethoxy]-ethoxy)-ethoxy]-ethoxy}-ethoxy)-ethoxy-acetic acid,  $\text{HSC}_{11}(\text{EO})_6\text{-COOH}$ , MW = 526.73 g/mol) was obtained from ProChimia. A solution of 40 mM  $\text{HSC}_{11}(\text{EO})_6\text{-COOH}$  was prepared in deionized water from a Millipore Milli-Q Plus purification system. 4-nitrobenzenethiol (98%), was from Aldrich, Canada. 4 mM 4-nitrobenzenethiol (tNB) solution was freshly prepared in 20 v/v% ethanol (Quantum Chemical, Victoria, Australia) and 80v/v % deionized water.

### 3.2.2 Preparation of GNRs as SERS labels

CTAB exchange by  $-\text{SC}_{11}(\text{EO})_6\text{-COO}^-$ . CTAB capped GNR solutions were purified from excess CTAB molecules in solution by centrifugation once at

**Table 3.1.** Summary of specific characterization measurements for 30 nm spherical GNPs and GNRs of four different aspect ratios. l and d are the length and the diameter of GNRs, respectively.

<b>Nanoparticle</b>	<b>Aspect ratio 1.0<sup>a</sup></b>	<b>Aspect ratio 2.1</b>	<b>Aspect ratio 2.4</b>	<b>Aspect ratio 2.8</b>	<b>Aspect ratio 3.2</b>
<b>LSPR<sup>b</sup></b>	524 nm	T=527nm L=617 nm	T=526 nm L=640 nm	T= 526 nm L= 681 nm	T=525 nm L=714 nm
<b>Number of particles/ ml<sup>c</sup></b>	$1.04 \times 10^{10}$	$9.33 \times 10^9$	$8.60 \times 10^9$	$1.70 \times 10^9$	$8.53 \times 10^8$
<b>Dimensions/ nm <math>\pm</math> SD<sup>d</sup></b>	Diameter 30 $\pm$ 2	l =51 $\pm$ 1, d=25 $\pm$ 3	l=59 $\pm$ 2, d=25 $\pm$ 2	l=65 $\pm$ 3, d=23 $\pm$ 2	l=71 $\pm$ 2, d=22 $\pm$ 1
<b>Molar extinction<sup>e</sup> (M<sup>-1</sup> cm<sup>-1</sup>)</b>	$4.15 \times 10^8$	$1.03 \times 10^9$	$2.29 \times 10^9$	$4.58 \times 10^9$	$1.14 \times 10^{10}$

<sup>a</sup> Aspect ratio 1.0 for 30 nm spherical GNPs.

<sup>b</sup> The listed values are averages based on n=3 measurements for LSPR values, T is the transverse plasmon and L is the longitudinal plasmon.

<sup>c,e</sup> The listed values are calculated measurements provided by NanoPartz.

<sup>d</sup> The listed values of the GNR dimensions (l is the length, d is the diameter) are averages based on n= 3, AFM measurements.

8000 rpm for 10 min at 25 °C in an Eppendorf a5417R microcentrifuge. The pellets of GNRs were mixed with 1 mL of 40 mM HSC<sub>11</sub>(EO)<sub>6</sub>~COOH, sonicated for 1 min and left to incubate for 24 h at room temperature with intermittent gentle shaking. The GNRs were then sonicated for 1 min and separated from solution *via* centrifugation once at 8000 rpm for 10 min. The supernatant of excess HSC<sub>11</sub>(EO)<sub>6</sub>~COOH was carefully removed with a micropipette without disturbing the pellets, and the pellets were dispersed in 1 mL of deionized water.

Incorporation of tNB onto the GNR surface. The HSC<sub>11</sub>(EO)<sub>6</sub>~COOH modified pellets of the GNRs were resuspended in 1 mL of 4 mM tNB. Then the GNRs suspension was sonicated for 1 min and allowed to stand for 24 h at room temperature with intermittent gentle shaking. The excess tNB and HSC<sub>11</sub>(EO)<sub>6</sub>~COOH in the supernatant solution were removed *via* centrifugation once at 8000 rpm for 10 min and the pellets were resuspended to 1 mL in deionized water. The modified GNRs maintain their colloidal stability for at least one month at 7 °C.

### 3.2.3 Instrumentation

Atomic force microscopy (AFM) measurements. Dimensions of the CTAB capped GNRs from NanoPartz, Loveland CO, U.S.A. were measured with atomic force microscopy (AFM). The summary of the measurements is in Table 3.1. Topographical AFM images of immobilized gold nanorods of aspect ratios 2.1, 2.4, 2.8 and 3.2 were captured. Line scans are measured across the width of

these GNRs. Figure 3.01A shows a topographical AFM image of GNR of aspect ratio 2.4 and the line scan measured across the width shown in Figure 3.01B. The measurements were carried out using a Multimode instrument from Digital Instruments (Santa Barbra, CA). Images were collected with aluminum coated silicon cantilevers (Asylum AC240TS) with nominal tip radius of <10 nm, spring constant of 2 N/m and resonant frequency of 70 kHz for tapping mode.

UV-vis extinction spectroscopy measurements. UV-visible extinction spectra for CTAB coated GNRs, citrate capped GNPs and  $-SC_{11}(EO)_6\sim COO^-$ /tNB modified GNPs were collected to show colloidal stability and probe surface plasmon shift due to the aspect ratio and changes in coating chemistry. Samples were prepared in aqueous solution spectra and were collected on a Perkin-Elmer Lambda 35 UV/VIS/NIR spectrometer with a 10 mm optical path length. The UV-vis spectra were scanned from 400 to 1100 nm with a scan rate of 960 nm/min. Deionized water was used as the blank.

Scanning electron microscopy (SEM) measurements. SEM images show the degree of the GNRs dispersion after modification. SEM sample was prepared by drop casting 20  $\mu$ L of the cleaned modified GNRs on a clean gold-coated microscope slide (200 nm thick films) and left to air-dry. SEM images were collected using a Hitachi S44800 FE-SEM system (Hitachi Scientific Equipment). Image acquisition on the Hitachi SEM was carried out with a 20.00 kV accelerating voltage and a 15  $\mu$ A emission current. The working distance was

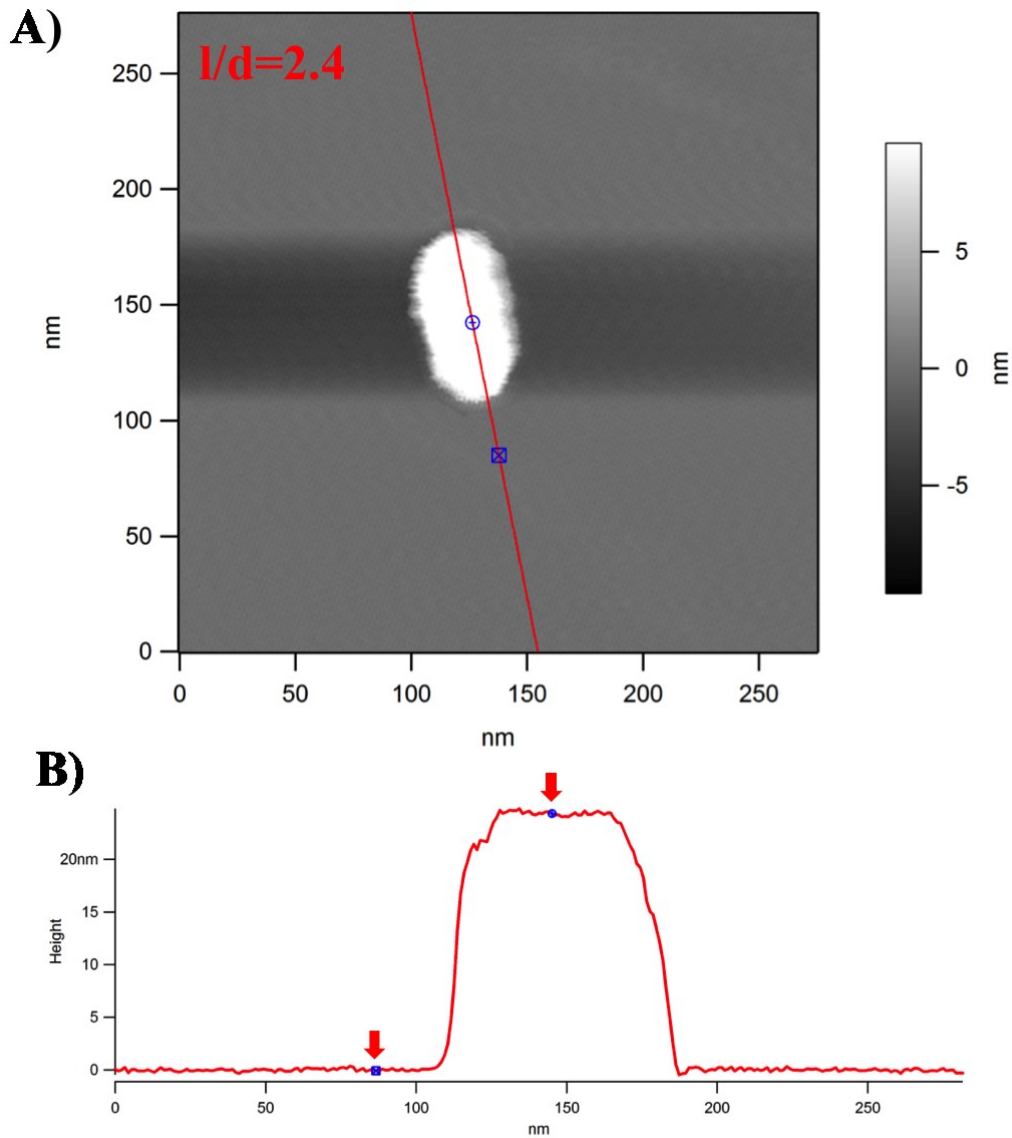


**Figure 3.01.** Atomic force microscopy (AFM) image of one GNR of aspect ratio 2.4 immobilized on a 200 nm Au substrate. A) A topographical image with line scans traces marked. B) Line scans across the width of the GNR shows  $25 \pm 1$  nm height (presented by two red arrows).

approximately 8-10 mm.

Surface enhanced Raman scattering (SERS). SERS spectra for five different size GNSs with aspect ratio ( $l/d$ ) 1, 2.1, 2.4, 2.8 and 3.2 modified with  $-\text{SC}_{11}(\text{EO})_6\sim\text{COO}^-/\text{tNB}$  were recorded in aqueous solutions with a Thermo Scientific - mega XR dispersive Raman microscope equipped with high performance near IR diode (780 nm) lasers with a 2  $\mu\text{m}$  spot size. Laser power at the sample was 30 mW, and the integration time was 10 s.

### **3.3 Result and discussion**

Investigate the dependence of SERS enhancement on the aspect ratio, GNRs of aspect ratio 2.1, 2.4, 2.8 and 3.2 and 30 nm spherical GNPs were studied. This range of aspect ratio was chosen to have longitudinal LSPR with a variable degree of plasmon overlap with the 780 nm excitation wavelength. Note that previous reports describe SERS activity on primarily aggregated GNRs,<sup>114</sup> where determining the dependence of SERS on the GNR optical properties is difficult due to plasmon coupling contribution.<sup>101, 132, 221-223</sup> To determine the electromagnetic (EM) contributions to SERS enhancement from the aspect ratio alone, one must minimize plasmon coupling. We thus used dilute colloidal solutions of modified GNRs to minimize particle-particle coupling.

### 3.3.1 Colloidal stability

Extinction spectroscopy. As discussed in Chapter 2, extinction spectroscopy is a common technique was used to monitor GNPs modification.<sup>69,</sup>  
<sup>75</sup> The sensitivity towards changes in the dielectric constant of the surrounding medium upon exchange or addition of organic molecules to the nanoparticle surface can be used to verify a successful surface modification. Although our modification procedure was thoroughly characterized in Chapter 2, we recorded extinction spectra here to ensure that all the nanorods and spherical NPs studied were successfully modified. The LSPR of the  $30 \pm 2$  nm GNPs results in a strong excitation band in the visible region near 524 nm, as shown in Figure 3.02A. As noted above, GNRs have a characteristic transverse plasmon band in the visible region near  $525 \pm 2$  nm and longitudinal plasmon band in the near infrared (NIR) region that can be tuned by changing the aspect ratio ( $l/d$ ) of the GNRs.<sup>187, 208</sup> Figure 3.02A-E presents the experimentally measured extinction spectra for 30 nm citrate capped spherical GNPs and CTAB capped GNRs of aspect ratio 2.1, 2.4, 2.8 and 3.2 before and after labeling with tNB in a mixed monolayer of  $-\text{SC}_{11}(\text{EO})_6\text{-COO}^-$ . All modified GNPs and GNRs exhibit extinction bands that are red-shifted from the original, citrate-capped GNPs and CTAB capped GNRs. The LSPR band for  $30 \pm 2$  nm GNPs is red-shifted about  $5 \pm 1$  nm after modification; however, the longitudinal and transverse LSPRs for other four GNRs are shifted  $8 \pm 2$  nm and  $3 \pm 1$  nm, respectively after modification. These observations agreed with previous studies, which showed red

shift in the LSPR band position due to changes in the surrounding dielectric constant and coating chemistry.<sup>54, 186, 224</sup>

Other aspects of the extinction curves shown in Figure 3.02 include extinction magnitudes and LSPR broadening. We noticed that the intensity of the surface plasmon band for 30 nm GNPs and GNRs of four-different aspect ratio modified with  $-\text{SC}_{11}(\text{EO})_6\text{-COO}^-$  and tNB is slightly lower than that for unmodified GNPs and GNRs. This was due to loss of a portion of the modified GNPs and GNRs during separation from unreacted  $\text{HSC}_{11}(\text{EO})_6\text{-COOH}$  and/ or tNB via centrifugation. However, the  $-\text{SC}_{11}(\text{EO})_6\text{-COO}^-/\text{tNB}$  modified GNRs that were resuspended remain stable in the aqueous solution. In regards, to the band broadening, all curves exhibit a small  $3 \pm 1$  nm width difference for longitudinal LSPR (full-width-half-maximum, FWHM) before and after modification. This is an indicator for the absence of significant aggregation during surface modification.<sup>177</sup>

Scanning electron microscopy (SEM) characterization. SEM images were collected to ensure the colloidal stability of the spherical GNPs and the GNRs after modification. Figure 3.03 shows SEM images for GNRs of aspect ratio 2.4 and 2.8 after modification with  $-\text{SC}_{11}(\text{EO})_6\text{-COO}^-$  and tNB. There is no noticeable aggregation in any of the SEM images for 30 nm nanospheres and GNRs modified samples. SEM samples were left to air-dry and that should be considered, when examining the SEM images. Previous reports describe the induced aggregation of nanoparticles by solvent evaporation that may explain

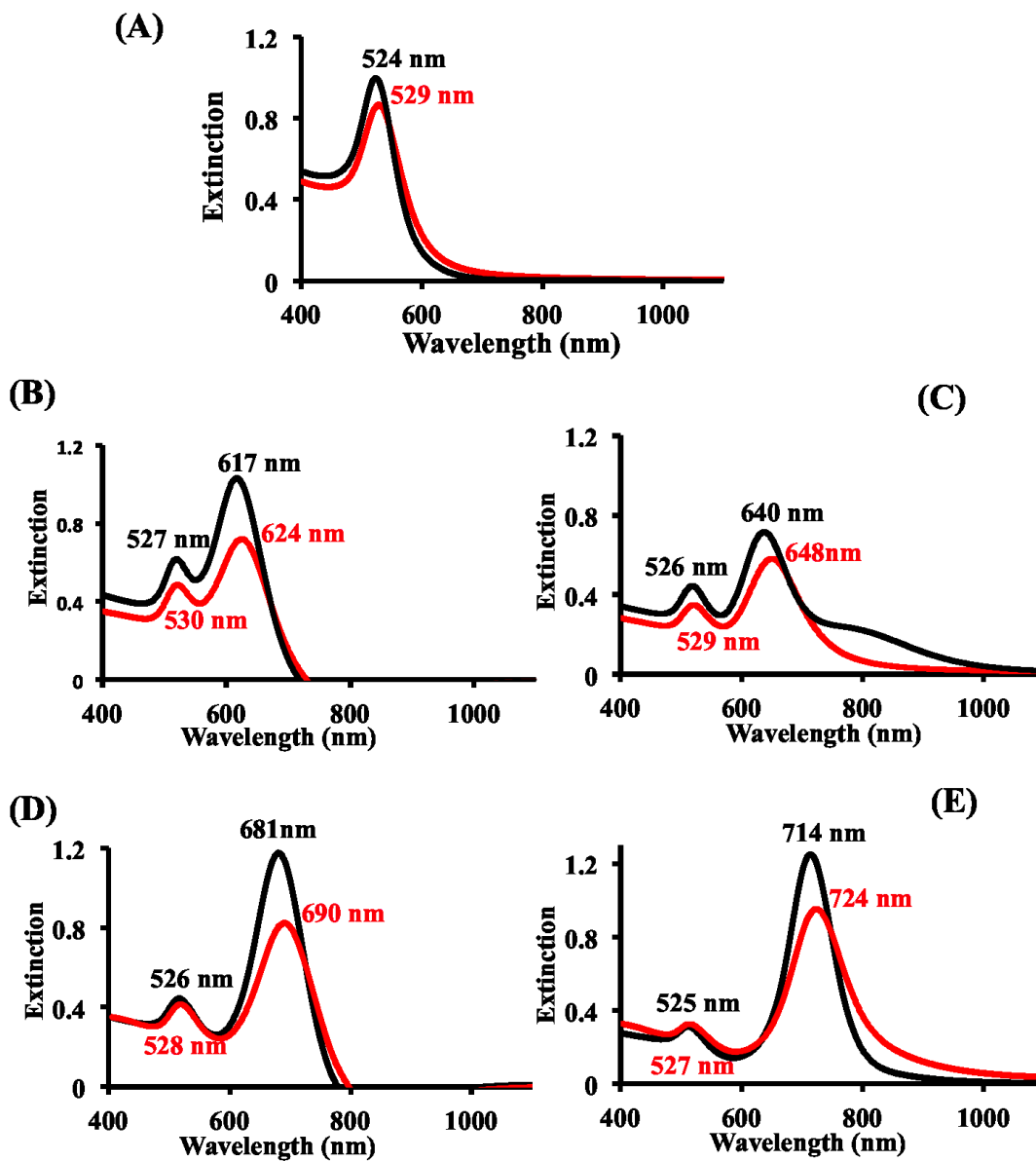


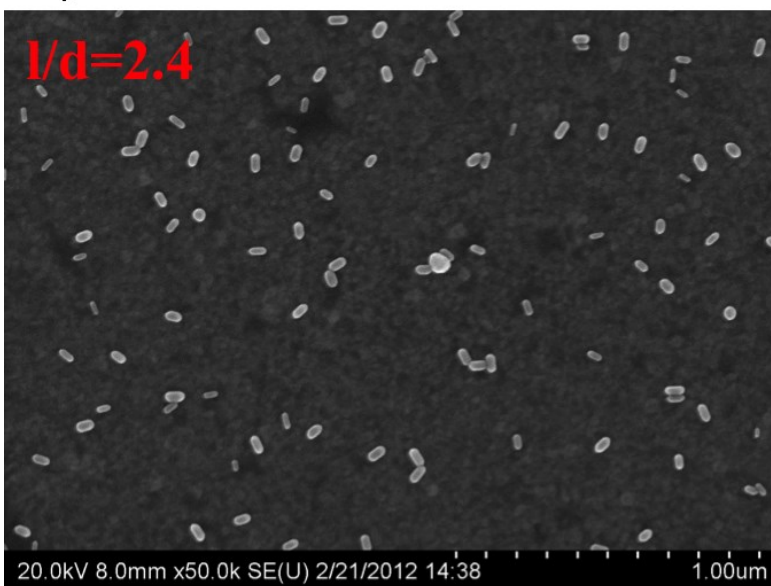
**Figure 3.02.** Experimental extinction spectra for A) citrate capped 30 nm diameter GNPs, GNRs of four-different aspect ratios B) 2.1, C) 2.4, D) 2.8, and E) 3.2 before and after labeling with tNB in a mixed thiolate layer with  $-\text{SC}_{11}(\text{EO})_6\sim\text{COO}^-$ .

presence of some dimers, trimers or more in the presented SEM images.<sup>225</sup> We have found that for all modified GNRs and GNPs with  $-\text{SC}_{11}(\text{EO})_6\sim\text{COO}^-$  and tNB maintains their colloidal stability in solutions at 7 °C for at least one month with no evidence of aggregation.

### 3.3.2 Surface enhanced Raman scattering (SERS)

The SERS spectra for tNB adsorbed on GNP of five different aspect ratios are shown in Figure 3.04. The effect of number of GNPs on the SERS intensities was also examined and is shown in Figure 3.05. The number of tNB molecules on each particle will depend on the surface area of the nanoparticle. For that reason, we accounted for surface area by presenting plots of the Raman intensity of the symmetric stretch of the nitro group of tNB at  $\sim 1337\text{ cm}^{-1}$  versus surface area  $\times$  number of particles/mL (Figure 3.05). The number of particles per mL was calculated from a series of dilutions for the stock solutions of GNPs and GNRs with known concentrations as provided by manufacturer. We calculated the surface area for each GNR by taking the average particle dimensions measured by AFM (Figure 3.01). We observe a linear relationship ( $R^2 > 0.990$ ) for the chosen range of dilutions for the five plots. This is also portrayed by the slopes of the curves for the various aspect ratios, which are related to SERS sensitivity. The summary of least square fits equation are presented in Table 3.2. The main feature of the plots in Figure 3.05 is the larger Raman response for the higher aspect ratio GNRs ( $l/d=3.2$ ). For example at the particles number/mL  $\times$

**A)**



**B)**

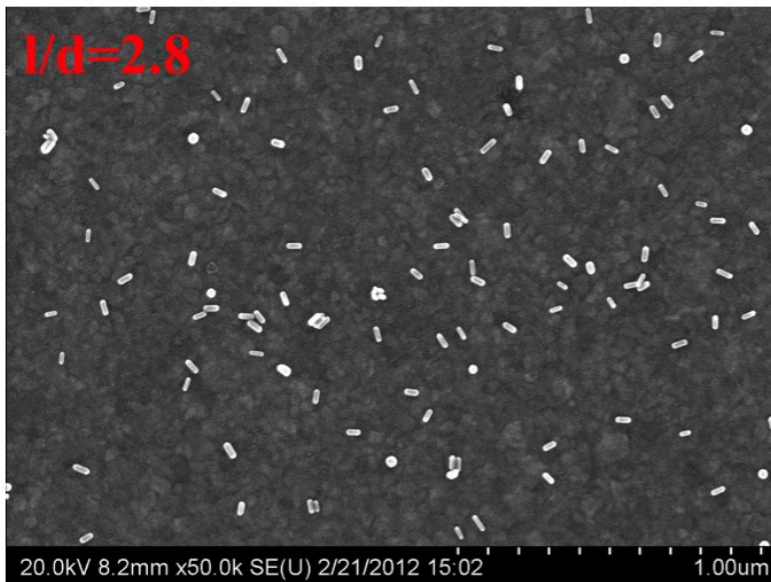


**Figure 3.03.** SEM images show well-dispersed gold nanorods of aspect ratio ( $l/d$ )

A) 2.4 and B) 2.8 after modification.

surface area of  $2 \times 10^{13}$ , the response is 10 fold higher for GNRs of aspect ratio 3.2 compared to GNRs of aspect ratio 2.1.

Usually, the SERS enhancement factor (EF) is estimated using:<sup>141, 142</sup>

$$EF = [I_{\text{SERS}}] / [I_{\text{Raman}}] \times [M_{\text{bulk}}] / [M_{\text{ads}}] \quad (3-02)$$

where,  $M_{\text{bulk}}$  is the number of Raman reporter molecules sampled in the bulk,  $M_{\text{ads}}$  is the number of Raman reporter molecules adsorbed and sampled on the SERS-active substrate,  $I_{\text{SERS}}$  is the intensity of a vibrational mode in the surface-enhanced spectrum, and  $I_{\text{Raman}}$  is the intensity of the same mode in the Raman spectrum. In our system, the number of tNB molecules adsorbed on the GNRs is unknown. Thus applying equation 3.02 here is a problematic. We compare the slopes for the plots of SERS intensity magnitudes of the symmetric stretch of the nitro group at  $1337 \text{ cm}^{-1}$  versus surface area  $\times$  number of particles/mL (Figure 3.05).

In Figure 3.05 using the example for tNB incorporated onto the surface of GNRs of aspect ratio 3.2 with longitudinal LSPR at 724 nm, the maximum slope value was recorded  $4 \times 10^{-9}$  cts/nm<sup>2</sup>.number of particles/mL, while the minimum slope was  $4 \times 10^{-11}$  cts/nm<sup>2</sup>.number of particles/mL for 30 nm diameter GNPs with LSPR  $\sim$ 529 nm. Based on these values, we can estimate that SERS response for GNRs with LSPR band  $\sim$ 724 nm that blue shifted from laser excitation wavelength of 780 nm was two orders of magnitude greater than those

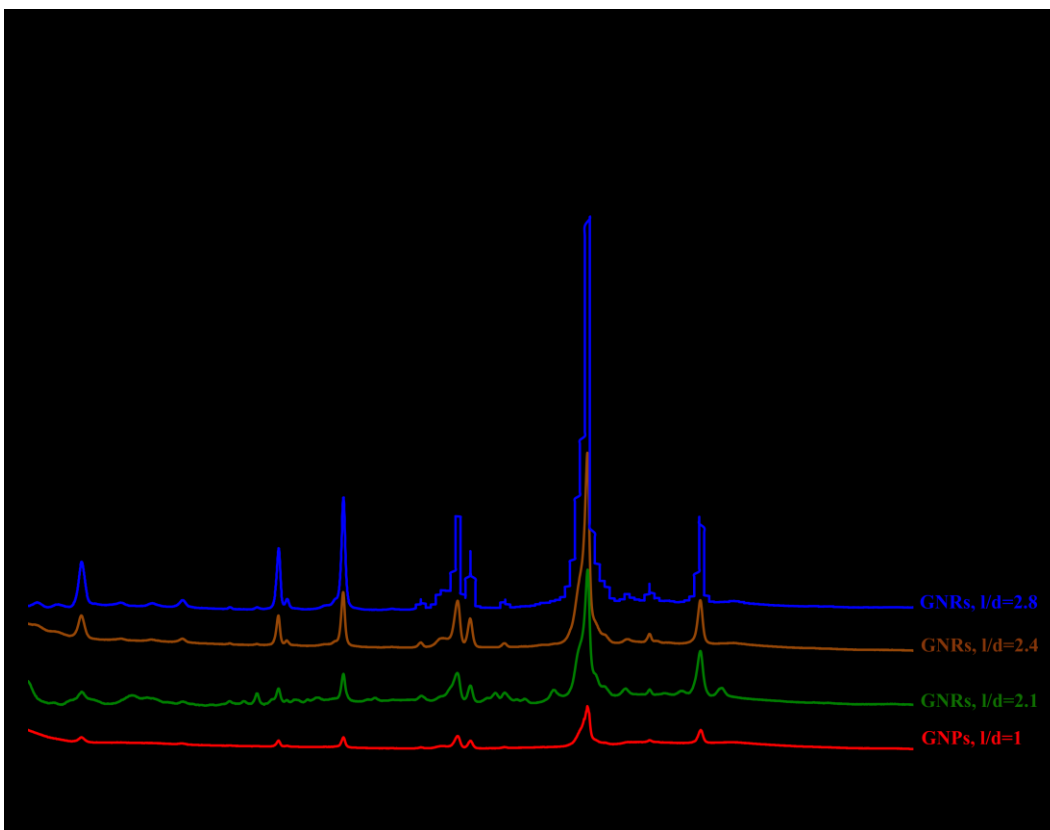


**Figure 3.04.** SERS spectra for 30 nm GNPs and four-different size GNRs of aspect ratios ( $l/d$ ) 2.1, 2.4, 2.8 and 3.2 after labeling with tNB in a mixed monolayer with  $-\text{SC}_{11}(\text{EO})_6\text{-COO}^-$ . The spectra were collected using 780 nm laser and offset for clarity.

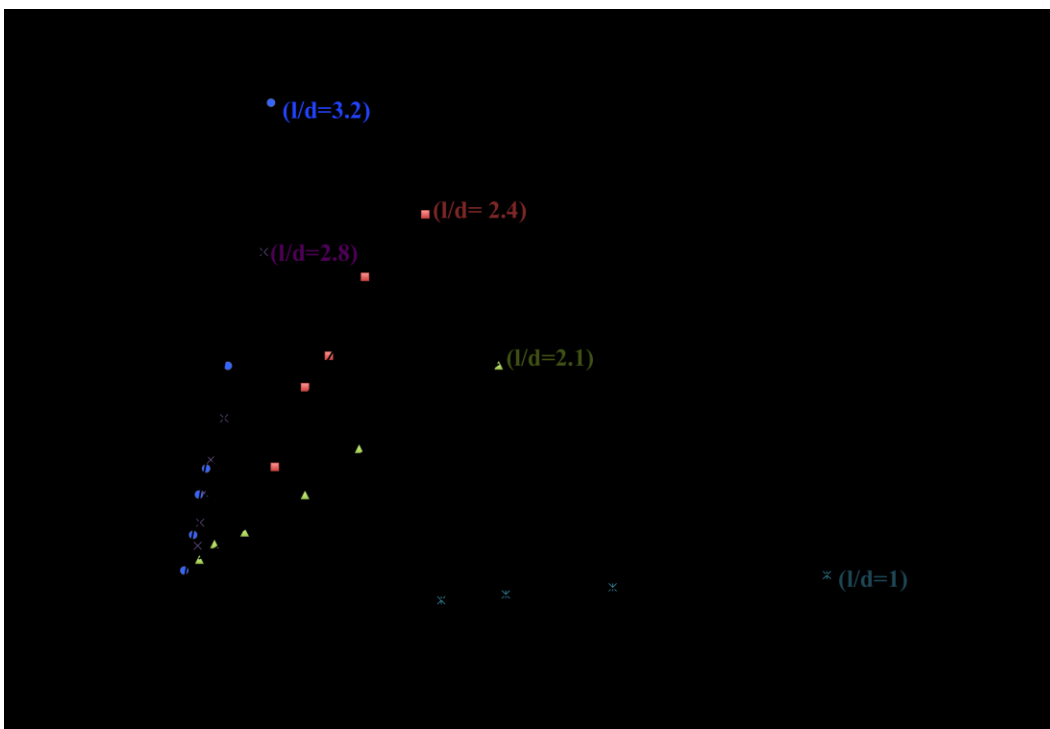


**Figure 3.05.** Plots of SERS intensity of the symmetric stretching of the nitro group at  $1337\text{ cm}^{-1}$  versus surface area  $\times$  number of particles/mL for 30 nm diameter GNPs and GNRs of four-different aspect ratios 2.1, 2.4, 2.8 and 3.2. The y-error bars represents the standard deviation for  $n=6$  measurements for each of two separate samples.

with LSPR more far from laser excitation wavelength. Also the difference in SERS response for GNRs of LSPR  $\sim 724$  nm and GNRs of LSPR  $\sim 624$  nm was one order of magnitude.

The differences observed in SERS intensity for five GNP solutions agrees more closely to the theoretical models of calculated localized electric field for metal NPs with LSPR band at different degree of overlapping with laser excitation wavelength. The calculated SERS intensity from the slopes presented in Figure 3.04 for on and off-resonance plasmon was higher by a factor of 10 to 100.<sup>114, 226-228</sup> However, previous studies that presented theoretical calculations for localized electric field at sharp points of arbitrary shape nanoparticles.<sup>24, 38</sup> They concluded that presence of corners and edges was accompanied with order of magnitude of SERS enhancement. For this reason, it was expected that the shape of the nanorods would influence the observed SERS intensity for the rods compared to SERS response for spherical NPs.

The molar extinction values for GNP solutions of different aspect ratios are presented in Table 3.1. It is clear that the molar extinction increases with aspect ratio increases. El-Sayed and co-workers have reported using theoretical calculations that the longitudinal plasmon extinction efficiency increases as aspect ratio increases.<sup>216, 229</sup> Consequently, it is predictable that extinction efficiency has an influence on the SERS signal intensity. Figure 3.05 presents SERS enhancement of one to two orders of magnitude between the GNPs of five different aspect ratios that could be considered smaller enhancement in SERS

**Table 3.2.** Summary of linear least squares fit equations for 30 nm diameter GNPs and GNRs of four-different aspect ratios studied in SERS comparison.

<b>Gold nanoparticles</b>	<b>Slope</b> cts/nm <sup>2</sup> .number of particles/mL	<b>Intercept</b>	<b>R<sup>2</sup></b>
GNRs (l/d=3.2)	$4 \times 10^{-9}$	773±12	0.996
GNRs (l/d=2.8)	$3 \times 10^{-9}$	611±22	0.990
GNRs (l/d=2.4)	$1 \times 10^{-10}$	340±17	0.991
GNRs (l/d=2.1)	$4 \times 10^{-10}$	105±11	0.997
30 nm spheres (l/d=1)	$4 \times 10^{-11}$	111±19	0.991

than what could be expected. Because the predicted SERS enhancement coming from the three theoretical models that relate the localized electric field intensity to the relative position of LSPR band to excitation wavelength, the presence of sharp points and corners of GNR surface, and the larger extinction coefficient for higher aspect ratio.

On the other hand, a number of reports demonstrate that the relative scattering to the total extinction of GNPs was not only related to their shape but also their absolute size: larger nanorods with the same aspect ratio, lead to more scattering relative to total extinction that may attenuate SERS enhancement.<sup>230</sup>  
<sup>231</sup> Others performed simulations for the relative contribution of absorption and scattering to the total extinction of the longitudinal mode to be significantly dependent on the aspect ratio of GNPs in somewhat complex manner, different from a typical linear relationship for the resonance wavelength.<sup>187</sup> Experimentally, a recent report for Murphy and coworkers has demonstrated SERS enhancement for six-different aspect ratio GNRs after trapping Raman reporter (MB) at least 5 nm from the surface using the layer-by-layer coating approach.<sup>161</sup> However, the variation in coating thickness in their study significantly affected the observed SERS intensity. Murphy and her research group demonstrated considerable extinction attenuation for SERS enhancement when designing nanoparticles SERS probes in solution. This result is in agreement with our results. Regardless of plasmon resonance frequency and sharp points at the GNR surface, the competition between SERS response and

extinction attenuation for colloidal nanoparticles in solution has an observable influence on SERS response. However to the best of our knowledge Raman enhancement of GNRs of different-aspect ratio has not been studied experimentally for directly immobilized Raman reporter onto the GNR surface in the absence of CTAB.

### 3.4 Conclusions

In this chapter SERS labels of 30 nm spherical gold nanoparticles and gold nanorods of aspect ratios 2.1, 2.4, 2.8 and 3.2 were prepared by following the proposed approach in Figure 2.01 for CTAB replacement with  $-\text{SC}_{11}(\text{EO})_6\text{-COO}^-/\text{tNB}$ . SERS experiments were done in aqueous solutions under dilute conditions in order to study the dependence of SERS enhancement on aspect ratio. This study has shown that the GNRs of aspect ratio 3.2 gives one order of magnitude greater SERS signal intensity than GNRs of aspect ratio 2.1 and two order of magnitude greater SERS intensity than 30 nm diameter spherical gold nanoparticles. Larger SERS intensity for GNRs of aspect ratio 3.2 than other GNRs of smaller aspect ratio could be explained by the position of the longitudinal LSPR frequency at  $\sim 724$  nm, which was closer to the 780 nm laser excitation wavelength than other LSPR bands. This result was attributed to greater contributions from localized electric field generated on the GNR surface related to the longitudinal LSPR band position. In addition, localized electric field is stronger at corners of the GNR surface than spherical GNPs.<sup>24, 38</sup>

However, these experimentally observed SERS intensity for the GNPs of different aspect ratios was smaller than expected. For that we concluded that SERS intensity could be attenuated by the extinction contributions of the GNPs in solutions in agreement with the observation of Murphy and coworkers.<sup>161</sup> This identifies experimentally important contributions such as LSPR band position to laser extinction wavelength, shape and extinction effects on SERS enhancement when designing tagged SERS probes in solution for optimal sensing.

## 4 Chapter IV

---

### **Gold nanorods as extrinsic Raman labels in a sandwich immunoassay**

#### **4.1 Introduction**

The biosensing field has been revitalized by the incorporation of metal nanoparticles (NPs). At the forefront of this field are spherical gold nanoparticles (GNPs). One reason for the widespread use of spherical GNPs is that their surface can be easily and efficiently modified. These GNPs as well as other metal NPs have unique optical properties that can benefit the design of a biosensor by exploiting a phenomenon called localized surface plasmon resonance (LSPR).<sup>9, 10</sup> As introduced in Chapter 1, this phenomenon refers to the oscillation of conduction electrons over the surface of the metal NP induced by the absorption of visible light. The LSPR results in a localized electric field in close proximity to the NP surface.<sup>53</sup> Many reviews are dedicated to applications of gold nanoparticles (GNPs) with different forms of labeling in vitro and in vivo.<sup>20, 31, 62, 64, 75, 232, 233</sup> LSPR biosensors utilizing GNPs have been employed to detect biotin streptavidin binding,<sup>70</sup> and a variety of different immunoglobulin G's (IgG's).<sup>71-73, 234</sup> Many other applications for GNPs in a solution based visible absorption spectroscopy analysis have been reported.<sup>235-237</sup> Conjugation of gold nanoparticles with biological molecules such as DNA, antibodies, enzyme and

others have found applications in DNA hybridization studies,<sup>238</sup> surface plasmon resonance (SPR)<sup>19, 239, 240</sup> and imaging.<sup>241</sup>

The incorporation of surface enhanced Raman scattering (SERS) in an immunoassay was first demonstrated by Rohr and co-workers in 1989 using a roughened silver film to achieve SERS.<sup>242</sup> Natan and coworkers studied the gold colloid bioconjugate applications in SERS and found that metal-protein-metal sandwiches offer benefits as reagents. Single molecule SERS based spectroscopy of hemoglobin adsorbed on 100 nm sized citrate capped colloidal nanoparticles was achieved by SERS. Nanoparticle aggregation is necessary for this effect, and the protein molecules actually bind the nanoparticle clusters together.<sup>221</sup> Other research groups have exploited surface modified GNPs to function as analytical reagents in SERS-based bioassays. In 1999, Porter and coworkers presented the first sandwich immunoassay that utilized GNPs with SERS detection.<sup>241</sup> The assay detected rabbit and rat IgG at the nano-molar level. In their work, the gold nanoparticle surface was bi-functionalized, carrying a capture-molecule to selectively bind to the analyte and a Raman active molecule (Raman reporter) used in the detection strategy in order to prepare extrinsic Raman labels (ERLs) of GNPs (as introduced in Chapter 1). The SERS response from the Raman reporter was measured and correlated to the analyte concentration. The ERLs with 30 nm GNPs were employed to detect free prostate-specific antigen from human serum,<sup>115, 140, 243</sup> various viral pathogens<sup>244</sup> and microorganisms<sup>245</sup>, and much lower molecular weight biomarkers such as a metabolite of vitamin D.<sup>246</sup>

The colloidal stability of these ERLs is a challenging factor that needs to be controlled to maintain the optical properties of GNPs.<sup>104</sup>

Generally, GNPs have distinctive optical properties that depend on their shape, size and surrounding dielectric constant.<sup>247, 248</sup> Elongated NPs have an inherently higher sensitivity to the local dielectric environment, as compared to similar sized spherical nanoparticles.<sup>249</sup> A SERS measurement for gold and silver nanoparticles has already been established for other morphologies including dendrites,<sup>250</sup> cubes,<sup>251</sup> and rods.<sup>217</sup> These nanostructures were excellent substrates for SERS because of their arbitrary shapes and the presence of sharp points and/or corners.<sup>213</sup> Some research groups extend their biosensing applications to utilize some of these nanostructures such as silver nanoprism,<sup>252, 253</sup> and gold nanowires.<sup>254, 255</sup> However, the use of gold nanorods (GNRs) as biosensors has not been widely pursued. GNRs are generally prepared with an adsorbed layer of the surfactant cetyltrimethylammonium bromide (CTAB). This layer of CTAB is difficult to displace and the conjugation of bromide to biological molecules is a challenge.<sup>178, 256</sup>

Liao and co-workers have demonstrated that CTAB can be replaced by thiol-terminated methoxypolyethyleneglycol (mPEG), which can be used to subsequently conjugate immunoglobulin G. However, the large size of thiolated PEG makes it difficult for it to reach the GNR surface due to dense CTAB bilayer and this results in an incomplete removal of CTAB molecules.<sup>255, 257</sup> Yamada and his research group reported a method for replacing the CTAB with

phospholipids by extraction with a chloroform phase. However, no bioconjugate can be formed in the presence of phospholipids.<sup>155</sup> The layer-by-layer method (previously discussed in Chapter 1) is a widely applied method for GNR surface covering with a polyelectrolyte coating that provides terminal groups for antibody conjugation onto the GNR surface.<sup>258-260</sup> Chilkoti and co-workers reported a chip-based LSPR biosensor using an immobilized layer of GNRs. The sensor had a refractive index sensitivity 5 times higher than a similar sensor based on spherical GNPs.<sup>261</sup> Wang and his research group demonstrated solution-phase based LSPR sensor for the detection of human IgG<sup>262</sup> and Microcystin LR (environmental cyanotoxin) through the end-to-end and side-to-side assembly of antibody-conjugated GNRs driven by antibody-antigen recognition.<sup>263</sup> However, this type of LSPR sensing assays, does not allow for the detection of multiple analytes simultaneously and the instrumentation has to be more sophisticated when detecting small shifts. El-Sayed reported antibodies conjugated GNRs to image human oral cancer cells. These cells assembled and aligned GNRs on its surface and intense SERS spectra of CTAB coating were presented.<sup>113</sup>

In Chapter 2, we presented a new design for GNR surface modification with a mixed thiolate layer of  $-\text{SC}_{11}(\text{EO})_6\sim\text{COO}^-/\text{tNB}$  that maintains colloidal stability in an aqueous solution and includes anchor points (carboxylic acid groups) for further functionalization with biological probes. Herein, we covalently link rabbit anti-goat IgG antibodies to the GNR surface via EDC/NHS chemistry to prevent antibody desorption during the assay, which could lead to

reduction in the signal.<sup>115</sup> The anti-goat IgG conjugated GNRs were characterized by HRTEM and UV-vis spectroscopy. The GNRs of aspect ratio 2.4 were conjugated with anti-goat IgG and utilized as ERLs in a SERS-based sandwich immunoassay to detect goat IgG. The corresponding SERS response will be presented. The SERS-based sandwich immunoassay performance was assessed by Raman microscopy and scanning electron microscopy. This will show the successful implementation of anti-goat IgG conjugated GNRs as ERLs, which are well dispersed on the surface of assay chip. The specific assembly of GNRs upon binding will be investigated that may influence the reproducibility of SERS response. Further, SEM images will illustrate the aspect of non-specific binding either as a result of the capture layer on the solid support or from the GNRs. Lastly, the limit of detection of goat IgG will be investigated for our SERS-based sandwich immunoassay.

## 4.2 Experimental

### 4.2.1 Reagent and Materials

Cetyltrimethylammonium bromide (CTAB) capped GNRs of aspect ratio 2.4 were from NanoPartz, Loveland Co. The number of gold nanorods per each mL was  $1 \times 10^{11}$ . 2-(2-{2-[2-(2-[2-(11-mercapto-undecyloxy)-ethoxy]-ethoxy)-ethoxy]-ethoxy}-ethoxy)-ethoxy)-acetic acid ( $\text{HSC}_{11}(\text{EO})_6\text{-COOH}$ ), MW= 526.73 g/ mol) was from ProChimia, Poland. A solution of 40 mM

HSC<sub>11</sub>(EO)<sub>6</sub>~COOH was prepared in deionized water from a Millipore Milli-Q Plus purification system. 4-nitrobenzenethiol (98%), was from Sigma Aldrich. 4 mM 4-nitrobenzenethiol (tNB) solution was freshly prepared in a mixture of 80% ethanol (Quantum Chemical, Victoria, Australia) and 20% deionized water. Buffer solution employed salts from Fisher Scientific Company (Ottawa, ON). Phosphate buffered saline (PBS, pH 7.4) was prepared with reagent grade 1.4 mM KH<sub>2</sub>PO<sub>4</sub> and 4.3 mM Na<sub>2</sub>PO<sub>4</sub>, 137 mM NaCl and 2.7 mM KCl, all buffer solutions were prepared in deionized water. N-hydroxy succinimide (NHS) 98%, N-(3-dimethylaminopropyl)-N'-ethylcarbodiimide hydrochloride (EDC, Sigma Aldrich, Canada). Sulphuric acid, 96%, and hydrogen peroxide, 30%, were from Caledon Laboratories. Purified goat IgG and purified polyclonal rabbit anti-goat IgG (anti-goat IgG) were from MP Biomedicals, Canada. Deionized water was from a Millipore Milli-Q Plus purification system.

#### 4.2.2 *Substrate Preparation*

Glass (Dow Corning, Portsmouth, NH, 18 mm × 18 mm × 1 mm) substrates were pre-cleaned in piranha solution (1 : 3 H<sub>2</sub>O<sub>2</sub> : H<sub>2</sub>SO<sub>4</sub>) at 90°C for 15 min, rinsed several times with deionized water and dried with argon. A 15 nm adhesive layer of chromium and a 200 nm gold film were prepared by physical vapor deposition (PVP). A thermal evaporation system (Ion International Inc., New Windsor, NY) was used for the deposition of the gold and chromium films on the clean glass substrates. A vacuum of  $4.6 \times 10^{-6}$  mbar was maintained

during evaporation with rates of  $0.2^\circ\text{A}/\text{sec}$  for gold. Once prepared, the gold surfaces were rinsed using ethanol and water followed by drying with Argon. The substrates were then cleaned in ozone cleaner (UV0-Cleaner, Model No. 42, Jelight Company Inc., Irvine, CA) for 10 min prior to surface modification.

#### 4.2.3 Preparation of extrinsic Raman labels (ERLs) of GNRs

The  $-\text{SC}_{11}(\text{EO})_6\text{-COO}^-/\text{tNB}$  modified GNRs were prepared following the procedure in Chapter 2. The  $-\text{SC}_{11}(\text{EO})_6\text{-COO}^-/\text{tNB}$  modified GNRs were covalently linked with rabbit anti-goat IgG. This was accomplished by exposing the modified GNRs to an aqueous solution of equal volumes of 5 mM EDC and 5 mM NHS for 30 min to activate the carboxylic acid groups, the GNRs were centrifuged once at 8000 rpm for 10 min, and the pellets were re-suspended in 2 mM phosphate buffer, pH 7.4. Afterwards 20  $\mu\text{L}$  of 1 mg/mL purified rabbit anti-goat IgG antibody solution was added to the GNRs suspension and incubated for 2 h. Finally, the rabbit anti-goat IgG conjugated GNRs were separated from leftover reactants by centrifugation once at 8000 rpm for 10 min and re-suspending the antibody-conjugated gold nanorods in 2 mM phosphate buffer with pH 7. The modified GNRs are stable for at least one month, and stored at  $7^\circ\text{C}$  until use (Figure 4.01A).

#### 4.2.4 *Substrate modification*

Surface modification was achieved through self-assembly of  $-\text{SC}_{11}(\text{EO})_6\sim\text{COOH}$ . A planer gold-coated 0211 chip was immersed in 1 mM of  $\text{HSC}_{11}(\text{EO})_6\sim\text{COOH}$  prepared in ethanol for 2 h. The slides were removed from the solution and rinsed with ethanol to remove unbound thiols from the surface, and then dried with a stream of argon. Then, the capture agent (rabbit anti-goat IgG antibodies) was covalently linked to the  $-\text{SC}_{11}(\text{EO})_6\sim\text{COOH}$  modified substrate. This was achieved by exposing the  $-\text{SC}_{11}(\text{EO})_6\sim\text{COOH}$  modified planer gold substrate to an aqueous solution of 5 mM EDC and 5 mM NHS for 30 min to activate the carboxylic acid groups. Afterwards the surface was rinsed with deionized water and immediately exposed to 1 mg/mL rabbit anti-goat IgG antibodies for 2 h, followed by rinsing with PBS buffer. To block any unreacted succinimidyl ester sites the surface was exposed to 1% bovine serum albumin (BSA) in PBS buffer for 10 min and rinsed with PBS buffer. At this stage the biochip was ready to be exposed to varying concentrations of analyte (goat IgG) for 2 h followed by rinsing with 2 mM PBS buffer (Figure 4.01B).

The analyte (goat IgG) was labeled on the chip surface by incubating the substrate with 0.5 mL of 30 nM rabbit anti-goat IgG conjugated gold nanoparticles, and rabbit anti-goat IgG conjugated GNRs with 2.4 aspect ratio for 4 h followed by rinsing with 2 mM PBS buffer, deionized water and drying under a stream of nitrogen (Figure 4.01C).

#### 4.2.5 *Preparation of blank sample*

Blank solution contained 0 M goat IgG prepared in 0.1 M PBS buffer. After preparation of anti-goat IgG coated substrate, blocking any unreacted succinimidyl ester sites by 1% BSA for 10 min and rinsing with deionized water the substrate exposed to blank solution for 2 h. Afterwards the surface was briefly rinsed with deionized water. Lastly, the chip was incubated with SERS labels for 2 h followed by rinsing with deionized water and drying under a stream of argon.

#### 4.2.6 *Instrumentation*

High resolution transmission electron microscopy (HRTEM) measurements. HRTEM imaging was used firstly to examine the conjugation of antibodies to  $-\text{SC}_{11}(\text{EO})_6\sim\text{COO}^-/\text{tNB}$  modified GNRs through measuring the coating thickness of the GNRs. TEM grids (carbon coated copper grid) were prepared by drop casting 2  $\mu\text{L}$  of anti-goat IgG conjugated GNR solution on the TEM grids. The solution was wicked through the grid by touching the underside to filter paper and then allowed to air dry before analysis. This method was used

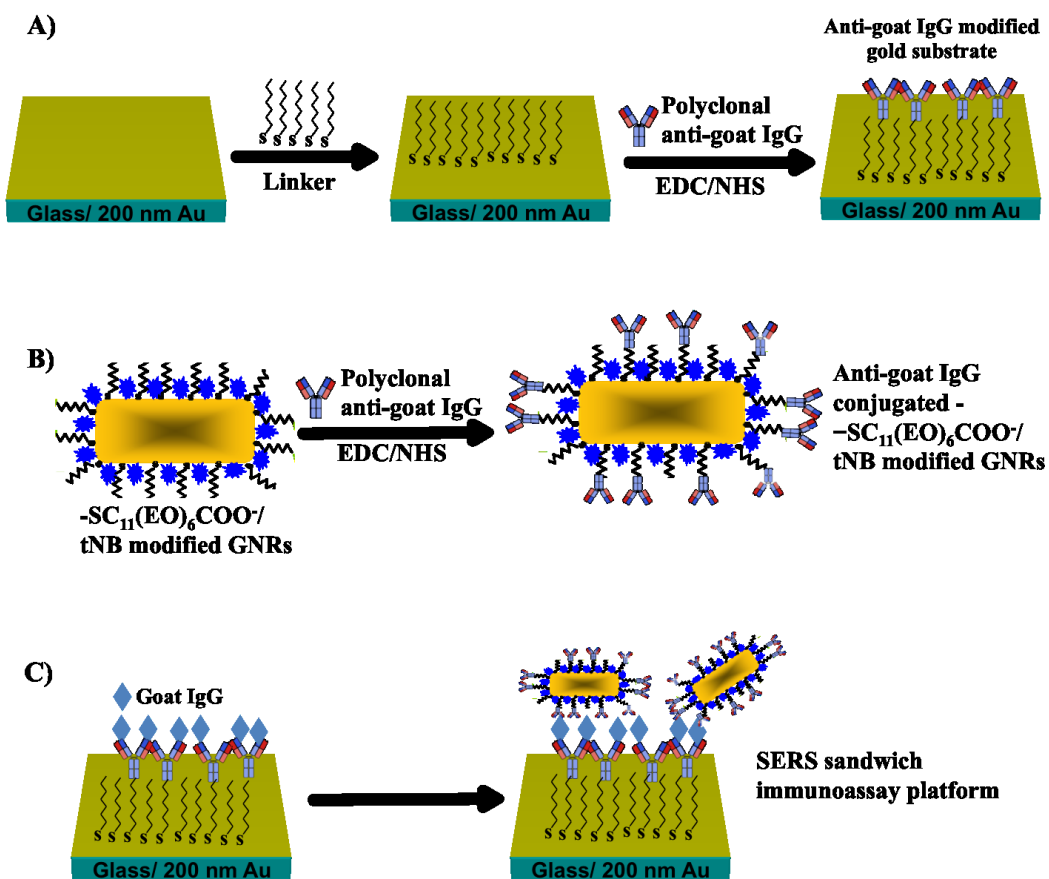


**Figure 4.01.** Schematic diagram illustrates A) preparation of anti-goat IgG modified planer gold substrate, B) conjugation of anti-goat IgG to  $-\text{SC}_{11}(\text{EO})_6\text{COO}^-/\text{tNB}$  modified GNRs and C) SERS sandwich immunoassay platform.

to avoid forming specific patterns on the grid surface due to water evaporation.<sup>159</sup>

These HRTEM images were obtained with a JEOL 2200FS TEM/STEM microscope with a 200 kV field emission gun and in-column energy filter (Omega Filter).

Extinction spectroscopy. Anti-goat IgG conjugated GNPs and GNRs were characterized with UV-vis spectroscopy to measure the surface plasmon band shift and intensity after modification. The extinction spectra were obtained using a Perkin-Elmer Lambda 35 UV/VIS/NIR spectrophotometer with a 10 mm optical path length.

Surface enhanced Raman scattering (SERS) measurements. SERS spectra were recorded with a Renishaw inVia Raman Microscope equipped with high performance near-IR (HPNIR) diode (785 nm, 1200I/mm) laser, and a CCD detector. Radiation of 785 nm from the air-cooled diode laser was used for excitation. Laser power at the sample was a  $5 \pm 0.5$  mW. The microscope was based on a Leica system. A 5 $\times$  microscope objective was used to first focus the laser beam and a 50X objective used to collect spectra. All reported spectra are the result of integration time of 10 seconds.

Scanning electron microscopy (SEM) measurements. SEM images were collected using a Hitachi S4800 Field Emission SEM system from Hitachi Scientific Equipment, Japan. Image acquisition was carried out with a 10 and / or 15 kV accelerating voltage and a 15  $\mu$ A emission current. The working distance was approximately 5-10 mm.

### 4.3 Results and discussion

As discussed above an illustration of the sandwich assay explored here is shown in Figure 4.01C. The two main requirements for the proposed chip based SERS sandwich immunoassay are conjugation of  $-\text{SC}_{11}(\text{EO})_6\sim\text{COO}^-/\text{tNB}$  modified GNRs with anti-goat IgG and immobilization of capture antibodies (anti-goat IgG) on a gold substrate. The analyte (goat IgG) will be sandwiched between the assay chip and the GNR label. As shown in Chapter 3, GNRs with larger aspect ratio provide higher SERS intensities with 780 nm excitation wavelength. Thus, GNRs with an aspect ratio of 2.4 were used here. The following discussion is divided into several sections that describe the conjugation of  $-\text{SC}_{11}(\text{EO})_6\sim\text{COO}^-/\text{tNB}$  modified GNRs with antibodies and an assessment of the designed SERS-based assay performance.

#### 4.3.1 *Characterization and monitoring of gold nanorods conjugated with anti-goat IgG*

HRTEM characterization for GNR coating thickness. Anti-goat conjugated GNRs were imaged with HRTEM to quantitatively measure the coating thickness before and after conjugation with the antibodies. In Chapter 2 we presented HRTEM images that enabled us to measure the thickness of the  $-\text{SC}_{11}(\text{EO})_6\sim\text{COO}^-$  monolayer on GNRs. This was determined to be  $2.2 \pm 0.6$  nm based on average of ten measurements. Figure 4.02A presents again Figure 2.03 B which is HRTEM image of a  $-\text{SC}_{11}(\text{EO})_6\sim\text{COO}^-$  coated GNR of aspect ratio

2.4. Figure 4.02B is an image after conjugation with anti-goat IgG antibodies. In these HRTEM images that the coating thickness is shown as a faint layer surrounding the dark GNR surface. These HRTEM images were used to measure the thickness of the anti-goat IgG layer surrounding the GNR (average of ten measurements), which was found to be  $5 \pm 1$  nm.

The size of immunoglobulin G of various species, such as rabbit anti-goat IgG has been reported to be  $\sim 8-10$  nm.<sup>264</sup> Variation among the size of antibodies of various species is due to differences in their molecular weight. Note that in our images (Figure 4.02B) the structure of the antibodies is not directly observed. It is difficult to directly observe biological molecules such as antibodies with HRTEM because they are usually composed of light elements include H, C, N, and O. The Coulomb potential for the electron beam is small and the contrast of TEM images becomes weak. Using an electron microscope dye, Kamogawa and co-workers recently used HRTEM to measure the length of Fab region for IgG antibody to be 2.5 nm; the length of Fc region was at least 3.1 nm and the width of Fc and Fab varied from  $\sim 1.2$  to 2.5 nm.<sup>265</sup> In addition, it is expected that the drying of biological molecules such as antibodies would be accompanied by a noticeable decrease in size. Considering the above we feel that the change in thickness observed upon conjugation of anti-goat IgG to the  $-\text{SC}_{11}(\text{EO})_6\sim\text{COO}^-$  modified GNRs ( $2.2 \pm 0.6$  nm to  $5 \pm 1$  nm) provides compelling evidence that the conjugation reaction was successful.

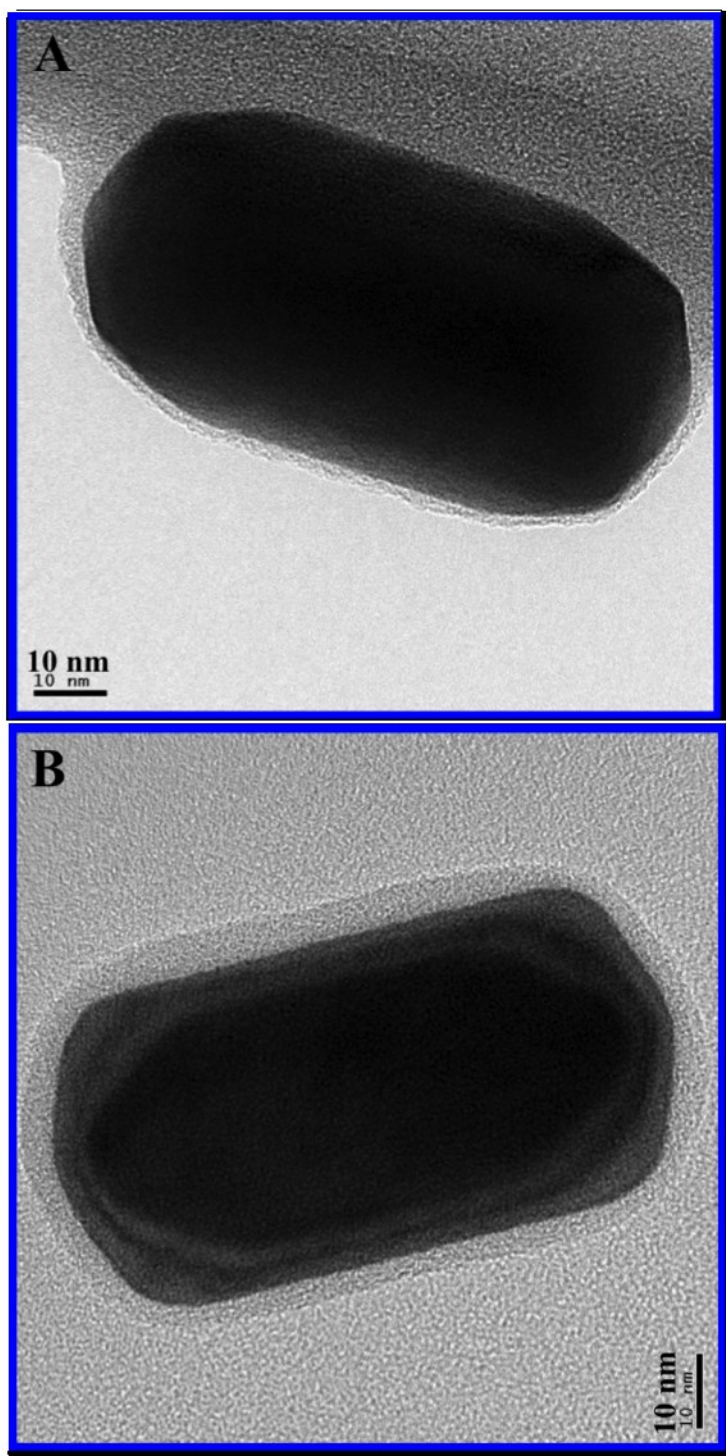


**Figure 4.02.** HRTEM images show (A)  $-\text{SC}_{11}(\text{EO})_6-\text{COO}^-$  coated GNRs of aspect ratio (l/d) 2.4, and (B) anti-goat IgG conjugated GNRs.

Extinction spectroscopy measurements. Extinction spectroscopic results provides further evidence for successful conjugations of anti-goat IgG to the GNRs and are diagnostic of the colloidal stability of the particles. Figure 4.03 contains the extinction spectra of  $-\text{SC}_{11}(\text{EO})_6\sim\text{COO}^-/\text{tNB}$  coated and anti-goat conjugated GNRs of aspect ratio 2.4. The  $-\text{SC}_{11}(\text{EO})_6\sim\text{COO}^-/\text{tNB}$  coated rods exhibit a transverse plasmon band at 529 nm and a longitudinal band at 648 nm. These same bands are observed at 533 nm and 654 nm, respectively, for the anti-goat IgG conjugated GNRs. The red-shift in the LSPR bands indicate a variation in the effective reflective index of the surrounding molecular layer following conjugation of the antibody.<sup>151</sup> These results are in agreement with the HRTEM images presented in Figure 4.02. The spectra in Figure 4.03 also provide no indication of GNR aggregation, as no significant broadening of the plasmon bands is observed. We have found that anti-goat IgG conjugated GNRs are stable in solution for at least one month at 7 °C.

Sandwich immunoassay featuring GNR ERLs. Herein, we demonstrate the capability of anti-goat IgG conjugated GNRs for the detection of goat IgG in a sandwich immunoassay as shown in Figure 4.01. GNRs of aspect ratio 2.4 were used for various concentrations of goat IgG ranging from 1 pM to 1 nM. The SERS spectra of tNB corresponding to six-different goat IgG concentration and a blank are displayed in Figure 4.04A. The non-specific adsorption involved in this assay platform was evaluated by exposing the capture layer to a blank

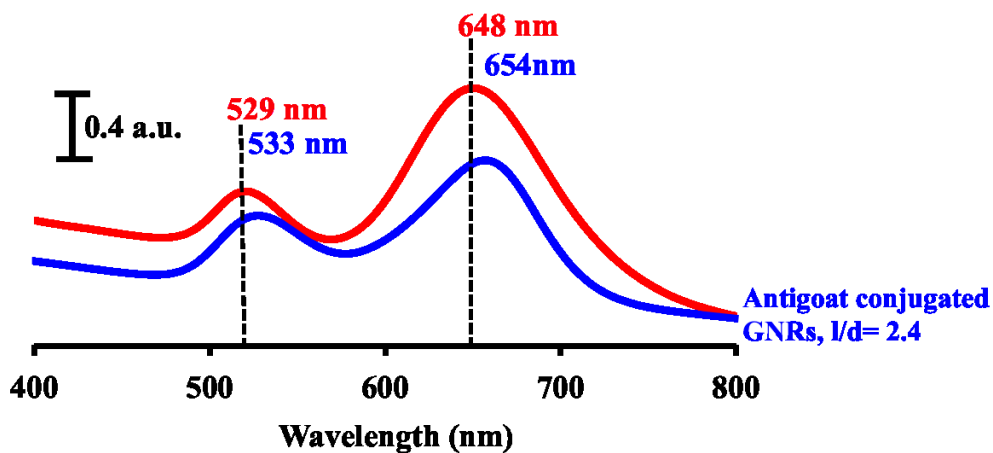


**Figure 4.03.** The extinction spectra of  $-\text{SC}_{11}(\text{EO})_6\sim\text{COO}^-/\text{tNB}$  coated GNRs and anti-goat conjugated GNRs of aspect ratio 2.4, the spectra were offset for clarity.

sample, which containing 0 nM of goat IgG. An expanded view of the blank spectrum is shown in Figure 4.04B. The low signal observed is indicative of a very low amount of nonspecific adsorption of the GNRs to the substrate.

As discussed below, the signal of the blank, and thus the non-specific adsorption is very important in determining the limit of detection (LOD).<sup>104</sup> Non-specific adsorption was examined further by SEM imaging. Figure 4.05 present two SEM images at two-different magnifications for SERS assay chip used for detection of 1 nM goat IgG. These SEM images were collected to show the blank area next to the analyte-exposed area on the same chip. This has been achieved by using polydimethylsiloxane (PDMS) stamps to pattern the gold substrate surface.<sup>266</sup> In our sandwich immunoassay design, we used  $-\text{SC}_{11}(\text{EO})_6\sim\text{COOH}$  molecules to form a SAM monolayer on the surface of a planar gold substrate. The choice of  $-\text{SC}_{11}(\text{EO})_6\sim\text{COOH}$  is due to presence of ethoxy groups that minimize hydrophobic interaction of protein with gold surface and reduces the nonspecific adsorption. Previously, ethylene glycol molecules have been widely studied and used to reduce nonspecific adsorption of biological molecules.<sup>267-269</sup> In addition, the remaining active sites on the functional SAM were blocked with 1% BSA. The BSA step aims at blocking fraction of the surface that are not covered with anti-goat IgG to prevent nonspecific binding. Figure 4.05 clearly shows that the blank areas contain very few bound GNRs.

The spectra in Figure 4.04A were used to generate a calibration curve for goat IgG. The binding of the GNRs to the assay surface can be quantitated by

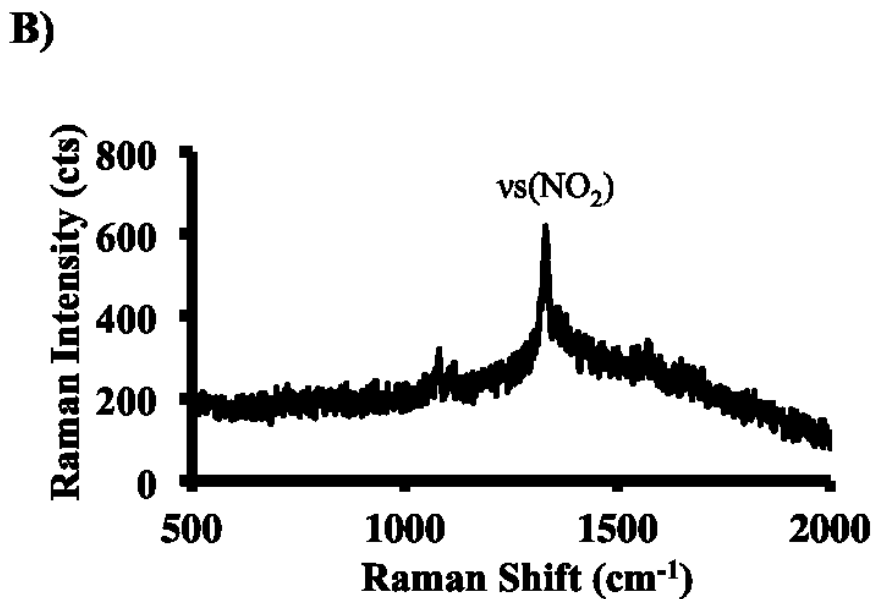
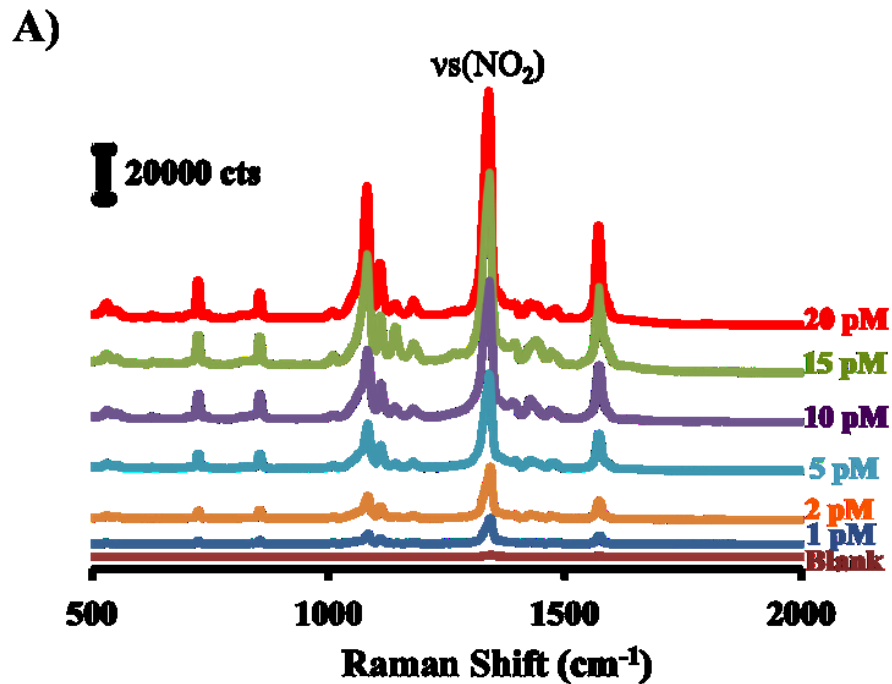


**Figure 4.04.** SERS spectra for tNB were collected from bioassay chips used for: A) detection of different concentration of goat IgG 1, 2, 5, 10, 15, 20 pM, and blank. The SERS spectra were offset for clarity; B) A magnified SERS spectrum of blank.

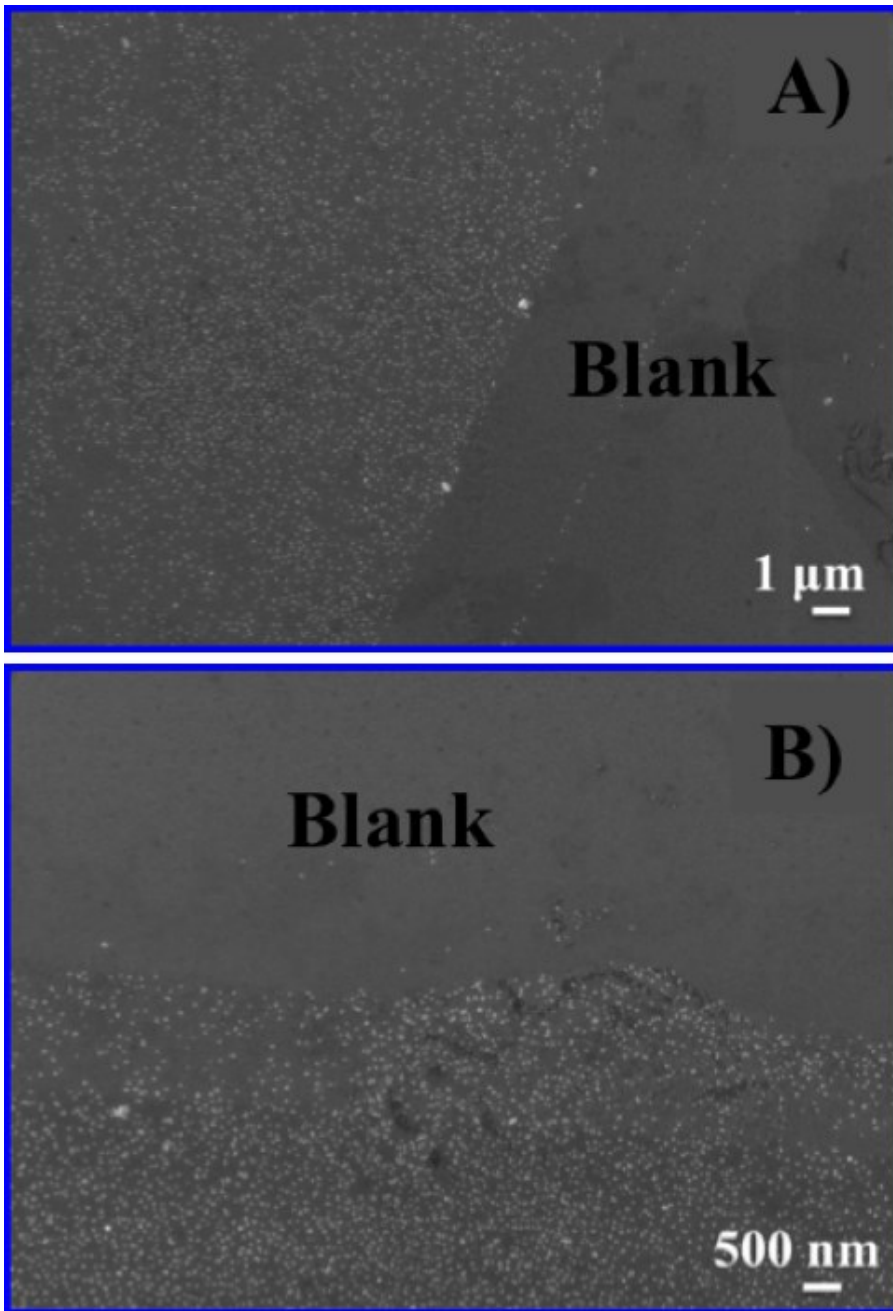


**Figure 4.05.** SEM images show anti-goat IgG conjugated GNRs of aspect ratio 2.4 used in SERS-based sandwich immunoassay for detection of 1 nM goat IgG at two-different magnifications A) 1  $\mu\text{m}$  and (B) 500 nm. Bovine serum albumin was used as blocking agent.

using the intensity of the Raman band of the symmetric stretch of the nitro group of tNB at  $\sim 1337\text{ cm}^{-1}$ . As can be observed in Figure 4.04A this band clearly scales with the goat IgG concentration. In agreement with previous reports using antibody-conjugated GNRs in SERS-based immunoassays,<sup>104, 245</sup> there are no observable Raman active vibrations associated with the antibody conjugated onto the GNR surface via the  $-\text{SC}_{11}(\text{EO})_6-\text{COOH}$  linker. This is likely due to the strong dependence of the SERS intensity on the distance from the GNR surface.<sup>98</sup>

A plot of SERS response at various goat IgG concentrations is shown in Figure 4.06 A. The SERS intensity at  $1337\text{ cm}^{-1}$  increases as the goat IgG concentration increases until the surface has been saturated with goat IgG resulting in the response to level off. The maximum concentration analyzed was 1 nM and produces a similar response to that for 100 pM, indicating that saturation coverage has already been reached at 100 pM. We observe a linear relationship ( $R^2= 0.988$ ) for a concentration range of 1-20 pM (Figure 4.06 B). This establishes the linear dynamic range of our sandwich immunoassay from 1 pM to approximately 100 pM or 2 orders of magnitude, which is common for surface based bioassays.

Figure 4.04 and 4.06 allow the determination of the limit of detection (LOD). In these types of surface bioassays the LOD is governed by the amount nonspecific adsorption.<sup>104, 140, 270</sup> For this

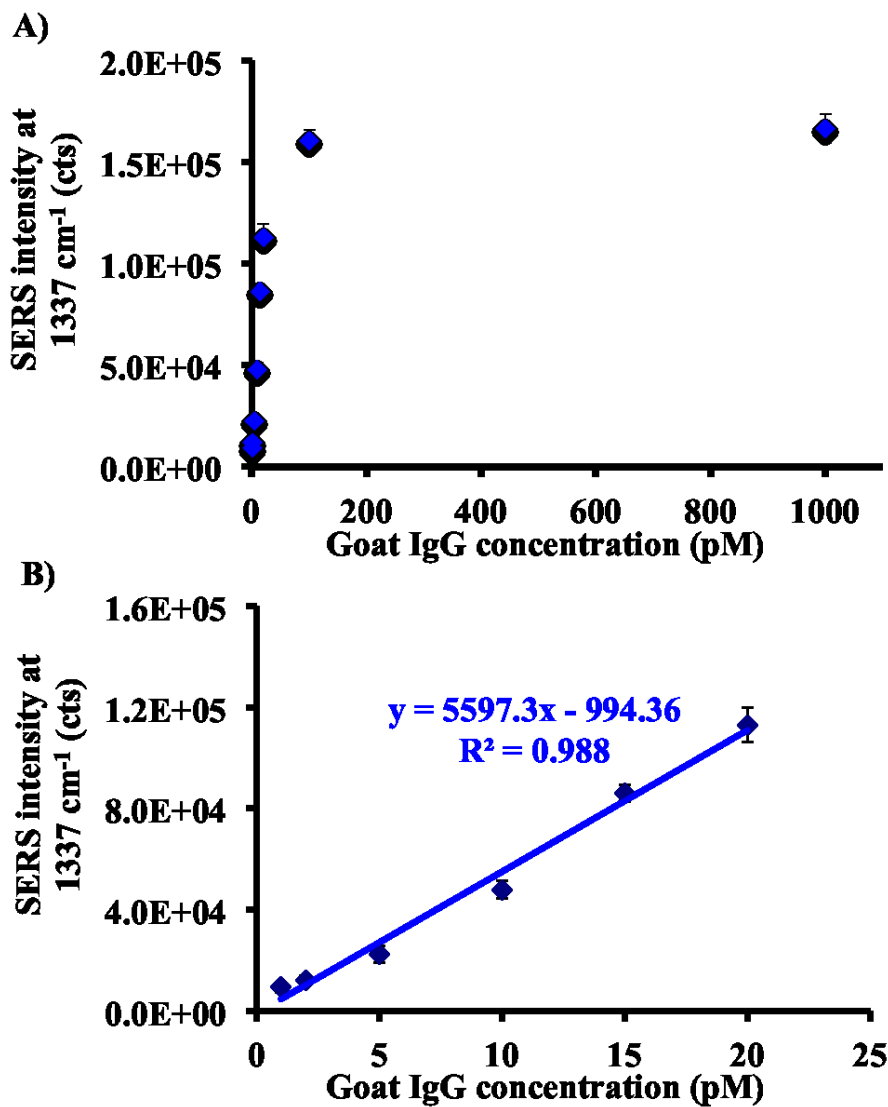


**Figure 4.06.** A) Plot of SERS intensity of the symmetric stretch of the nitro group at  $1337\text{ cm}^{-1}$  versus goat IgG concentration (1 pM to 1 nM) shows linear dynamic range from 1- 20 pM. The error bars represent the standard deviation of the mean for 5 different spots analyzed on each biochip of 2 separate bioassays. B) Plot of SERS intensity at  $1337\text{ cm}^{-1}$  versus goat IgG concentration from 1 to 20 pM.

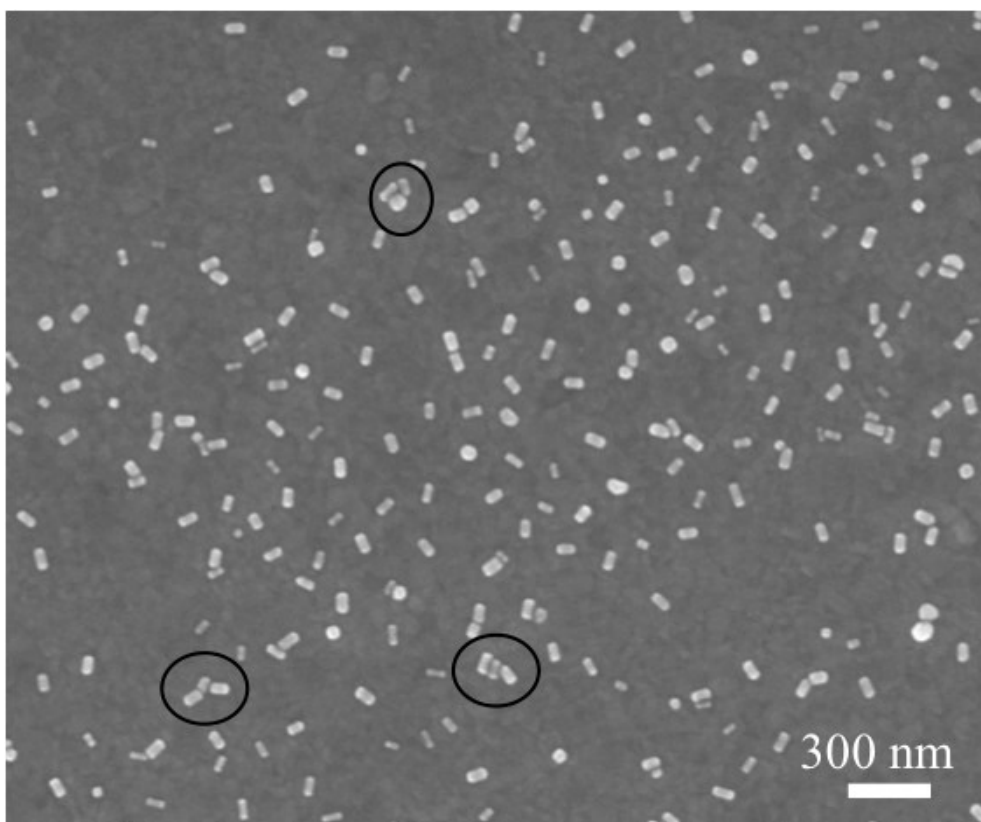
reason, the signal of blank substrate shown in Figure 4.04B is used. The limit of detection is defined as (blank signal +  $3\sigma_{\text{Blank}}$ ), where  $\sigma_{\text{Blank}}$  is the standard deviation of blank. Using this calculation LOD is 15 fM. This value of the LOD is lower than that of a SERS assay utilizing spherical gold nanoparticles (10 pM)<sup>271</sup> and for surface plasmon resonance based immunoassay (77 pM).<sup>272</sup> This highlights the enhanced detection afforded by the use of GNR as ERLs.

#### *4.3.2 Further characterization of anti-goat IgG conjugated GNRs performance in SERS-based sandwich immunoassay by scanning electron microscopy (SEM)*

In this chapter, we focus on a SERS-based biosensing application that is enhanced by the shape<sup>273</sup> of the gold nanorods and not by aggregation. Strong near-field coupling between LSPR of closely packed metal nanoparticles results in a dramatic electric field enhancement in nanoscale volume.<sup>274</sup> The enhanced electric field influences the reproducibility of the Raman signal.<sup>90</sup> This is because the electric field intensity values are difficult to control due to random assemblies of these aggregates with a huge variation in their size and shape. The challenge facing the reproducibility of Raman signal collected from SERS assay chip relies on an averaging of the Raman signal over a relatively large area. In general, SERS-based assays require nanoparticle metal surface that combine high electric field enhancement with low on-chip and chip-to-chip variability.

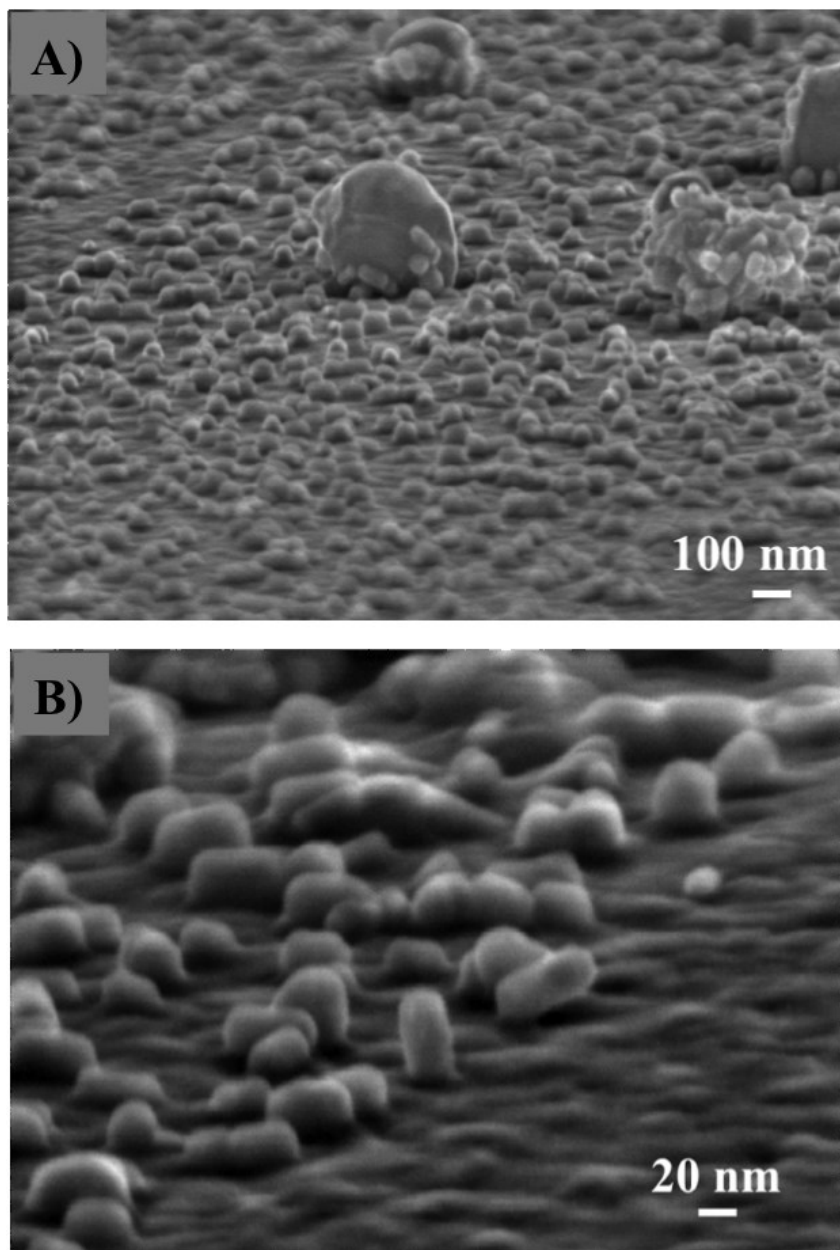
In Chapter 2 and 3 we utilized SEM imaging to examine colloidal stability of GNRs after exchange of the CTAB coating with  $-\text{SC}_{11}(\text{EO})_6\sim\text{COO}^-$  /tNB. Herein, SEM images provide evidence for the absence of large-scale aggregation of anti-goat IgG conjugated GNRs on the surface of SERS assay chip. Figure 4.07 presents a SEM image shows the distribution of the GNRs of aspect ratio 2.4 utilized in a sandwich immunoassay for detection of 100 pM of goat IgG. Figure 4.07 clearly shows the absence of large-scale aggregation. The GNRs are generally well-distributed with a few clusters present throughout. Some clusters are circled in Figure 4.07. A possible explanation for these clusters is evaporation of the solvent following incubation. These SEM observations are consistent with good SERS reproducibility results that we collected from SERS assay chips as shown in Figures 4.04 and 4.06.

Figure 4.08 A and B shows side view SEM images of SERS assay chip and anti-goat IgG conjugated GNRs of aspect ratio 2.4 were used for detection of 1 nM of goat IgG at two-different magnifications. The large spherical structure in Figure 4.08A are unidentified and may be dust particles or salt crystals. These SEM images show different orientations for anti-goat conjugated GNRs on the biochip upon binding to the analyte (goat IgG) for example vertical, angled and mainly flat bindings. This can be due to the rods binding at the (111) end in a vertical manner. From these images we concluded that some spheres that appeared in top



**Figure 4.07.** SEM image shows anti-goat IgG conjugated GNRs of aspect ratio 2.4 used in SERS-based sandwich immunoassay for detection of 100 pM goat IgG. The circles highlight clusters of GNRs that are discussed in the text.

views of SEM images shown in Figure 4.07 could be top view of vertically bounded GNR. In addition, the image in Figure 4.08 B provides strong evidence that the conjugated antibodies are distributed evenly over the GNR surface. That is, the antibodies are immobilized on the sides and ends of the GNRs by extension. This implies that the two components of our mixed monolayer are evenly distributed over the GNR surface.



**Figure 4.08.** Side view SEM images of anti-goat IgG conjugated GNRs of aspect ratio 2.4 used in SERS-based sandwich immunoassay for detection of 1 nM goat IgG at two different magnification scales A) 100 nm and B) 20 nm.

#### 4.4 Conclusions

High resolution transmittance electron microscopy (HRTEM) and extinction spectroscopy provide a clear evidence of successful conjugation of  $\text{-SC}_{11}(\text{EO})_6\text{-COO}^-/\text{tNB}$  modified GNRs with anti-goat IgG antibodies as extrinsic Raman labels (ERLs) in SERS-based assays. The SERS intensity dependence on the goat IgG concentration was assessed by a chip based SERS sandwich immunoassay using GNRs of aspect ratio 2.4. The calculated limit of detection of goat IgG was 15 fM, which is lower than other commonly used immunoassay detection methods such as surface plasmon resonance<sup>272</sup> and surface enhancement Raman scattering utilizing spherical gold nanoparticles.<sup>271</sup> The performance of the anti-goat IgG conjugated GNRs in the SERS-based immunoassay has been demonstrated by Raman microscopy as well as scanning electron microscopy (SEM) that evidenced absence of large-scale aggregation on the surface of SERS assay chip. Lastly, with the design of ERLs of gold nanorods with good colloidal stability and tested femto-molar limit of detection, these ERLs will provide the capability to detect small molecules such as metabolites. This will be discussed in Chapter 5.

## 5 Chapter V

---

### **An indirect competitive SERS-based assay for detection of free thyroxine using gold nanorods as SERS labels**

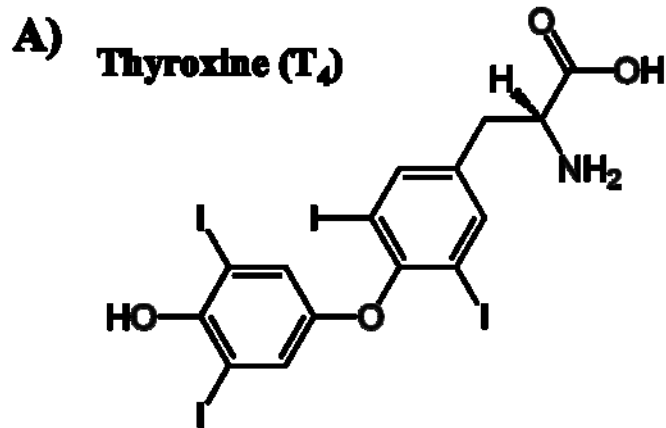
#### **5.1 Introduction**

The work presented here will build from the previous projects and focus on biosensing of the small molecule metabolite, free thyroxine ( $\text{fT}_4$ ). In Chapter 2 and 3 the modification of CTAB capped gold nanorods (GNRs) of different-aspect ratios to extrinsic Raman labels (ERLs) with good colloidal stability and anchor points for functionalization with biological probe was discussed. Here, the use of this chemistry to conjugate  $\text{fT}_4$  to GNRs is described. Further, Chapter 4 demonstrated that these ERLs of GNRs could be successfully utilized in a SERS-based sandwich assay for immunoglobulin G detection with a femto-molar limit of detection. The experience gained from the earlier work will be utilized to introduce an indirect competitive design that detects and quantifies  $\text{fT}_4$  in human plasma.

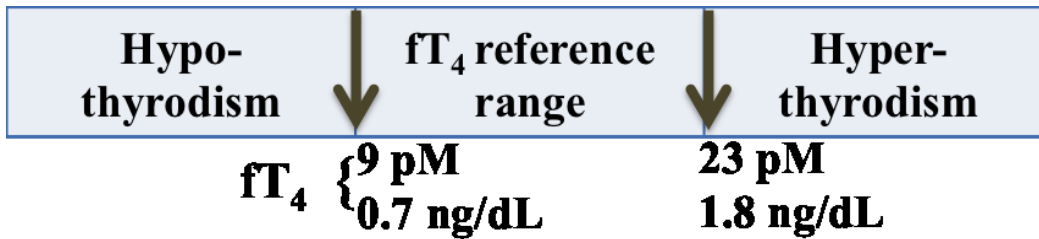
Recent reports show more than 300 million people suffer from thyroid disease. In general, the concentration of hormones secreted by the thyroid gland is proportional to reflect the thyroid function of the patient. Determination of these hormones, can aid in the establishment of therapy for thyroid disease.

Figure 5.01A shows the chemical structure of thyroxine (3, 5, 3', 5'-tetraiodothyronine, T<sub>4</sub>), with molecular weight of 777 Da, T<sub>4</sub> is the most commonly measured thyroid hormone for diagnosis of thyroid function. T<sub>4</sub> are present in blood in both free and bound forms. More than 99.97 % of the T<sub>4</sub> in blood is bound to carrier proteins, among which 60 % is to thyroxine binding globulin (TBG), 30 % to thyroid binding prealbumin (TBPA), and 9.97 % binding to albumin (Alb) with a total concentration in human serum of ~65-155 nM. Only 0.03 % of T<sub>4</sub> with a concentration of 10-30 pM exists as free thyroxine (fT<sub>4</sub>).<sup>275-277</sup> The fT<sub>4</sub> is of interest to clinicians since it is believed to represent the biological activity that permeates cell membranes or interacts with receptors.<sup>278,</sup>  
<sup>279</sup> Thyroid function was assessed through the measurement of fT<sub>4</sub> level related to a reference range of 9-23 pM (Figure 5.01B). Increased levels of fT<sub>4</sub> are found in hyperthyroidism due to Graves' disease and Plummer's disease.<sup>280</sup> Low levels of fT<sub>4</sub> are associated with congenital hypothyroidism, myxedema, Hashimoto's disease, and some genetic abnormalities.<sup>279, 280</sup> Also fT<sub>4</sub> is necessary for normal neural development and normal cellular metabolism.<sup>279, 280</sup> For example, children born with thyroid hormone deficiency will not grow well and brain development can be severely impaired.

At present, the number of patients that suffer from thyroid diseases is increasing. A convenient and sensitive assay kit for thyroid hormones, especially



**B)**



**Figure 5.01.** A) The chemical structure for thyroxine (T<sub>4</sub>) hormone and B) changes in free thyroxine (fT<sub>4</sub>) normal range during hypo or hyper thyroid disorder.

fT<sub>4</sub>, is strongly desired. The methods proposed up to now for the determination of T<sub>4</sub> in its free and/ or bound form are HPLC,<sup>281</sup> radioimmunoassay (RIA),<sup>282, 283</sup> fluorescence immunoassay,<sup>284</sup> electrochemiluminescence,<sup>285, 286</sup> mass spectrometry,<sup>287</sup> various enzyme immunoassay,<sup>288-292</sup> and amperometry.<sup>293, 294</sup>

There are several problems to overcome for a simple, sensitive, and reliable assay for fT<sub>4</sub> detection. For example, electrochemical method requires preparation of working electrodes and multiple-step preparation. RIA tests now face increased concerns posed by waste disposal issues with radiolabeled analogue of the target analyte.

This chapter examines the use of surface enhanced Raman scattering (SERS) as the basis for a new test for fT<sub>4</sub>. Past work on the development of diagnostic tests with SERS has focused on the detection of peptides, proteins, viruses, and microorganisms.<sup>91, 140, 142, 203, 244, 295-298</sup> These targets, however, are much larger than fT<sub>4</sub> and have multiple recognition sites and are, as a result, well suited for use in sandwich-type assays. Although sandwich assay exhibits specificity and sensitivity, small molecules such as metabolites including fT<sub>4</sub> are not suitable for the conventional sandwich assay because of the lack of two discrete binding sites. For that, fT<sub>4</sub> is not a candidate for detection using sandwich assays because of its small size; thus a different scheme is necessary. While the direct detection of small molecules when adsorbed onto a SERS substrate has been previously reported,<sup>299-305</sup> much of this work has relied on the use of a chromatographic preparation technique such as HPLC<sup>303, 306</sup> and

capillary electrophoresis<sup>299</sup>. Furthermore, the inherently weak Raman signal of analytes such as  $\text{fT}_4$  complicates the detection at low concentrations even when adsorbed on SERS substrates.

We have employed SERS-based sandwich assay in Chapter 4 utilizing antibody-conjugated GNRs in a femto-molar limit of detection of goat IgG. The advantage of this strategy largely reflects three unique features of SERS.<sup>307-309</sup> First, the widths of Raman spectral bands are 10-100 times narrower than those of fluorescence, minimizing spectral overlap. Thus facilitating the detection of different ERLs at a single chip in multiplexed assays.<sup>271, 310</sup> Second, SERS intensities for Raman reporter molecules can rival those of fluorescent dyes, which enabled the detection of a single SERS label of GNR.<sup>311, 312</sup> Third, only one excitation wavelength is needed to produce SERS from different SERS labels, which simplifies the instrumental hardware required for signal generation and acquisition. This work herein studies the strategy of combining ERLs of GNRs in an indirect competitive assay to measure  $\text{fT}_4$ . The results are compared with conventional ELISA. The additional advantages of SERS assay over ELISA include eliminating the need for measuring the sample signal (absorbance) within limited time after stopping the reaction due to fading of the color. Also it is time saving because of fewer washing steps are required. Preparation of ERLs of GNRs has been achieved following the proposed scheme discussed in Chapter 2.

## 5.2 Experimental

### 5.2.1 Surface enhanced Raman scattering (SERS) study

Reagent and Materials. Cetyltrimethylammonium bromide (CTAB) capped GNRs were from NanoPartz, Loveland CO, which contained  $1 \times 10^{11}$  GNRs per 1 mL with  $60 \pm 5$  nm length,  $25 \pm 5$  nm width and aspect ratio of 2.4. 2-(2-{2-[2-(2-[2-(11-mercapto-undecyloxy)-ethoxy]-ethoxy)-ethoxy]-ethoxy}-ethoxy)-ethoxyamine hydrochloride ( $\text{HSC}_{11}(\text{EO})_6\text{-NH}_2$  HCl, MW= 526.73 g/mol) was obtained from ProChimia, Poland. A solution of 40 mM  $\text{HSC}_{11}(\text{EO})_6\text{-NH}_2$  HCl was prepared in deionized water. 4-nitrobenzenethiol (98%) was from Sigma Aldrich; Canada. 4 mM 4-nitrobenzenethiol (tNB) solution was freshly prepared in 20% of anhydrous ethanol (Quantum Chemical, Victoria, Australia) and 80% deionized water. Six- $\text{fT}_4$  standards spiked in human plasma from the ELISA kit were used in the indirect competitive SERS assay to construct the SERS calibration curve. These  $\text{fT}_4$  calibrators were chosen to evaluate assay applicability with true biological samples. Purified thyroxine ( $\text{fT}_4$ ) monoclonal antibody was from MyBioSource Inc. San Diego, U.S.A.  $\text{T}_4$  monoclonal antibody was specific to  $\text{fT}_4$  and  $\text{T}_4$ -BSA conjugate and it was prepared in 0.15 M sodium chloride, 10 mM Tris, pH 7.5. Phosphate buffered saline (PBS, pH 7.4) was prepared with reagent grade 1.4 mM  $\text{KH}_2\text{PO}_4$  and 4.3 mM  $\text{Na}_2\text{PO}_4$ , 137 mM NaCl and 2.7 mM KCl. All buffer solutions were prepared in deionized water. N-hydroxy succinimide (NHS) 98%, N-(3-dimethylaminopropyl)-N'-ethylcarbodiimide hydrochloride (EDC, Sigma

Aldrich). Deionized water was from with a Millipore Milli-Q Plus purification system.

Preparation of fT<sub>4</sub>-conjugated GNRs. The fT<sub>4</sub>-conjugated GNRs were prepared following the procedure outlined in Figure 2.01. Briefly, CTAB capped GNR solutions were purified from excess CTAB molecules in solution by centrifugation once at 8000 rpm, 25 °C for 10 min. The pellets of GNRs were dispersed in 1 mL of 40 mM HSC<sub>11</sub>(EO)<sub>6</sub>~NH<sub>2</sub>, sonicated for 1 min and then allowed to stand for 24 h at room temperature with intermittent gentle shaking. After 24 h, GNRs were sonicated for 1 min and centrifuged once at 8000 rpm for 10 min then the supernatant of excess HSC<sub>11</sub>(EO)<sub>6</sub>~NH<sub>2</sub> were removed. The -SC<sub>11</sub>(EO)<sub>6</sub>~NH<sub>2</sub> modified pellets of GNRs resuspended in 1 mL of 4 mM tNB. After that GNRs suspension was sonicated for 1 min and allowed to stand for 24 h at room temperature with intermittent gentle shaking. After 24 h, GNRs were sonicated for 1 min and centrifuged once at 8000 rpm for 10 min then the supernatant of excess tNB was removed by centrifugation once at 8000 rpm for 10 min and the pellets were suspended to 1 mL in deionized water. A 200 µL of 8 ng/dL fT<sub>4</sub> was added to a mixture of 5 mM NHS/5mM EDC in phosphate buffer, pH 7.5. After 1 h, the activated ester of fT<sub>4</sub> was added to -SC<sub>11</sub>(EO)<sub>6</sub>~NH<sub>2</sub>/tNB modified GNR solution and allowed to stand for 2 h. Then the GNR solution was centrifuged once at 8000 rpm for 10 min to remove excess reagents. The fT<sub>4</sub>-conjugated GNR pellets were resuspended in 1 mL of phosphate buffer, pH 7.5 and stored at 4 °C until use (Figure 5.02).

Preparation of gold substrate. The 4-inch Si/SiO<sub>2</sub> sample wafers (thermal SiO<sub>2</sub> thickness was 200-300 nm) were cleaned with piranha solution (3:1 H<sub>2</sub>SO<sub>4</sub>/H<sub>2</sub>O<sub>2</sub>) for 30 minutes. Then wafers were transferred to a Johnson Ultravac electron-beam evaporator where 5 nm of Cr adhesion layer and 200 nm of Au were deposited under vacuum (deposition rate 3 Å/s, vacuum pressure 2.4 x 10<sup>-7</sup> torr). The wafers were diced into pieces of 0.5 inch × 0.5 inch after being coated with photoresist to protect wafer surface from scratches. The wafers were sonicated in acetone, isopropanol and water 10 minutes each to remove the photoresist and clean them. The substrates were then cleaned in an ozone cleaner (UVO-Cleaner, Model No. 42, Jelight Company Inc., Irvine, CA) for 10 min prior to surface modification.

*Warning: Piranha solution should be handled with extreme care; it will react violently with organic materials, presenting an explosion danger.*

Modification of gold substrate. Modification of the substrate surface was achieved through self-assembly of -SC<sub>11</sub>(EO)<sub>6</sub>-COOH. Typically, a planar gold-coated chip was immersed overnight in 10 mM ethanolic solution of HSC<sub>11</sub>(EO)<sub>6</sub>-COOH. The slide was rinsed well with ethanol to remove unbound thiols, and dried with a stream of argon. Then, the chip was immersed in a mixture solution 1 : 1 mixture of 5 mM NHS/5 mM EDC prepared in phosphate buffer pH 7.5, and allowed to react for 1 h. The slide was removed from solution and rinsed well with ethanol to remove excess reagents. The slide was incubated with 1 mg/mL T<sub>4</sub>-monoclonal antibody for 2 h. To block any unreacted

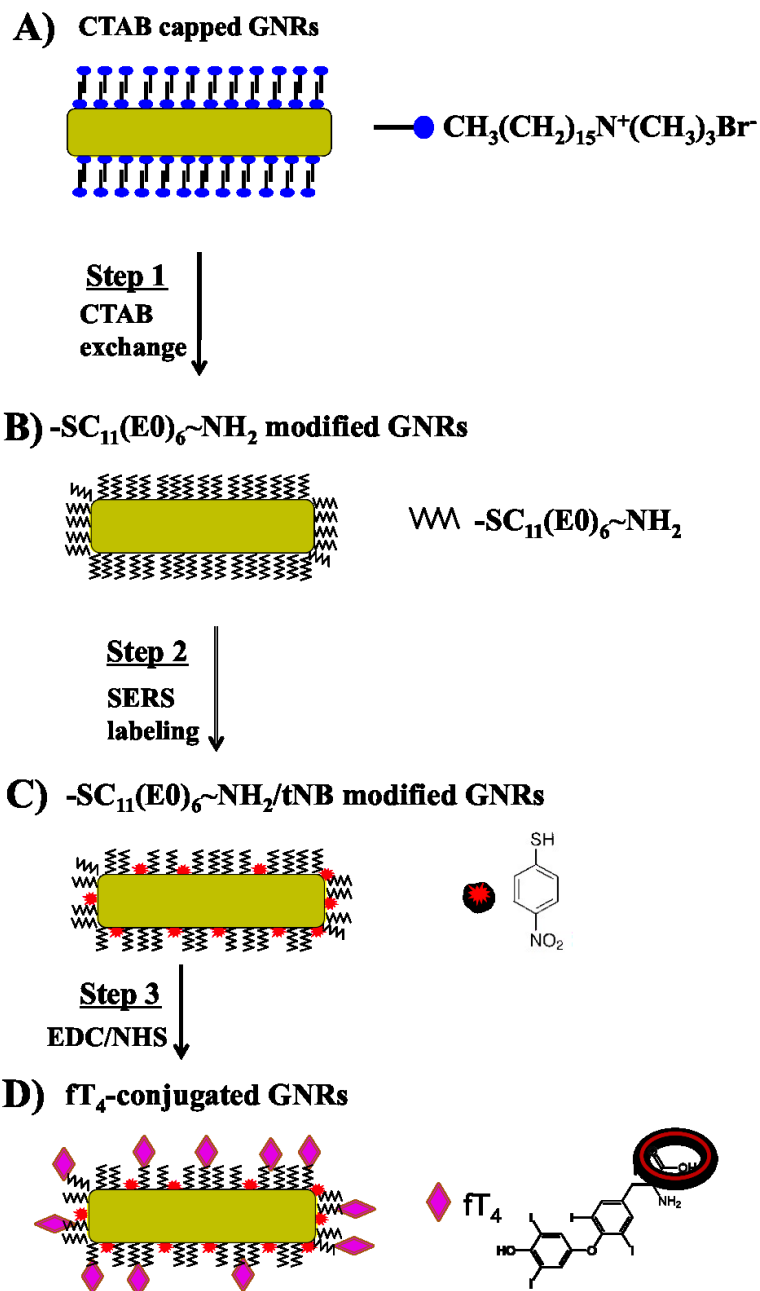


**Figure 5.02.** Schematic illustration shows preparation of  $\text{fT}_4$ -conjugated GNR. A) CTAB capped GNRs, B) modifying CTAB capped GNRs with  $-\text{SC}_{11}(\text{EO})_6\sim\text{NH}_2$ , C) incorporation of tNB in a mixed thiolate layer, and D)  $\text{fT}_4$  are conjugated into GNRs via EDC/NHS chemistry.

succinidyl ester sites the surface was exposed to SuperBlock blocking buffer for 1 h and then rinsed with PBS buffer and deionized water. Figure 5.03 shows SERS-based assay chip was exposed to  $fT_4$  calibrators and  $fT_4$ -conjugated GNRs for 2 h, followed by rinsing with PBS buffer, deionized water and drying under a stream of argon.

### 5.2.2 *Enzyme-linked immunosorbent assay (ELISA) study*

We purchased a solid phase competitive ELISA kit for  $fT_4$  from MyBioSource, Inc. San Diego, USA. The ELISA kit contained microwells coated with  $fT_4$  monoclonal antibody,  $fT_4$  horseradish peroxidase (HRP) enzyme conjugate, 3, 3', 5, 5'-tetramethylbenzidine (TMB) substrate, stop solution (sulfuric acid), wash concentrate and six  $fT_4$  standard solutions prepared in human serum of values: 0, 0.45, 0.94, 2.10, 3.70 and 8.20 ng/dL. 50  $\mu$ L of  $fT_4$  standard solution and control were pipetted into microwells coated with  $fT_4$  monoclonal antibody to be assayed in duplicate. TMB is a soluble colorimetric substrate for HRP enzyme and provided as a ready-to-use solution. In the presence of HRP, the TMB and peroxide contained in the substrate solution react

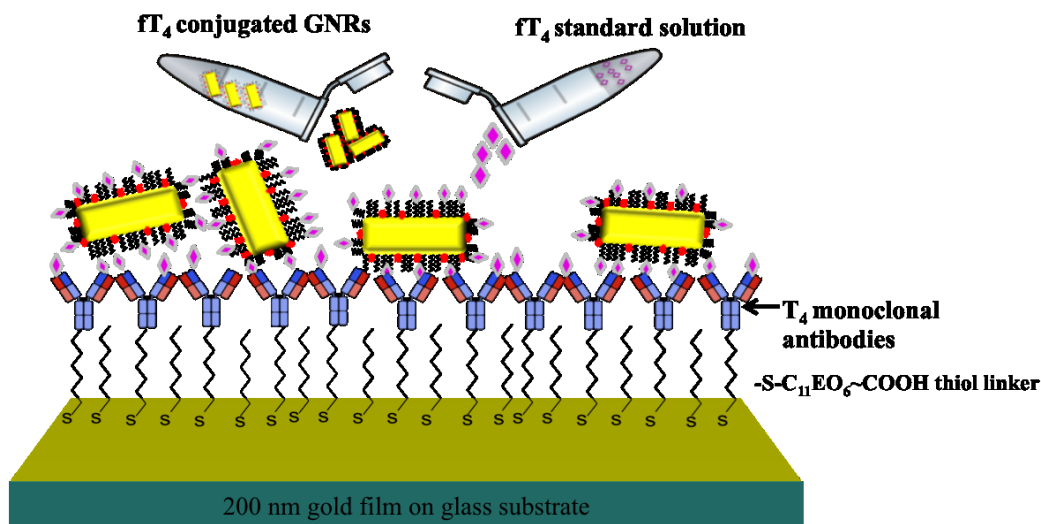


**Figure 5.03.** Schematic diagram shows SERS-based assay platform. Planar gold substrate was modified with a SAM of  $-SC_{11}(EO)_6-COOH$  linked with the amino group of  $T_4$ -monoclonal antibody via NHS/EDC chemistry and  $fT_4$ -conjugated GNRs compete with  $fT_4$  standard solution for  $T_4$ -monoclonal antibody binding sites. The diagram is not drawn to scale.

to produce a blue color. The color intensity is proportional to the amount of HRP activity, which in turn is related to the levels of target analyte. Addition of sulfuric acid stop solution changes the color to yellow, enabling accurate measurement of the intensity at 450 nm using a spectrophotometer or plate reader. Figure 5.04. shows ELISA indirect competitive assay platform. A 100  $\mu\text{L}$  of  $\text{fT}_4$  enzyme conjugate was added to all wells and incubated for 60 min at room temperature 26  $^{\circ}\text{C}$ . Liquid from all wells was removed; unbound  $\text{fT}_4$  and  $\text{T}_4$ -enzyme conjugate were washed off by filling the wells with 300  $\mu\text{L}$  of wash buffer and washed three times. To all the wells 100  $\mu\text{L}$  of TMB substrate was added and wells incubated for 15 min at room temperature. Followed by addition of 50  $\mu\text{L}$  of stop solution to all wells and the plate was shaken gently to mix the solution. Control solution was prepared using 50  $\mu\text{L}$  deionized water instead of  $\text{fT}_4$  standards and the next steps were performed under the same conditions. The readings were monitored at 450 nm using a microplate ELISA reader within 15 min after adding the stopping solution. The intensity of color is inversely proportional to the concentration of  $\text{fT}_4$  in the standard solutions. A calibration curve was prepared relating absorbance of  $\text{fT}_4$  calibrators versus  $\text{fT}_4$  calibrator concentrations. The ELISA kit should be stored at 2 - 8  $^{\circ}\text{C}$  until use.

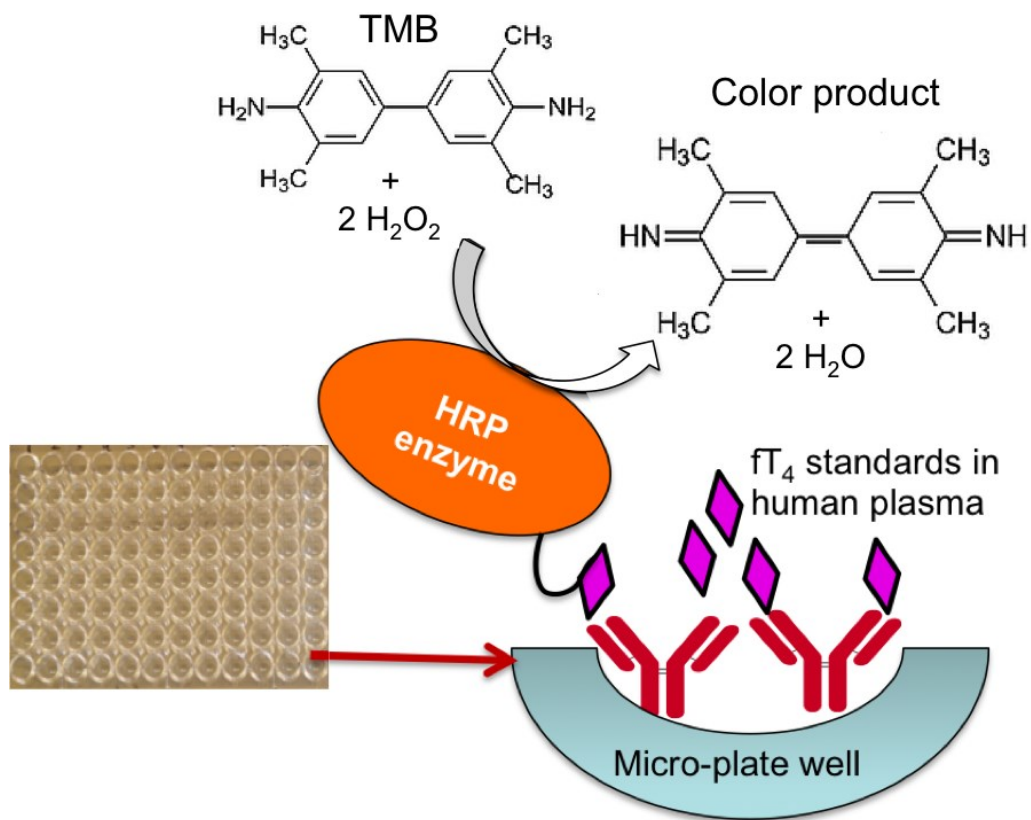


**Figure 5.04.** Schematic diagram shows ELISA indirect competitive assay platform. T<sub>4</sub>-monoclonal antibodies are immobilized on micro-plate wells and ft<sub>4</sub>-conjugated horseradish peroxidase (HRP) enzyme competes with ft<sub>4</sub> standard solution for T<sub>4</sub>-monoclonal antibody binding sites. TMB substrate is used to produce a color product at 450 nm.

### 5.2.3 *Instrumentation*

Surface enhanced Raman scattering (SERS) measurements. SERS spectra were recorded with a Renishaw inVia Raman Microscope equipped with high performance near-IR diode (785 nm, 1200 I/mm) lasers, and a CCD detector. Radiation of 785 nm from air-cooled diode laser was used for excitation. Laser power at the sample was  $5 \pm 0.5$  mW. The microscope attachment was based on a Leica system. A 5X objective focused the laser beam and a 50X objective used to collect spectra. All reported spectra were the result of 10 s integration.

ELISA reader measurements. The readings were monitored at 450 nm using a SPECTRAmax 340PC384 Microplate spectrophotometer made by Molecular Devices, Biological services, Chemistry department, University of Alberta. The reading was plotted as a graph of concentration versus absorbance.

Scanning electron microscopy (SEM) measurements. SEM images were collected using a Hitachi S4800 Field Emission SEM system from Hitachi Scientific Equipment, Japan. Image acquisition on the Hitachi SEM was carried out with a 20.00 kV accelerating voltage and a 15  $\mu$ A emission current. The working distance was 10-15 mm.

UV-vis spectroscopy measurements. CTAB capped GNRs and fT<sub>4</sub>-conjugated GNRs were centrifuged once for 10 min at 8000 rpm and suspended into 1 mL with deionized water before analysis. The extinction spectra were obtained in transmission mode on a Perkin Elmer Lambda 35 UV/VIS/NIR spectrometer with a 10 mm optical path length instrument and a photodiode

detector. The UV-vis spectra were scanned from 200 to 900 nm. Deionized water was used as the blank.

### **5.3 Result and discussion**

Figure 5.02 illustrates the indirect competitive assay platform designed for the SERS-based assay for detection of the  $fT_4$ . The two main requirements for the proposed indirect competitive SERS assay are the conjugation of GNRs with  $fT_4$  molecules and the immobilization of capture  $fT_4$ -monoclonal antibodies on a gold chip substrate. The  $fT_4$ -conjugated GNRs compete with the analyte,  $fT_4$ , for the binding sites of  $fT_4$ -monoclonal antibodies immobilized on the gold substrate. This approach relies on the indirect determination of  $fT_4$  by quantification the SERS intensity of  $fT_4$ -conjugated GNRs left on the biochip surface after competing with the  $fT_4$  solutions for antibody binding sites. As such, the higher the  $fT_4$  concentration, the greater the number of occupied antibody binding sites on the capture substrate, and the lower the amount of  $fT_4$ -conjugated Raman labels of GNRs. Thus, the observed SERS intensity decreases with an increase in the level of  $fT_4$ . This chapter will present SERS indirect competitive assay design utilizing GNRs of aspect ratio 2.4, and compared to an established ELISA competitive assay.

### 5.3.1 SERS-based competitive assay study

SERS measurements. GNRs are discussed in Chapter 2, 3 and 4 of this thesis. The rods provide better SERS enhancement than spherical gold nanoparticles. This enhancement is particularly prevalent within a few nanometers of the nanostructure surface.<sup>24</sup> Our design strategy for ERLs of GNRs includes directly immobilized tNB molecules on the GNR surface and thus maximizes SERS intensity. Figure 5.05A presents representative SERS spectra. The corresponding SERS response versus fT<sub>4</sub> concentration is plot in Figure 5.05B. Two important points can be drawn from these SERS spectra. First, the intensities of all spectral features decrease as the concentration of fT<sub>4</sub> increases. This trend follows the expectation for a competitive assay. Second, all the features in each spectrum are attributable to various vibrational modes of the tNB. For example, the bands at 1337 and 853 cm<sup>-1</sup> are respectively assigned to the symmetric stretch ( $\nu_s$  (NO<sub>2</sub>)) and scissoring mode for the nitro-group. Those at 1083, 1469 and 1572 cm<sup>-1</sup> arise from aromatic ring modes. No Raman bands are observed that can be assigned to fT<sub>4</sub> molecules linked into the GNR surface through the -SC<sub>11</sub>(EO)<sub>6</sub>-NH<sub>2</sub>. This observation is in agreement with our sandwich-based SERS assay presented in Chapter 4. There were no observable Raman active vibrational modes associated with antibody conjugated into the GNR surface. This is explained by weak Raman scattering of biological molecules and also being separated from the GNR surface by a thiolate linker.

The SERS-response versus  $fT_4$  concentration curve presented in Figure 5.05B plots the intensity of the symmetric stretch of the nitro group at  $1337\text{ cm}^{-1}$ , the strongest mode in each spectrum, against the  $fT_4$  concentration. The average intensity of spectra collected from five different locations on each sample was used to define each point. The signal exhibits a decrease with an increase in  $fT_4$  concentration. This general trend, again, is consistent with the expectation for a competitive assay.<sup>313</sup> The position of the curve in relation to analyte concentration is determined by several factors, most notably the ratio of  $fT_4$  conjugated GNRs to  $fT_4$  standard solution concentration. This parameter was manipulated for SERS-based competitive assay used in this study. Based on several experimental trials, the appropriate concentration of  $fT_4$ -conjugated GNRs was determined to be one-fifth of the initial concentration of the prepared  $fT_4$  conjugated GNRs ( $1 \times 10^{11}$  particles/mL). More importantly, serum levels of  $fT_4$  in healthy adults range from 9-23 pM or 0.7-18 ng/dL.<sup>276</sup> Serum concentrations below this range would be potentially diagnostic of hypothyroidism. This concentration range is readily, detected using our competitive SERS assay, as shown in Figure 5.05.

SEM measurements. SEM images were used to examine details of the GNR binding. The SERS assay chips at various  $fT_4$  concentrations were imaged with SEM to visualize the immobilized ERLs. Figure 5.06A and B shows representative examples for two different concentrations of  $fT_4$ . Images were collected at the same magnification and a visual inspection reveals the expected

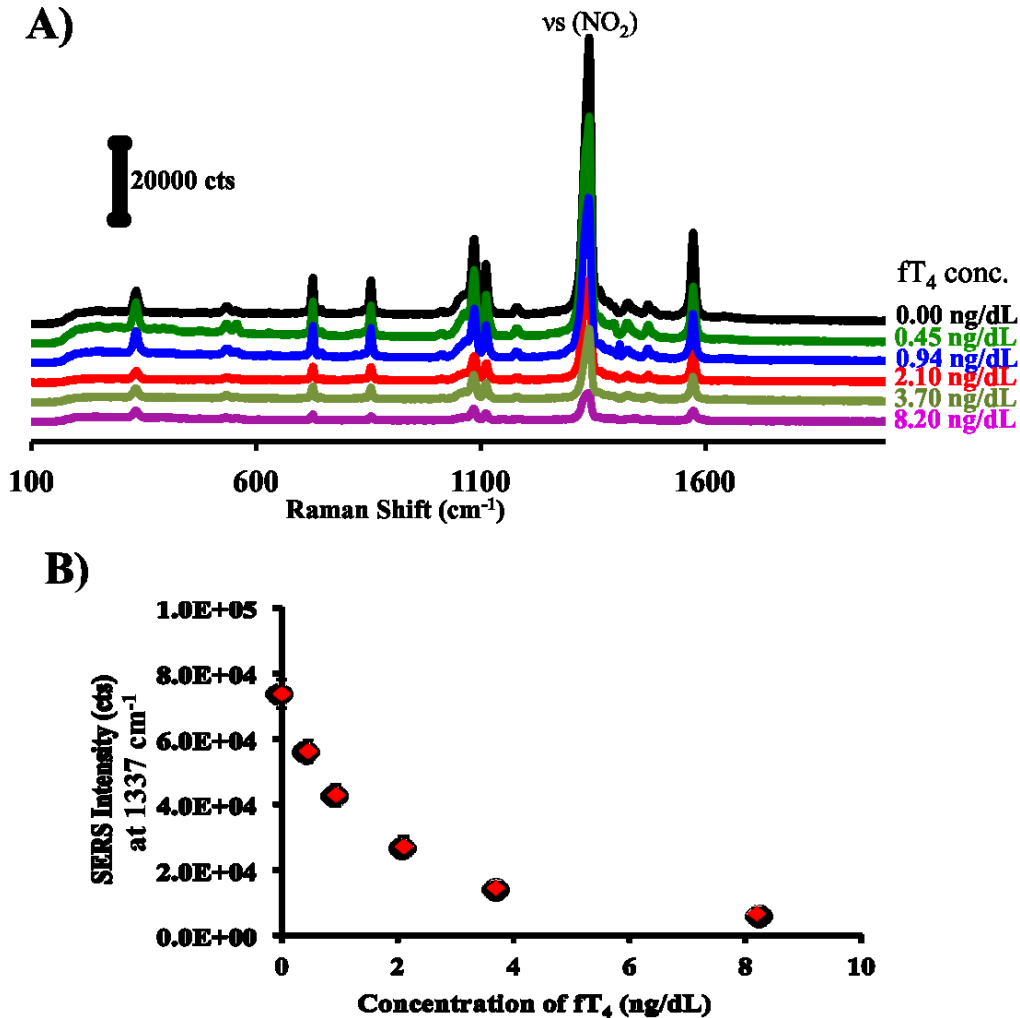


**Figure 5.05.** A) SERS spectra of 4-nitrobenzene-thiol collected from competitive assay biochips. The spectra were X-axis offset for clarity. B) A plot of SERS response versus fT<sub>4</sub> concentration. SERS response values are reported as the average intensity of symmetric stretch of the nitro group at 1337 cm<sup>-1</sup> from five independent locations of each sample, with an error bars representing the standard deviation of the mean for 10 readings collected from 2 separate assays.

trend: the GNR density decreases as the analyte concentration is increased. In both images the GNRs are generally well-dispersed on the surface, with few clusters present throughout and no evidence of large-scale aggregation. Several clusters are circled in Figure 5.06. A possible explanation for these clusters is evaporation of the solvent following incubation. The relation between aggregation and increases in SERS intensity has been reported previously. For instance, El-Sayed and co-workers reported the relative SERS peak enhancement as a function of the degree of aggregation.<sup>114</sup> The enhancement pattern of vibrations is different from that in the absence of aggregation. For all the stretching modes the relative intensities increased, whereas for some bending modes this value decreased. The change in relative enhancement was explained by differences in field symmetry in the aggregates from that in the absence of aggregation and most of SERS intensity in the aggregates originates from molecules adsorbed in the hot spots between nanoparticles in the aggregates and not on individual GNRs.<sup>114</sup>

We closely examined SERS spectra collected for tNB labeled fT<sub>4</sub>-conjugated GNRs used in the competitive assay (e.g., Figure 5.05A). These SERS spectra revealed that the relative SERS intensity of both stretching and bending modes decrease when fT<sub>4</sub> calibrator concentrations increase. Based on the argument above, the clusters shown in the SEM images do not provide additional enhancement or interfere with SERS intensity reproducibility in our competitive SERS-based assay

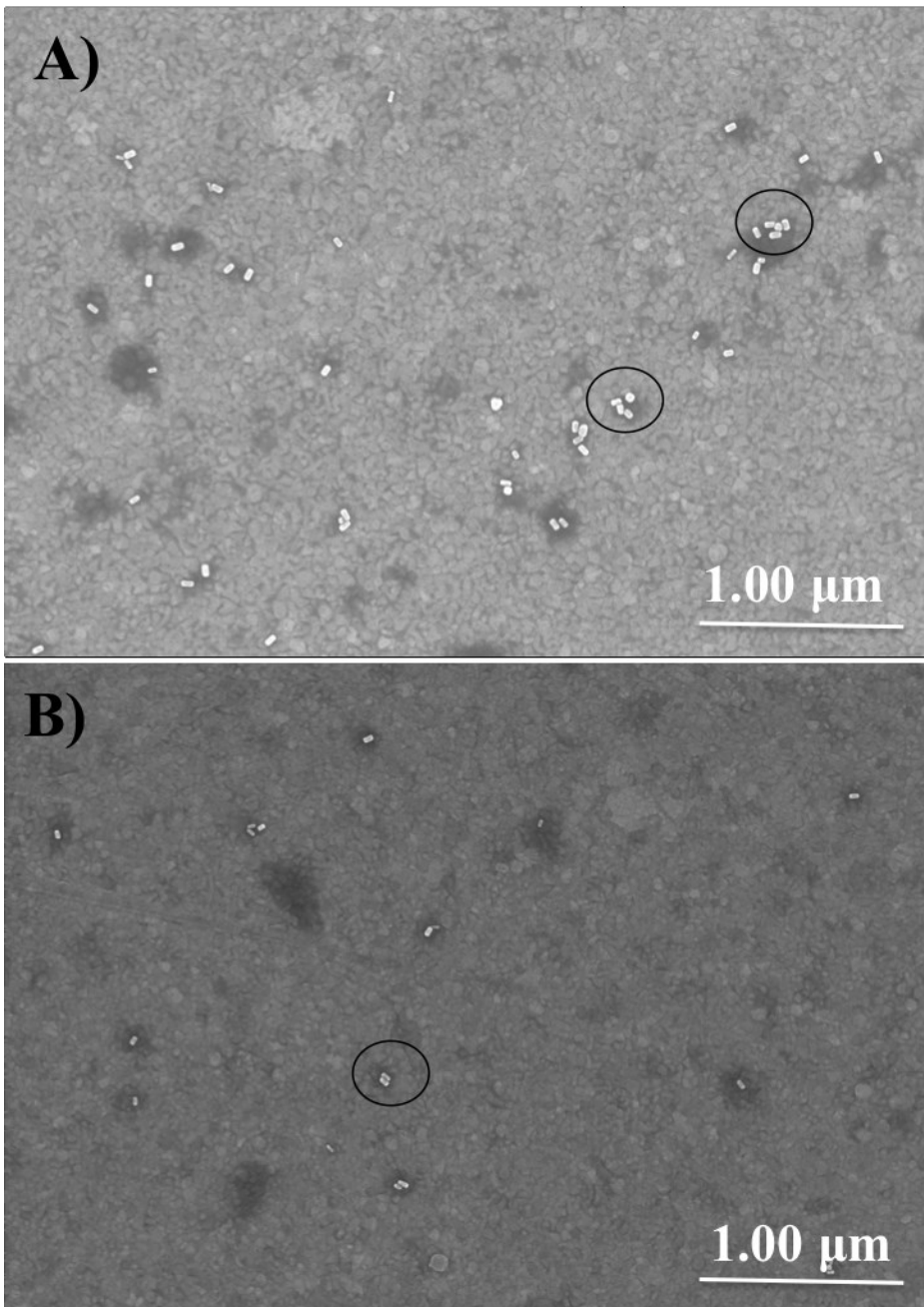


**Figure 5.06.** SEM imaging of indirect competitive SERS-based assay utilizing  $fT_4$ -conjugated GNRs:  $fT_4$ -conjugated GNRs were competing with  $fT_4$  standards for (A) 0.45 ng/dL and (B) 8.20 ng/dL.

One more issue should be addressed: the activity of the immobilized antibodies. A study by Shannon demonstrated that ~30% of the immobilized antibodies on a capture substrate were effective in target binding.<sup>314</sup> This level of activity was attributed to steric effect with respect to the spatial orientation of the capture antibody and/ or to the antibody denaturation due to interactions with the substrate surface.<sup>315</sup> Moreover, the distribution of lysine residues throughout the antibody structure points that an immobilized antibody can have a distribution of orientations.<sup>316</sup> These issues explain the random distribution of ERLs on the chip surface.

### *5.3.2 Comparison using indirect competitive ELISA platform*

The concentration-absorbance curve for the ELISA, obtained using the same concentrations of  $fT_4$  standard solutions as for the SERS measurements, is presented in Figure 5.07. The reported values for the calibration standards represent the average readings from three complete, but independent, runs on each standard for two different ELISA kits. As is evident, in Figure 5.07, the absorbance decreases as the level of  $fT_4$  increases. A comparison of these data with those in Figure 5.05B demonstrates

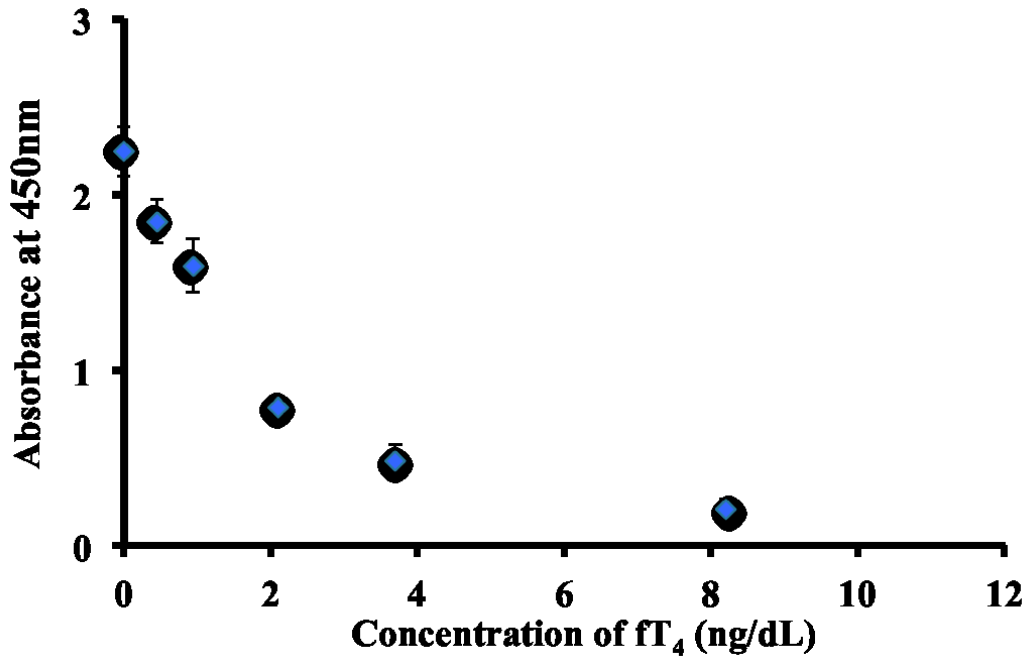


**Figure 5.07.** A plot of absorbance versus fT<sub>4</sub> concentration for ELISA assay. The error bars represent the standard deviation of the mean for six runs of 2 separate bioassays.

that our SERS assay has comparable reproducibility with the established ELISA. For ELISA the coefficient of variance (CV) for 0.45, 2.1 and 3.7 ng/dL samples are 6.7, 3.8 and 19.4%, respectively. The CVs for the SERS assay for the same three sample concentrations are 3.0, 6.3 and 8.4%. Thus, the reproducibility of the SERS assay for  $fT_4$  closely matches or is better than that for ELISA while eliminating the multistep washing procedure of ELISA.

### 5.3.3 *Langmuir adsorption isotherm fits for competitive assay responses*

To compare the results between the SERS-based and ELISA assay, we fitted both plots from Figure 5.05B and 5.07 to a Langmuir isotherm (Figure 5.08 A and B). This model assumes that: all binding sites are equivalent; monolayer coverage of  $fT_4$ -monoclonal antibodies, and  $fT_4$  molecules do not interact with each other. If concentration of  $fT_4 \gg$  immobilized affinity reagent, data from Figure 5.08A and B can be used to estimate the dissociation constants ( $K_D$ ) between the  $fT_4$ -conjugated GNRs and  $fT_4$  -monoclonal antibody and similarly between  $fT_4$  horseradish peroxidase (HRP) enzyme conjugate and  $fT_4$ -monoclonal antibody. Similar estimations have been used for SPR<sup>317</sup> and SERS<sup>318</sup>-based competitive assays. This approach is straightforward because it does not require quantification of the immobilized antibodies. Although a linear regression approach is simple, error measurements are distorted. Therefore, calculated constants should be used as estimates only. The amount of receptor – ligand complex [RL] can be expressed as

$$[RL] = [R] [L] / K_{D(L)} \quad (5-01)$$

where  $[R]$  denotes the concentration of free surface binding sites and  $[L]$  the ligand concentration, with  $K_{D(L)}$  as the dissociation constant for  $[RL]$ . During a competitive assay, the labeled reagents  $[L]$  including  $fT_4$ -conjugated GNRs and  $fT_4$ -HRP enzyme conjugates are held at fixed concentrations while the analyte ( $fT_4$ ) concentration varies. Under these conditions, concentrations, and affinity constants determine fractional binding of each competitor to the antibody-binding site. When an analyte  $[A]$  competes with a labeled ligand  $[L]$  a new equilibrium expression may be written as

$$[RA] = [R] [A] / K_{D(A)} \quad (5-02)$$

where  $[A]$  is the analyte ( $fT_4$ ) concentration,  $[RA]$  the binding site-analyte immunocomplex, and  $K_{D(A)}$  the dissociation constant for  $[RA]$ . A mass balance for the three-component system can be written for the surface receptor as

$$[R_T] = [RL] + [R] + [RA] \quad (5-03)$$

where,  $[R_T]$  is the total concentration of binding sites on the surface. Combining and rearranging equations 5.01 and 5.03 gives

$$[RL] / [R_T] = [R] [L] / K_{D(L)} / [RL] + [R] + [RA] \quad (5-04)$$

The relationship of this ratio with the SERS or absorbance response can be written as

$$\Delta R / \Delta R_{\max} = [RL] / [R_T] = [R] [L] / K_{D(L)} / [RL] + [R] + [RA] \quad (5-05)$$

Finally, by substitution equation 5.02 and rearranging, we can write

$$\Delta R / \Delta R_{\max} = (K_{D(L)} / K_{D(A)} [L]) [A] + (1 + K_{D(L)} / [L]) \quad (5-06)$$

where,  $\Delta R$  is the response (either SERS signal for SERS-based assay or absorbance value for ELISA) at a fixed concentration of the ligand and variable concentration of the analyte ( $fT_4$ ).  $\Delta R_{\max}$  is the response when the binding sites are saturated with  $fT_4$ -conjugated GNRs. A plot of  $[A]$  versus  $1/\Delta SERS$  produces a slope from which  $K_{D(L)}$  for  $fT_4$ -conjugated GNRs and  $fT_4$ -HRP enzyme conjugate can be estimated, as  $[L]$  is fixed.  $K_{D(A)}$  for  $T_4$ -monoclonal antibody was determined previously to be  $1.0 \times 10^{-8} \text{ M}$ .<sup>318</sup> Figure 5.08 show plots of  $\Delta SERS_{\max} / \Delta SERS$  and  $\Delta \text{abs}_{\max} / \Delta \text{abs}$  versus  $fT_4$  concentrations. The slope value for SERS assay was 1.26 compared with 1.24 for ELISA, whereas the intercept for SERS and ELISA assays were 0.59 and 0.51, respectively. Values found for these dissociation constants are closely matched.

This result shows that conjugation of  $fT_4$  with GNRs has no significant effect on the competition between  $fT_4$  standards and  $fT_4$ -conjugated GNRs for its surface binding sites. Furthermore, these results show that the SERS-based assay is comparable with established ELISA technique.

#### 5.3.4 Colloidal stability of $fT_4$ -conjugated GNRs

Extinction spectroscopy. The colloidal stability of GNR based SERS labels is important for assessing shelf-life of such reagents. The visible spectrum was used to monitor colloidal stability and flocculation of  $fT_4$ -conjugated GNRs in solution.<sup>177, 188</sup> The broadening of the LSPR band and shifting to longer wavelength is used as indicators of aggregation.<sup>114, 176</sup> We do not observe

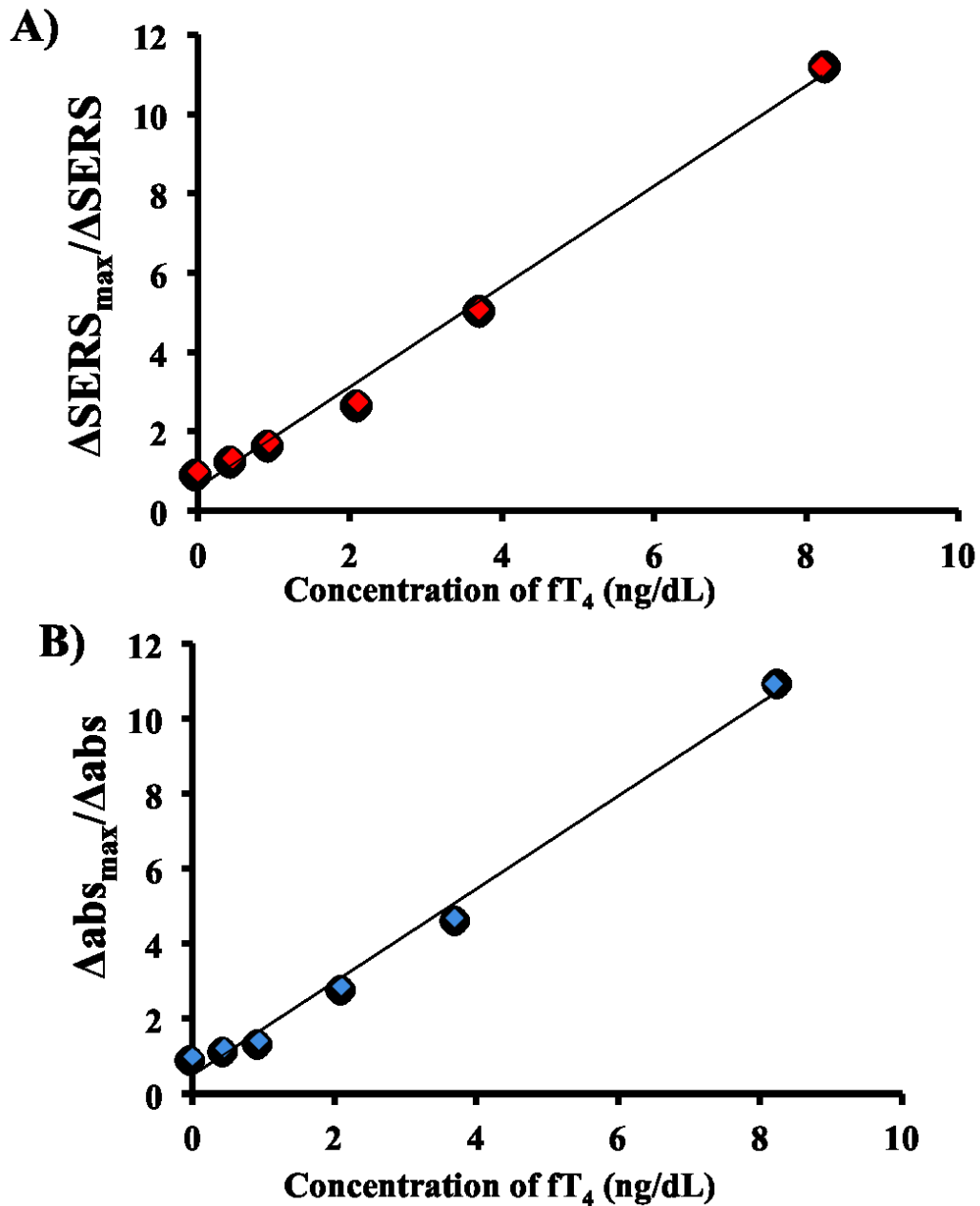


**Figure 5.08.** Plots of A)  $\Delta SERS_{max}/\Delta SERS$  and B)  $\Delta abs_{max}/\Delta abs$  versus  $ft_4$  concentrations for competitive SERS-based and ELISA assays, respectively. The fit yields  $R^2 = 0.993$  for SERS-based assay and  $R^2 = 0.991$  for ELISA.

any broadening in the extinction spectrum of fT<sub>4</sub>-conjugated GNRs as shown in Figure 5.09. The extinction spectra of GNRs before and after modification exhibit approximately  $\sim 60 \pm 2$  nm for full-width-half-maximum. The intensity of the longitudinal and transverse plasmon bands for the fT<sub>4</sub>-conjugated GNRs is slightly lower than that for unmodified CTAB capped GNRs. This is due to loss of a very small portion of the GNRs during centrifugation after each step of the modification scheme. The sensitivity of LSPR towards changes in the dielectric constant of the surrounding medium upon GNR surface modification is employed again in this chapter as an indicator for colloidal stability after fT<sub>4</sub> conjugation to the GNRs. This effect was monitored by the  $\Delta\lambda_{\text{max}}$  shift in Figure 5.09. The fT<sub>4</sub>-conjugated GNRs exhibit longitudinal and transverse plasmon bands that are red shifted by  $\sim 8$  and 4 nm, respectively. Because fT<sub>4</sub> is a small molecule, a significant change in the  $\Delta\lambda_{\text{max}}$  is not expected after fT<sub>4</sub> conjugation with -SC<sub>11</sub>(EO)<sub>6</sub>-NH<sub>2</sub>/tNB modified GNRs.

Scanning electron microscopy (SEM). Variation between GNRs in shape and size after surface modification has been reported previously. Wang and co-workers reported GNR surface modification with biological molecules such as glutathione and cysteine.<sup>319</sup> Transverse overgrowth of GNRs due to preferential binding of glutathione and cysteine to the ends of GNRs was observed. The preferential end binding blocked the growth of the GNRs in the longitudinal direction completely and allowed for the growth only in the transverse direction. As a result, the diameter of the GNR became larger while the length remained

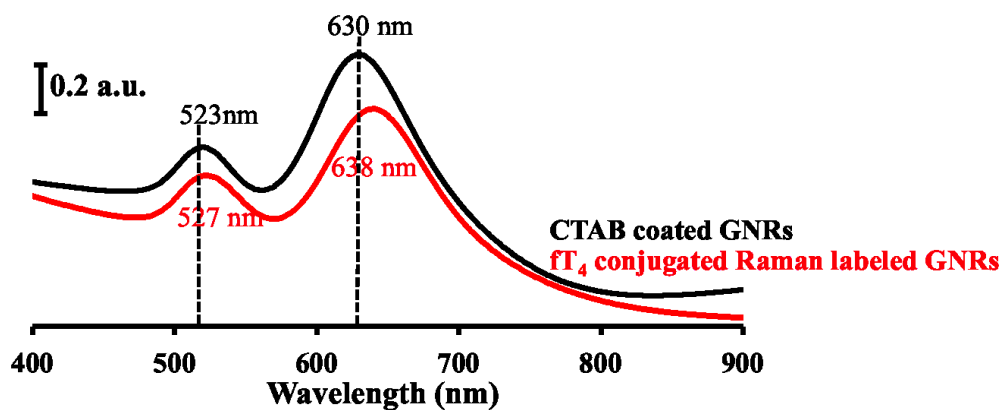


**Figure 5.09.** Extinction spectra of CTAB coated GNRs and fT<sub>4</sub> conjugated Raman labeled GNRs. The spectra were offset for clarity.

unchanged. Also the shape of the GNRs showed a gradual change from rods to either peanuts, octahedral or spheres during overgrowth. Since size and shape control the GNR plasmon frequency, constancy is crucial to prepare ERLs and conjugate them with biological molecules to realize a quantitative and reproducible assay.<sup>25, 158</sup> We used SEM to address this variability by characterizing the size and shape distribution of an aqueous solution of fT<sub>4</sub>-conjugated GNRs dropped on gold-coated glass slide and left to air-dry. Figure 5.10 presents similar sized GNRs distributed on a gold-coated glass slide. The majority of the particles are rod shaped with a diameter of  $23 \pm 6$  nm and a length of  $56 \pm 7$  nm. This agrees well with the unmodified. Some spheres are observed but as shown in Chapter 4, these can be due to the rods binding at their (111) end in a vertical manner.

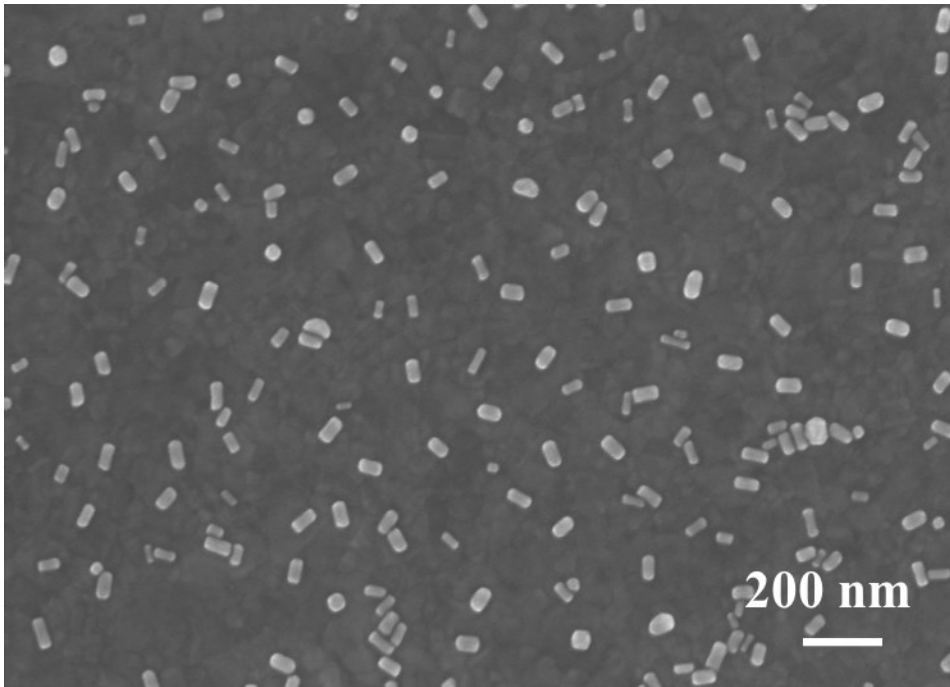


**Figure 5.10.** SEM image of the  $-\text{SC}_{11}(\text{EO})_6\text{-NH}_2/\text{tNB}$  modified GNRs after conjugation with  $\text{fT}_4$ .

## 5.4 Conclusions

We have described a successful extension of SERS-based assay utilizing ERLs of gold nanorods from a sandwich format for a large biological molecule such as IgG to one based on a competitive assay for a small metabolite molecule by focusing specifically on the biologically important free thyroxine ( $fT_4$ ). The amount of  $fT_4$  in standard solutions spiked in human plasma quantified using indirect competitive SERS-based and the results were compared with ELISA assay. The Langmuir adsorption isotherm fits showed that the binding affinity of  $fT_4$  remained unaltered after conjugation to GNRs. The reproducibility of the newly developed SERS-based assay matched that of established ELISA for  $fT_4$  and overcame one of the main disadvantages of ELISA, which was label instability where fading of the developed color within 15 to 30 min after stopping the enzyme reaction. ELISA samples should be examined within a time limit otherwise the accuracy of the results will be significantly distorted. Furthermore, the required number of washing steps for SERS-based assay was less than with ELISA test. We believe that this work sets the stage for the broader implementation of SERS-based detection utilizing ERLs of gold nanorods and other nanostructures with different size and shape to detect other small molecules. The potential of our SERS platform is concurrently detecting multiple biomarkers if configured for multiplexing application.

## 6 Chapter VI

---

### Conclusions and Future Work

#### 6.1 Chapter conclusions

The drive towards nanotechnology and its applications in biosensing was the primary motivation for the work conducted in this thesis on gold nanorods (GNRs). The thesis was divided into two distinct parts. Chapters 2 and 3 revolved around the modification of gold nanorods using 2-(2-{2-[2-(2-[2-(11-mercapto-undecyloxy) -ethoxy]-ethoxy)-ethoxy]-ethoxy}-ethoxy)-ethoxy acetic acid ( $\text{HSC}_{11}(\text{EO})_6\text{-COOH}$ ) and 4-nitrobenzenethiol (tNB) in a mixed thiolate monolayer. Chapters 4 and 5 demonstrated the use of gold nanorods as extrinsic Raman labels in SERS-based assays. Both studies provided new avenues and insights for the utilization of gold nanorods.

Chapter 2 introduced exchange of CTAB coating of gold nanorods with a mixed thiolate layer of  $-\text{SC}_{11}(\text{EO})_6\text{-COO}^-$  and tNB in an aqueous solution. Tracking of the CTAB replacement was evidenced by X-ray photoelectron spectroscopy (XPS), zeta potential measurements and high-resolution transmittance electron microscopy (HRTEM). There are three direct evidences of successful GNR surface modification. First is the disappearance of the Br 3d and N 1s signals of CTAB in the XPS spectra. Second is the reversal of the GNR surface charge from  $> +30$  eV for CTAB coated GNRs to  $> -30$  eV for  $-\text{SC}_{11}(\text{EO})_6\text{-COO}^-/\text{tNB}$  modified GNRs. Third is HRTEM imaging of

$-\text{SC}_{11}(\text{EO})_6\text{-COO}^-/\text{tNB}$  coating thickness on the GNR surface. Extinction spectroscopy and scanning electron microscopy demonstrated the colloidal stability of  $-\text{SC}_{11}(\text{EO})_6\text{-COO}^-/\text{tNB}$  modified GNRs.

In Chapter 3 the SERS intensity of 30 nm diameter GNPs and GNRs of four different aspect ratios were modified by  $-\text{SC}_{11}(\text{EO})_6\text{-COO}^-/\text{tNB}$  in aqueous solutions, were investigated. Experimentally, GNRs of aspect ratio 3.2 exhibited 10 and 100 times higher response of SERS signal than the SERS signal of the GNRs of aspect ratio 2.4 and 30 nm spherical GNPs, respectively. Lastly, these results can find applications in SERS based assays that require utilization of GNRs of different aspect ratio as Raman labels. The outcome of Chapters 2 and 3 provide a well-established scheme for designing tagged Raman probes of GNRs of different aspect ratios while maintaining their colloidal stability and optical properties.

Chapter 4 introduced preparation of bioconjugates of  $-\text{SC}_{11}(\text{EO})_6\text{-COO}^-/\text{tNB}$  modified GNRs by covalently linking the amino group of rabbit anti-goat IgG to the carboxylic acid group of  $-\text{SC}_{11}(\text{EO})_6\text{-COOH}$  linker via EDC/NHS chemistry. HRTEM and UV-vis spectroscopy were used to characterize the conjugation of the antibodies into GNR surface. Further the anti-goat immunoglobulin G (IgG) conjugated GNRs of aspect ratio 2.4 were utilized in a SERS-based sandwich assay for goat IgG. The SERS signal from the Raman reporter molecule (tNB) was correlated to the goat IgG concentration. Assays derive much of their successfulness from the limit of detection that could be

achieved. However, nonspecific binding either as a result of the capture layer on the solid support or from the gold nanoparticles. It was therefore important to assess nonspecific binding by scanning electron microscopy (SEM). The limit of detection of goat IgG was 15 fM.

Lastly, Chapter 5 described the development and preliminary testing of a competitive SERS-based assay for free thyroxine. Chapter 5 extends the many attributes of SERS based sandwich immunoassays utilizing extrinsic Raman labels of gold nanorods that have been exploited in the detection of large molecules such as goat IgG (Chapter 4) into a competitive assay for the determination of a small metabolite molecule, free thyroxine. Various concentrations of analyte (free thyroxine) were competing with thyroxine conjugated GNRs for binding sites of thyroxine-monoclonal antibodies, which were indirectly detected by correlation to the Raman response of tNB. In this fashion free thyroxine concentration as low as 0.45 ng/dL were detected, which is lower than the borderline of hypothyroidism of 0.7 ng/dL. The analytical performance of our designed SERS competitive assay match those of tests for free thyroxine that rely on enzyme labels, while using a stable label and eliminating the need for multistep washing procedure. Chapters 4 and 5 described a new approach for using the gold nanorods in SERS biosensing. Similar approaches utilizing spherical gold nanoparticles have been adopted for years in detection strategies. Gold nanorods exhibit much more localized electric field due to their shape and presence of corners that typically outperform spherical of gold

nanoparticles. Therefore it makes sense to employ these nanorods in SERS biosensing applications such as these.

## 6.2 Future work

The work conducted in this thesis shows a new and simple method to prepare bioconjugate of gold nanorods for a variety of biosensing applications. To date the majority of modification schemes rely on introducing an additional coating to cover the entire surface of the CTAB capped gold nanorods by layer-by-layer polyelectrolyte deposition method.<sup>161, 320</sup> The large size of these multilayers makes it difficult to exploit the strong localized electric field of gold nanorod for SERS applications due to the SERS distance dependence.<sup>98, 220</sup> These multilayers also increase the distance between the analyte and the GNR surface, which will reduce the sensitivity when they are used as LSPR sensor.<sup>188</sup> Further, the stability of this coating obtained through electrostatic interaction is in question for long sensing times necessary for a number of analytes in biosensing assays. This is where our proposed scheme of gold nanorod surface modification should enjoy increased attention in the near future. For instance, a solution or chip based LSPR sensing using gold nanorods has gained significant attention in recent years. This because the gold nanorods exhibit extinction efficiency that is approximately 20 times greater for rods compared to spheres.<sup>57, 186</sup> However, this application is still limited because of the challenge of gold nanorod surface functionalization with biological probes at close distance from the surface that

significantly influence the sensitivity factor. I would like to see our proposed scheme for exchange of CTAB with thiolate linker such as  $-\text{SC}_{11}(\text{EO})_6\sim\text{COOH}$ , its length measured with HRTEM to be  $2.2 \pm 0.6$  nm and conjugated with biological probes, be applied. We believe that some detailed work should be done to adjust a couple of factors such as incubation time, temperature or sonication to guarantee complete replacement of CTAB layer at this step.

The second part of this thesis is using gold nanorod bioconjugate as extrinsic Raman labels in SERS-based assays in detection of large and small biological molecules. The detection relies on the characteristic SERS spectrum of Raman reporter molecule immobilized on the gold nanorod surface, and has the capability for multiplexing by employing a variety of different labels. The ongoing issue with the usage of gold nanorods and other labels in a small molecule sensing is the conjugation of the small molecule to the nanorod without losing its binding affinity to the capture molecule. The proof-of-concept experiment demonstrated in Chapter 5 has shown a successful thyroxine-nanorod conjugate. Using gold nanorods is often preferable to multiplexed biosensors due to their tunable LSPR bands in the near infrared region. Their absorbance at higher wavelength enables use of near infrared laser excitation wavelength, as biological molecules weakly absorb photons at those wavelengths. Further the fluorescence background is minimized which improves the performance of the SERS assay. I would like to see both small and macromolecular biomarkers, which could be group of clinically related analytes,

could be detected from a single sample using SERS based assay utilizing gold nanorods.

Another material that provides promising biosensing application is silver nanorods. The Raman enhancement by silver nanorods is more efficient than by gold nanorods because the plasmon field intensity of silver rods is stronger than that of gold rods.<sup>76, 321</sup> Due to their superior properties an aligned silver nanorods array have been employed in SERS detection and are capable of providing extremely high enhancement factor.<sup>322</sup> However, the silver nanorod surface chemistry remains an issue that need to be resolved to extend biosensing to silver nanorods due to silver oxide formation.

## References

1. Sadik, O.A., W.H. Land, and J. Wang, *Targeting chemical and biological warfare agents at the molecular level*. *Electroanalysis*, 2003. **15**(14): p. 1149-1159.
2. El-Sherif, M., L. Bansal, and J.M. Yuan, *Fiber optic sensors for detection of toxic and biological threats*. *Sensors*, 2007. **7**(12): p. 3100-3118.
3. Lee, Y.C., B.S. Knox, and J.E. Garrett, *Use of cytokeratin fragments 19.1 and 19.21 (Cyfra 21-1) in the differentiation of malignant and benign pleural effusions*. *Australian and New Zealand Journal of Medicine*, 1999. **29**(6): p. 765-769.
4. Porstmann, T. and S.T. Kiessig, *Enzyme-Immunoassay Techniques - an Overview*. *Journal of Immunological Methods*, 1992. **150**(1-2): p. 5-21.
5. MacBeath, G. and S.L. Schreiber, *Printing proteins as microarrays for high-throughput function determination*. *Science*, 2000. **289**(5485): p. 1760-1763.
6. Montoya, J.R., R.L. Armstrong, and G.B. Smith, *Detection of salmonella using Surface Enhanced Raman Scattering*. *Chemical and Biological Sensing Iv*, 2003. **5085**: p. 144-152.
7. Lequin, R.M., *Enzyme Immunoassay (EIA)/Enzyme-Linked Immunosorbent Assay (ELISA)*. *Clinical Chemistry*, 2005. **51**(12): p. 2415-2418.
8. Vanweeme.Bk and A.H.W. Schuurs, *Immunoassay Using Antigen-Enzyme Conjugates*. *Febs Letters*, 1971. **15**(3): p. 232-240.

9. Eustis, S. and M.A. El-Sayed, *Determination of the aspect ratio statistical distribution of gold nanorods in solution from a theoretical fit of the observed inhomogeneously broadened longitudinal plasmon resonance absorption spectrum*. Journal of Applied Physics, 2006. **100**(4): p. 1430-1442.
10. Willets, K.A. and R.P. Van Duyne, *Localized surface plasmon resonance spectroscopy and sensing*. Annual Review of Physical Chemistry, 2007. **58**: p. 267-297.
11. Rosi, N.L. and C.A. Mirkin, *Nanostructures in biodiagnostics*. Chemical Reviews, 2005. **105**(4): p. 1547-1562.
12. Agasti, S.S., S. Rana, M.H. Park, C.K. Kim, C.C. You, and V.M. Rotello, *Nanoparticles for detection and diagnosis*. Advanced Drug Delivery Reviews, 2010. **62**(3): p. 316-328.
13. Asefa, T., C.T. Duncan, and K.K. Sharma, *Recent advances in nanostructured chemosensors and biosensors*. Analyst, 2009. **134**(10): p. 1980-1990.
14. Daniel, M.C. and D. Astruc, *Gold nanoparticles: Assembly, supramolecular chemistry, quantum-size-related properties, and applications toward biology, catalysis, and nanotechnology*. Chemical Reviews, 2004. **104**(1): p. 293-346.
15. Zayats, M., R. Baron, I. Popov, and I. Willner, *Biocatalytic growth of Au nanoparticles: From mechanistic aspects to biosensors design*. Nano Letters, 2005. **5**(1): p. 21-25.

16. Haick, H., *Chemical sensors based on molecularly modified metallic nanoparticles*. Journal of Physics D-Applied Physics, 2007. **40**(23): p. 7173-7186.
17. Cai, H.X., Y. Zhang, K.T. Yong, Z. Shao, Y.X. Li, and X.H. Zhang, *Raman Spectrum Study of 3,3'-Diethylthiatri Carbocyanine Iodide*. Spectroscopy and Spectral Analysis, 2010. **30**(12): p. 3244-3248.
18. Thobhani, S., S. Attree, R. Boyd, N. Kumarswami, J. Noble, M. Szymanski, and R.A. Porter, *Bioconjugation and characterisation of gold colloid-labelled proteins*. Journal of Immunological Methods, 2010. **356**(1-2): p. 60-69.
19. Sendroiu, I.E., L.K. Gifford, A. Luptak, and R.M. Corn, *Ultrasensitive DNA Microarray Biosensing via in Situ RNA Transcription-Based Amplification and Nanoparticle-Enhanced SPR Imaging*. Journal of the American Chemical Society, 2011. **133**(12): p. 4271-4273.
20. Wilson, R., *The use of gold nanoparticles in diagnostics and detection*. Chemical Society Reviews, 2008. **37**(9): p. 2028-2045.
21. Gregas, M.K., J.P. Scaffidi, B. Lauly, and T. Vo-Dinh, *Surface-Enhanced Raman Scattering Detection and Tracking of Nanoprobes: Enhanced Uptake and Nuclear Targeting in Single Cells*. Applied Spectroscopy, 2010. **64**(8): p. 858-866.
22. Schatz, G.C., R.P. Van Duyne, *Image Field-Theory Of Enhanced Raman-Scattering By Molecules Adsorbed On Metal-Surfaces - Detailed Comparison With Experimental Results*. Surface Science, 1980. **101**: p. 425-438.

23. Garrell, R.L., *Surface-Enhanced Raman Spectroscopy*, Analytical Chemistry, 1989. **61**: p. 401A-411A.
24. Stiles, P.L., J.A. Dieringer, N.C. Shah, and R.R. Van Duyne, *Surface-Enhanced Raman Spectroscopy*. Annual Review of Analytical Chemistry, 2008. **1**: p. 601-626.
25. Burda, C., X.B. Chen, R. Narayanan, and M.A. El-Sayed, *Chemistry and properties of nanocrystals of different shapes*. Chemical Reviews, 2005. **105**(4): p. 1025-1102.
26. Gerhold, M., A. Dhawan, and T. Vo-Dinh, *Geometry-dependent plasmon resonances of metallic nanostructures for enhancement of localized electromagnetic fields around the nanostructures - art. no. 690208*. Quantum Dots, Particles, and Nanoclusters V, 2008. **6902**: p. 90208-90208.
27. Sau, T.K. and C.J. Murphy, *Self-assembly patterns formed upon solvent evaporation of aqueous cetyltrimethylammonium bromide-coated gold nanoparticles of various shapes*. Langmuir, 2005. **21**(7): p. 2923-2929.
28. Faraday, M., Philosophical Transactions of the Royal Society, London, 1857.
29. Bohren, C.F., D. R. Huffman, *Absorption of Light by Small Particles*. Wiley: New York, 1983.
30. Van der Hulst, H.C., *Light Scattering by Small Metal Particles*. Wiley: New York, 1957.

31. Saha, K., S.S. Agasti, C. Kim, X.N. Li, and V.M. Rotello, *Gold Nanoparticles in Chemical and Biological Sensing*. Chemical Reviews, 2012. **112**(5): p. 2739-2779.
32. Mie, G., *Articles on the optical characteristics of turbid tubes, especially colloidal metal solutions*. Annalen Der Physik, 1908. **25**(3): p. 377-445.
33. Barber, P.W., R.K. Chang, and H. Massoudi, *Electrodynamic Calculations of the Surface-Enhanced Electric Intensities on Large Ag Spheroids*. Physical Review B, 1983. **27**(12): p. 7251-7261.
34. Yang, W.H., G.C. Schatz, and R.P. Van Duyne, *Discrete Dipole Approximation for Calculating Extinction and Raman Intensities for Small Particles with Arbitrary Shapes*. Journal of Chemical Physics, 1995. **103**(3): p. 869-875.
35. Purcell, E.M., C.R. Pennypac, *Scattering and Absorption of Light by Nonspherical Dielectric Grains*. Astrophysical Journal, 1973. **186**(2): p. 705-714.
36. Draine, B.T., *The Discrete-Dipole Approximation and Its Application to Interstellar Graphite Grains*. Astrophysical Journal, 1988. **333**(2): p. 848-872.
37. Draine, B.T. and P.J. Flatau, *Discrete-Dipole Approximation for Scattering Calculations*. Journal of the Optical Society of America a-Optics Image Science and Vision, 1994. **11**(4): p. 1491-1499.
38. Hao, E.C., J.T. Hupp, and G.C. Schatz, *Synthesis and optical properties of anisotropic metal nanoparticles*. Abstracts of Papers of the American Chemical Society, 2004. **227**: p. U313-U313.

39. Link, S., Z.L. Wang, and M.A. El-Sayed, *Alloy formation of gold-silver nanoparticles and the dependence of the plasmon absorption on their composition*. Journal of Physical Chemistry B, 1999. **103**(18): p. 3529-3533.
40. Evanoff, D.D. and G. Chumanov, *Size-controlled synthesis of nanoparticles. 2. Measurement of extinction, scattering, and absorption cross sections*. Journal of Physical Chemistry B, 2004. **108**(37): p. 13957-13962.
41. Talley, C.E., J.B. Jackson, C. Oubre, N.K. Grady, C.W. Hollars, S.M. Lane, T.R. Huser, P. Nordlander, and N.J. Halas, *Surface-enhanced Raman scattering from individual Au nanoparticles and nanoparticle dimer substrates*. Nano Letters, 2005. **5**(8): p. 1569-1574.
42. Njoki, P.N., I.I.S. Lim, D. Mott, H.Y. Park, B. Khan, S. Mishra, R. Sujakumar, J. Luo, and C.J. Zhong, *Size correlation of optical and spectroscopic properties for gold nanoparticles*. Journal of Physical Chemistry C, 2007. **111**(40): p. 14664-14669.
43. Seney, C.S., B.M. Gutzman, and R.H. Goddard, *Correlation of Size and Surface-Enhanced Raman Scattering Activity of Optical and Spectroscopic Properties for Silver Nanoparticles*. Journal of Physical Chemistry C, 2009. **113**(1): p. 74-80.
44. Sr, E., W.E. Haskins, and S.M. Nie, *Direct observation of size-dependent optical enhancement in single metal nanoparticles*. Journal of the American Chemical Society, 1998. **120**(31): p. 8009-8010.
45. Abalde-Cela, S., P. Aldeanueva-Potel, C. Mateo-Mateo, L. Rodriguez-Lorenzo, R.A. Alvarez-Puebla, and L.M. Liz-Marzan, *Surface-enhanced Raman scattering*

- biomedical applications of plasmonic colloidal particles*. Journal of the Royal Society Interface, 2010. **7**: p. S435-S450.
46. Moskovits, M., *Surface-enhanced Raman spectroscopy: a brief retrospective*. Journal of Raman Spectroscopy, 2005. **36**(6-7): p. 485-496.
47. Evanoff, D.D., R.L. White, and G. Chumanov, *Measuring the distance dependence of the local electromagnetic field from silver nanoparticles*. Journal of Physical Chemistry B, 2004. **108**(5): p. 1522-1524.
48. Link, S. and M.A. El-Sayed, *Size and temperature dependence of the plasmon absorption of colloidal gold nanoparticles*. Journal of Physical Chemistry B, 1999. **103**(21): p. 4212-4217.
49. Lee, S., H. Chon, M. Lee, J. Choo, S.Y. Shin, Y.H. Lee, I.J. Rhyu, S.W. Son, and C.H. Oh, *Surface-enhanced Raman scattering imaging of HER2 cancer markers overexpressed in single MCF7 cells using antibody conjugated hollow gold nanospheres*. Biosensors & Bioelectronics, 2009. **24**(7): p. 2260-2263.
50. Frens, G., *Controlled Nucleation for Regulation of Particle-Size in Monodisperse Gold Suspensions*. Nature-Physical Science, 1973. **241**(105): p. 20-22.
51. Cheng, Y., A.C. Samia, J.D. Meyers, I. Panagopoulos, B.W. Fei, and C. Burda, *Highly efficient drug delivery with gold nanoparticle vectors for in vivo photodynamic therapy of cancer*. Journal of the American Chemical Society, 2008. **130**(32): p. 10643-10647.

52. Ghosh, P., G. Han, M. De, C.K. Kim, and V.M. Rotello, *Gold nanoparticles in delivery applications*. *Advanced Drug Delivery Reviews*, 2008. **60**(11): p. 1307-1315.
53. Huang, X.H., S. Neretina, and M.A. El-Sayed, *Gold Nanorods: From Synthesis and Properties to Biological and Biomedical Applications*. *Advanced Materials*, 2009. **21**(48): p. 4880-4910.
54. El-Sayed, M.A., *Some interesting properties of metals confined in time and nanometer space of different shapes*. *Accounts of Chemical Research*, 2001. **34**(4): p. 257-264.
55. Qian, W.J., W.G. Wei, Y.X. Zhang, and Z.J. Yao, *Total synthesis, assignment of absolute stereochemistry, and structural revision of chlorofusin*. *Journal of the American Chemical Society*, 2007. **129**(20): p. 6400-6410.
56. von Maltzahn, G., A. Centrone, J.H. Park, R. Ramanathan, M.J. Sailor, T.A. Hatton, and S.N. Bhatia, *SERS-Coded Gold Nanorods as a Multifunctional Platform for Densely Multiplexed Near-infrared Imaging and Photothermal Heating*. *Advanced Materials*, 2009. **21**(31): p. 3175-3182.
57. Pissuwan, D., S.M. Valenzuela, and M.B. Cortie, *Prospects for Gold Nanorod Particles in Diagnostic and Therapeutic Applications*. *Biotechnology and Genetic Engineering Reviews*, Vol 25, 2008. **25**: p. 93-112.
58. Boca, S.C. and S. Astilean, *Detoxification of gold nanorods by conjugation with thiolated poly(ethylene glycol) and their assessment as SERS-active carriers of Raman tags*. *Nanotechnology*, 2010. **21**(23): p. 31-42.

59. Jiang, L., J. Qian, F.H. Cai, and S.L. He, *Raman reporter-coated gold nanorods and their applications in multimodal optical imaging of cancer cells*. Analytical and Bioanalytical Chemistry, 2011. **400**(9): p. 2793-2800.
60. Wang, Z.Y., S.F. Zong, J. Yang, C.Y. Song, J. Li, and Y.P. Cui, *One-step functionalized gold nanorods as intracellular probe with improved SERS performance and reduced cytotoxicity*. Biosensors & Bioelectronics, 2010. **26**(1): p. 241-247.
61. Park, H., S. Lee, L. Chen, E.K. Lee, S.Y. Shin, Y.H. Lee, S.W. Son, C.H. Oh, J.M. Song, S.H. Kang, and J. Choo, *SERS imaging of HER2-overexpressed MCF7 cells using antibody-conjugated gold nanorods*. Physical Chemistry Chemical Physics, 2009. **11**(34): p. 7444-7449.
62. Shipway, A.N., E. Katz, and I. Willner, *Nanoparticle arrays on surfaces for electronic, optical, and sensor applications*. Chemphyschem, 2000. **1**(1): p. 18-52.
63. Katz, E. and I. Willner, *Integrated nanoparticle-biomolecule hybrid systems: Synthesis, properties, and applications*. Angewandte Chemie-International Edition, 2004. **43**(45): p. 6042-6108.
64. Zamborini, F.P., L.L. Bao, and R. Dasari, *Nanoparticles in Measurement Science*. Analytical Chemistry, 2012. **84**(2): p. 541-576.
65. Tang, F.Q., X.W. Meng, D. Chen, J.G. Ran, and C.Q. Zheng, *Glucose biosensor enhanced by nanoparticles*. Science in China Series B-Chemistry, 2000. **43**(3): p. 268-274.

66. Sonvico, F., C. Dubernet, P. Colombo, and P. Couvreur, *Metallic colloid nanotechnology, applications in diagnosis and therapeutics*. Current Pharmaceutical Design, 2005. **11**(16): p. 2091-2105.
67. Guo, H.S., J.N. Zhang, P.F. Xiao, L.B. Nie, D. Yang, and N.Y. He, *Determination of cardiac troponin I for the auxiliary diagnosis of acute myocardial infarction by anodic stripping voltammetry at a carbon paste electrode*. Journal of Nanoscience and Nanotechnology, 2005. **5**(8): p. 1240-1244.
68. Huang, P.J., L.L. Tay, J. Tanha, S. Ryan, and L.K. Chau, *Single-Domain Antibody-Conjugated Nanoaggregate-Embedded Beads for Targeted Detection of Pathogenic Bacteria*. Chemistry-a European Journal, 2009. **15**(37): p. 9330-9334.
69. Lopatynskiy, A.M., O.G. Lopatynska, L.J. Guo, and V.I. Chegel, *Localized Surface Plasmon Resonance Biosensor-Part I: Theoretical Study of Sensitivity-Extended Mie Approach*. Ieee Sensors Journal, 2011. **11**(2): p. 361-369.
70. Nath, N. and A. Chilkoti, *Label-free biosensing by surface plasmon resonance of nanoparticles on glass: Optimization of nanoparticle size*. Analytical Chemistry, 2004. **76**(18): p. 5370-5378.
71. Dahint, R., E. Trileva, H. Acumnan, U. Konrad, M. Zimmer, V. Stadler, and M. Himmelhaus, *Optically responsive nanoparticle layers for the label-free analysis of biospecific interactions in array formats*. Biosensors & Bioelectronics, 2007. **22**(12): p. 3174-3181.

72. Shao, Y.L., S.P. Xu, X.L. Zheng, Y. Wang, and W.Q. Xu, *Optical Fiber LSPR Biosensor Prepared by Gold Nanoparticle Assembly on Polyelectrolyte Multilayer*. *Sensors*, 2010. **10**(4): p. 3585-3596.
73. Englebienne, P., *Use of colloidal gold surface plasmon resonance peak shift to infer affinity constants from the interactions between protein antigens and antibodies specific for single or multiple epitopes*. *Analyst*, 1998. **123**(7): p. 1599-1603.
74. Aslan, K., J.R. Lakowicz, and C.D. Geddes, *Nanogold plasmon resonance-based glucose sensing. 2. Wavelength-ratiometric resonance light scattering*. *Analytical Chemistry*, 2005. **77**(7): p. 2007-2014.
75. Anker, J.N., W.P. Hall, O. Lyandres, N.C. Shah, J. Zhao, and R.P. Van Duyne, *Biosensing with plasmonic nanosensors*. *Nature Materials*, 2008. **7**(6): p. 442-453.
76. Lee, K.S. and M.A. El-Sayed, *Gold and silver nanoparticles in sensing and imaging: Sensitivity of plasmon response to size, shape, and metal composition*. *Journal of Physical Chemistry B*, 2006. **110**(39): p. 19220-19225.
77. Jain, P.K., I.H. El-Sayed, and M.A. El-Sayed, *Au nanoparticles target cancer (vol 2, pg 18, 2007)*. *Nano Today*, 2007. **2**(2): p. 16-22.
78. Zhang, N., Y.Y. Liu, L.L. Tong, K.H. Xu, L.H. Zhuo, and B. Tang, *A novel assembly of AuNPs-beta-CDs-FL for the fluorescent probing of cholesterol and its application in blood serum*. *Analyst*, 2008. **133**(9): p. 1176-1181.

79. Maxwell, D.J., J.R. Taylor, and S.M. Nie, *Self-assembled nanoparticle probes for recognition and detection of biomolecules*. Journal of the American Chemical Society, 2002. **124**(32): p. 9606-9612.
80. Guo, S.J. and E.K. Wang, *Synthesis and electrochemical applications of gold nanoparticles*. Analytica Chimica Acta, 2007. **598**(2): p. 181-192.
81. Mao, X. and G.D. Liu, *Nanomaterial Based Electrochemical DNA Biosensors and Bioassays*. Journal of Biomedical Nanotechnology, 2008. **4**(4): p. 419-431.
82. Wang, L., J.Y. Bai, P.F. Huang, H.J. Wang, L.Y. Zhang, and Y.Q. Zhao, *Self-assembly of gold nanoparticles for the voltammetric sensing of epinephrine*. Electrochemistry Communications, 2006. **8**(6): p. 1035-1040.
83. Smith, E. and G. Dent, *Modern Raman Spectroscopy: A Practical Approach*. Modern Raman Spectroscopy: A Practical Approach, 2005: p. 1-210.
84. Kang, J.W., X.N. Li, G.F. Wu, Z.H. Wang, and X.Q. Lu, *A new scheme of hybridization based on the Au-nano-DNA modified glassy carbon electrode*. Analytical Biochemistry, 2007. **364**(2): p. 165-170.
85. Ambrosi, A., M.T. Castaneda, A.J. Killard, M.R. Smyth, S. Alegret, and A. Merkoci, *Double-codified gold nanolabels for enhanced immunoanalysis*. Analytical Chemistry, 2007. **79**(14): p. 5232-5240.
86. Chen, C.R., D.Y. Liu, Z.S. Wu, Q.M. Luo, G.L. Shen, and R.Q. Yu, *Sensitive label-free electrochemical immunoassay by electrocatalytic amplification*. Electrochemistry Communications, 2009. **11**(10): p. 1869-1872.

87. Schlucker, S., *SERS Microscopy: Nanoparticle Probes and Biomedical Applications*. Chemphyschem, 2009. **10**(9-10): p. 1344-1354.
88. Fleischm.M, P.J. Hendra, and Mcquilla.Aj, *Raman-Spectra of Pyridine Adsorbed at a Silver Electrode*. Chemical Physics Letters, 1974. **26**(2): p. 163-166.
89. Albrecht, M.G. and J.A. Creighton, *Anomalously Intense Raman-Spectra of Pyridine at a Silver Electrode*. Journal of the American Chemical Society, 1977. **99**(15): p. 5215-5217.
90. Jeanmaire, D.L. and R.P. Vanduyne, *Surface Raman Spectroelectrochemistry .I. Heterocyclic, Aromatic, and Aliphatic-Amines Adsorbed on Anodized Silver Electrode*. Journal of Electroanalytical Chemistry, 1977. **84**(1): p. 1-20.
91. Doering, W.E., M.E. Piotti, M.J. Natan, and R.G. Freeman, *SERS as a foundation for nanoscale, optically detected biological labels*. Advanced Materials, 2007. **19**(20): p. 3100-3108.
92. Jarvis, R.M. and R. Goodacre, *Characterisation and identification of bacteria using SERS*. Chemical Society Reviews, 2008. **37**(5): p. 931-936.
93. Qian, X.M. and S.M. Nie, *Single-molecule and single-nanoparticle SERS: from fundamental mechanisms to biomedical applications*. Chemical Society Reviews, 2008. **37**(5): p. 912-920.
94. Kneipp, K., H. Kneipp, I. I, R.R. Dasari, and M.S. Feld, *Ultrasensitive chemical analysis by Raman spectroscopy*. Chemical Reviews, 1999. **99**(10): p. 2957-2964.

95. Banholzer, M.J., J.E. Millstone, L.D. Qin, and C.A. Mirkin, *Rationally designed nanostructures for surface-enhanced Raman spectroscopy*. Chemical Society Reviews, 2008. **37**(5): p. 885-897.
96. Nie, S.M. and S.R. Emery, *Probing single molecules and single nanoparticles by surface-enhanced Raman scattering*. Science, 1997. **275**(5303): p. 1102-1106.
97. Stockman, M.I., *Electromagnetic theory of SERS*. Surface-Enhanced Raman Scattering: Physics and Applications, 2006. **103**: p. 47-65.
98. Schatz, G.C., M.A. Young, and R.P. Van Duyne, *Electromagnetic mechanism of SERS*. Surface-Enhanced Raman Scattering: Physics and Applications, 2006. **103**: p. 19-45.
99. Otto, A., *On the significance of Shalaev's 'hot spots' in ensemble and single-molecule SERS by adsorbates on metallic films at the percolation threshold*. Journal of Raman Spectroscopy, 2006. **37**(9): p. 937-947.
100. Campion, A. and P. Kambhampati, *Surface-enhanced Raman scattering*. Chemical Society Reviews, 1998. **27**(4): p. 241-250.
101. Michaels, A.M., J. Jiang, and L. Brus, *Ag nanocrystal junctions as the site for surface-enhanced Raman scattering of single Rhodamine 6G molecules*. Journal of Physical Chemistry B, 2000. **104**(50): p. 11965-11971.
102. Kneipp, K., H. Kneipp, I. Itzkan, R.R. Dasari, and M.S. Feld, *Surface-enhanced Raman scattering and biophysics*. Journal of Physics-Condensed Matter, 2002. **14**(18): p. R597-R624.

103. Wang, R., C.W. Yu, F.B.A. Yu, and L.X. Chen, *Molecular fluorescent probes for monitoring pH changes in living cells*. *Trac-Trends in Analytical Chemistry*, 2010. **29**(9): p. 1004-1013.
104. Porter, M.D., R.J. Lipert, L.M. Siperko, G. Wang, and R. Narayanan, *SERS as a bioassay platform: fundamentals, design, and applications*. *Chemical Society Reviews*, 2008. **37**(5): p. 1001-1011.
105. Doering, W.E. and S.M. Nie, *Spectroscopic tags using dye-embedded nanoparticles and surface-enhanced Raman scattering*. *Analytical Chemistry*, 2003. **75**(22): p. 6171-6176.
106. Qian, X.M., X.H. Peng, D.O. Ansari, Q. Yin-Goen, G.Z. Chen, D.M. Shin, L. Yang, A.N. Young, M.D. Wang, and S.M. Nie, *In vivo tumor targeting and spectroscopic detection with surface-enhanced Raman nanoparticle tags*. *Nature Biotechnology*, 2008. **26**(1): p. 83-90.
107. Cao, Y.W.C., R.C. Jin, and C.A. Mirkin, *Nanoparticles with Raman spectroscopic fingerprints for DNA and RNA detection*. *Science*, 2002. **297**(5586): p. 1536-1540.
108. Cao, Y.C., R.C. Jin, J.M. Nam, C.S. Thaxton, and C.A. Mirkin, *Raman dye-labeled nanoparticle probes for proteins*. *Journal of the American Chemical Society*, 2003. **125**(48): p. 14676-14677.
109. Sha, M.Y., H.X. Xu, M.J. Natan, and R. Cromer, *Surface-Enhanced Raman Scattering Tags for Rapid and Homogeneous Detection of Circulating Tumor*

- Cells in the Presence of Human Whole Blood*. Journal of the American Chemical Society, 2008. **130**(51): p. 17214-17220.
110. Rule, K.L. and P.J. Vikesland, *Surface-Enhanced Resonance Raman Spectroscopy for the Rapid Detection of Cryptosporidium parvum and Giardia lamblia*. Environmental Science & Technology, 2009. **43**(4): p. 1147-1152.
111. Burns, D.H., S. Rosendahl, D. Bandilla, O.C. Maes, H.M. Chertkow, and H.M. Schipper, *Near-Infrared Spectroscopy of Blood Plasma for Diagnosis of Sporadic Alzheimer's Disease*. Journal of Alzheimers Disease, 2009. **17**(2): p. 391-397.
112. Tong, L., Q.S. Wei, A. Wei, and J.X. Cheng, *Gold Nanorods as Contrast Agents for Biological Imaging: Optical Properties, Surface Conjugation and Photothermal Effects*. Photochemistry and Photobiology, 2009. **85**(1): p. 21-32.
113. Huang, X.H., I.H. El-Sayed, W. Qian, and M.A. El-Sayed, *Cancer cells assemble and align gold nanorods conjugated to antibodies to produce highly enhanced, sharp, and polarized surface Raman spectra: A potential cancer diagnostic marker*. Nano Letters, 2007. **7**(6): p. 1591-1597.
114. Nikoobakht, B. and M.A. El-Sayed, *Surface-enhanced Raman scattering studies on aggregated gold nanorods*. Journal of Physical Chemistry A, 2003. **107**(18): p. 3372-3378.
115. Grubisha, D.S., R.J. Lipert, H.Y. Park, J. Driskell, and M.D. Porter, *Femtomolar detection of prostate-specific antigen: An immunoassay based on surface-*

- enhanced Raman scattering and immunogold labels*. Analytical Chemistry, 2003. **75**(21): p. 5936-5943.
116. Ansar, S.M., G.S. Perera, D.P. Jiang, R.A. Holler, and D.M. Zhang, *Organothiols Self-Assembled onto Gold: Evidence for Deprotonation of the Sulfur-Bound Hydrogen and Charge Transfer from Thiolate*. Journal of Physical Chemistry C, 2013. **117**(17): p. 8793-8798.
117. Sun, L., K.B. Sung, C. Dentinger, B. Lutz, L. Nguyen, J.W. Zhang, H.Y. Qin, M. Yamakawa, M.Q. Cao, Y. Lu, A.J. Chmura, J. Zhu, X. Su, A.A. Berlin, S. Chan, and B. Knudsen, *Composite organic-inorganic nanoparticles as Raman labels for tissue analysis*. Nano Letters, 2007. **7**(2): p. 351-356.
118. Alivisatos, A.P., *Perspectives on the physical chemistry of semiconductor nanocrystals*. Journal of Physical Chemistry, 1996. **100**(31): p. 13226-13239.
119. Steigerwald, M.L., A.P. Alivisatos, J.M. Gibson, T.D. Harris, R. Kortan, A.J. Muller, A.M. Thayer, T.M. Duncan, D.C. Douglass, and L.E. Brus, *Surface Derivatization and Isolation of Semiconductor Cluster Molecules*. Journal of the American Chemical Society, 1988. **110**(10): p. 3046-3050.
120. Murray, C.B., C.R. Kagan, and M.G. Bawendi, *Synthesis and characterization of monodisperse nanocrystals and close-packed nanocrystal assemblies*. Annual Review of Materials Science, 2000. **30**: p. 545-610.
121. Ni, J., R.J. Lipert, G.B. Dawson, and M.D. Porter, *Immunoassay readout method using extrinsic Raman labels adsorbed on immunogold colloids*. Analytical Chemistry, 1999. **71**(21): p. 4903-4908.

122. Kim, K., H.K. Park, and N.H. Kim, *Silver-particle-based surface-enhanced Raman scattering spectroscopy for biomolecular sensing and recognition*. *Langmuir*, 2006. **22**(7): p. 3421-3427.
123. Luo, S.Z., J. Xu, Y.F. Zhang, S.Y. Liu, and C. Wu, *Double hydrophilic block copolymer monolayer protected hybrid gold nanoparticles and their shell cross-linking*. *Journal of Physical Chemistry B*, 2005. **109**(47): p. 22159-22166.
124. Hotchkiss, J.W., A.B. Lowe, and S.G. Boyes, *Surface modification of gold nanorods with polymers synthesized by reversible addition-fragmentation chain transfer polymerization*. *Chemistry of Materials*, 2007. **19**(1): p. 6-13.
125. Vericat, C., M.E. Vela, G. Benitez, P. Carro, and R.C. Salvarezza, *Self-assembled monolayers of thiols and dithiols on gold: new challenges for a well-known system*. *Chemical Society Reviews*, 2010. **39**(5): p. 1805-1834.
126. Porter, M.D., T.B. Bright, D.L. Allara, and C.E.D. Chidsey, *Spontaneously Organized Molecular Assemblies .4. Structural Characterization of Normal-Alkyl Thiol Monolayers on Gold by Optical Ellipsometry, Infrared-Spectroscopy, and Electrochemistry*. *Journal of the American Chemical Society*, 1987. **109**(12): p. 3559-3568.
127. Frey, S., V. Stadler, K. Heister, W. Eck, M. Zharnikov, M. Grunze, B. Zeysing, and A. Terfort, *Structure of thioaromatic self-assembled monolayers on gold and silver*. *Langmuir*, 2001. **17**(8): p. 2408-2415.

128. Love, J.C., L.A. Estroff, J.K. Kriebel, R.G. Nuzzo, and G.M. Whitesides, *Self-assembled monolayers of thiolates on metals as a form of nanotechnology*. Chemical Reviews, 2005. **105**(4): p. 1103-1169.
129. Kim, D.J., S.M. Kang, B. Kong, W.J. Kim, H.J. Paik, H. Choi, and I.S. Choi, *Formation of thermoresponsive gold nanoparticle/PNIPAAm hybrids by surface-initiated, atom transfer radical polymerization in aqueous media*. Macromolecular Chemistry and Physics, 2005. **206**(19): p. 1941-1946.
130. Raula, J., J. Shan, M. Nuopponen, A. Niskanen, H. Jiang, E.I. Kauppinen, and H. Tenhu, *Synthesis of gold nanoparticles grafted with a thermoresponsive polymer by surface-induced reversible-addition-fragmentation chain-transfer polymerization*. Langmuir, 2003. **19**(8): p. 3499-3504.
131. Huang, Y., V.P. Swarup, and S.W. Bishnoi, *Rapid Raman Imaging of Stable, Functionalized Nanoshells in Mammalian Cell Cultures*. Nano Letters, 2009. **9**(8): p. 2914-2920.
132. Nguyen, C.T., J.T. Nguyen, S. Rutledge, J.N. Zhang, C. Wang, and G.C. Walker, *Detection of chronic lymphocytic leukemia cell surface markers using surface enhanced Raman scattering gold nanoparticles*. Cancer Letters, 2010. **292**(1): p. 91-97.
133. Tan, X.B., Z.Y. Wang, J. Yang, C.Y. Song, R.H. Zhang, and Y.P. Cui, *Polyvinylpyrrolidone- (PVP-) coated silver aggregates for high performance surface-enhanced Raman scattering in living cells*. Nanotechnology, 2009. **20**(44): P. 40-49.

134. Xu, D., J.J. Gu, W.N. Wang, X.C. Yu, K. Xi, and X.D. Jia, *Development of chitosan-coated gold nanoflowers as SERS-active probes*. *Nanotechnology*, 2010. **21**(37).
135. Potara, M., D. Maniu, and S. Astilean, *The synthesis of biocompatible and SERS-active gold nanoparticles using chitosan*. *Nanotechnology*, 2009. **20**(31).
136. Weng, K.C., C.O. Noble, B. Papahadjopoulos-Sternberg, F.F. Chen, D.C. Drummond, D.B. Kirpotin, D.H. Wang, Y.K. Hom, B. Hann, and J.W. Park, *Targeted tumor cell internalization and imaging of multifunctional quantum dot-conjugated immunoliposomes in vitro and in vivo*. *Nano Letters*, 2008. **8**(9): p. 2851-2857.
137. Ip, S., C.M. MacLaughlin, N. Gunari, and G.C. Walker, *Phospholipid Membrane Encapsulation of Nanoparticles for Surface-Enhanced Raman Scattering*. *Langmuir*, 2011. **27**(11): p. 7024-7033.
138. Mulvaney, S.P., M.D. Musick, C.D. Keating, and M.J. Natan, *Glass-coated, analyte-tagged nanoparticles: A new tagging system based on detection with surface-enhanced Raman scattering*. *Langmuir*, 2003. **19**(11): p. 4784-4790.
139. Li, J.F., Y.F. Huang, Y. Ding, Z.L. Yang, S.B. Li, X.S. Zhou, F.R. Fan, W. Zhang, Z.Y. Zhou, D.Y. Wu, B. Ren, Z.L. Wang, and Z.Q. Tian, *Shell-isolated nanoparticle-enhanced Raman spectroscopy*. *Nature*, 2010. **464**(7287): p. 392-395.
140. Caruso, F., *Nanoengineering of particle surfaces*. *Advanced Materials*, 2001. **13**(1): p. 11-16.

141. Nikoobakht, B., J.P. Wang, and M.A. El-Sayed, *Surface-enhanced Raman scattering of molecules adsorbed on gold nanorods: off-surface plasmon resonance condition*. Chemical Physics Letters, 2002. **366**(1-2): p. 17-23.
142. Orendorff, C.J., A. Gole, T.K. Sau, and C.J. Murphy, *Surface-enhanced Raman spectroscopy of self-assembled monolayers: Sandwich architecture and nanoparticle shape dependence*. Analytical Chemistry, 2005. **77**(10): p. 3261-3266.
143. Gole, A. and C.J. Murphy, *Polyelectrolyte-coated gold nanorods: Synthesis, characterization and immobilization*. Chemistry of Materials, 2005. **17**(6): p. 1325-1330.
144. Jana, N.R., L. Gearheart, and C.J. Murphy, *Seed-mediated growth approach for shape-controlled synthesis of spheroidal and rod-like gold nanoparticles using a surfactant template*. Advanced Materials, 2001. **13**(18): p. 1389-1393.
145. Yu, Y.Y., S.S. Chang, C.L. Lee, and C.R.C. Wang, *Gold nanorods: Electrochemical synthesis and optical properties*. Journal of Physical Chemistry B, 1997. **101**(34): p. 6661-6664.
146. Esumi, K., K. Matsuhisa, and K. Torigoe, *Preparation of Rodlike Gold Particles by Uv Irradiation Using Cationic Micelles as a Template*. Langmuir, 1995. **11**(9): p. 3285-3287.
147. Jana, N.R., L. Gearheart, and C.J. Murphy, *Evidence for seed-mediated nucleation in the chemical reduction of gold salts to gold nanoparticles*. Chemistry of Materials, 2001. **13**(7): p. 2313-2322.

148. Vigderman, L., B.P. Khanal, and E.R. Zubarev, *Functional Gold Nanorods: Synthesis, Self-Assembly, and Sensing Applications*. Advanced Materials, 2012. **24**(36): p. 4811-4841.
149. Caswell, K.K., J.N. Wilson, U.H.F. Bunz, and C.J. Murphy, *Preferential end-to-end assembly of gold nanorods by biotin-streptavidin connectors*. Journal of the American Chemical Society, 2003. **125**(46): p. 13914-13915.
150. Chang, J.Y., H.M. Wu, H. Chen, Y.C. Ling, and W.H. Tan, *Oriented assembly of Au nanorods using biorecognition system*. Chemical Communications, 2005(8): p. 1092-1094.
151. Yu, C.X., L. Varghese, and J. Irudayaraj, *Surface modification of cetyltrimethylammonium bromide-capped gold nanorods to make molecular probes*. Langmuir, 2007. **23**(17): p. 9114-9119.
152. Dai, Q., J. Coutts, J.H. Zou, and Q. Huo, *Surface modification of gold nanorods through a place exchange reaction inside an ionic exchange resin*. Chemical Communications, 2008(25): p. 2858-2860.
153. Larson-Smith, K. and D.C. Pozzo, *Competitive Adsorption of Thiolated Poly(ethylene glycol) and Alkane-Thiols on Gold Nanoparticles and Its Effect on Cluster Formation*. Langmuir, 2012. **28**(37): p. 13157-13165.
154. Nandan, E., N.R. Jana, and J.Y. Ying, *Functionalization of gold nanospheres and nanorods by chitosan oligosaccharide derivatives*. Advanced Materials, 2008. **20**(11): p. 2068-2074.

155. Takahashi, H., Y. Niidome, T. Niidome, K. Kaneko, H. Kawasaki, and S. Yamada, *Modification of gold nanorods using phosphatidylcholine to reduce cytotoxicity*. Langmuir, 2006. **22**(1): p. 2-5.
156. Orendorff, C.J., T.M. Alam, D.Y. Sasaki, B.C. Bunker, and J.A. Voigt, *Phospholipid-Gold Nanorod Composites*. ACS Nano, 2009. **3**(4): p. 971-983.
157. Huang, J.Y., K.S. Jackson, and C.J. Murphy, *Polyelectrolyte Wrapping Layers Control Rates of Photothermal Molecular Release from Gold Nanorods*. Nano Letters, 2012. **12**(6): p. 2982-2987.
158. Murphy, C.J., T.K. San, A.M. Gole, C.J. Orendorff, J.X. Gao, L. Gou, S.E. Hunyadi, and T. Li, *Anisotropic metal nanoparticles: Synthesis, assembly, and optical applications*. Journal of Physical Chemistry B, 2005. **109**(29): p. 13857-13870.
159. Orendorff, C.J., P.L. Hankins, and C.J. Murphy, *pH-triggered assembly of gold nanorods*. Langmuir, 2005. **21**(5): p. 2022-2026.
160. Singh, A.K., S.A. Khan, Z. Fan, T. Demeritte, D. Senapati, R. Kanchanapally, and P.C. Ray, *Development of a Long-Range Surface-Enhanced Raman Spectroscopy Ruler*. Journal of the American Chemical Society, 2012. **134**(20): p. 8662-8669.
161. Sivapalan, S.T., B.M. DeVetter, T.K. Yang, T. van Dijk, M.V. Schulmerich, P.S. Carney, R. Bhargava, and C.J. Murphy, *Off-Resonance Surface-Enhanced Raman Spectroscopy from Gold Nanorod Suspensions as a Function of Aspect Ratio: Not What We Thought*. ACS Nano, 2013. **7**(3): p. 2099-2105.

162. Alkilany, A.M., P.K. Nalaria, M.D. Wyatt, and C.J. Murphy, *Cation Exchange on the Surface of Gold Nanorods with a Polymerizable Surfactant: Polymerization, Stability, and Toxicity Evaluation*. Langmuir, 2010. **26**(12): p. 9328-9333.
163. Gole, A. and C.J. Murphy, *Azide-derivatized gold nanorods: Functional materials for "Click" chemistry*. Langmuir, 2008. **24**(1): p. 266-272.
164. Turner, N.H. and J.A. Schreifels, *Surface-Analysis - X-Ray Photoelectron-Spectroscopy and Auger-Electron Spectroscopy*. Analytical Chemistry, 1994. **66**(12): p. R163-R185.
165. Rahman, M.A., J.I. Son, M.S. Won, and Y.B. Shim, *Gold Nanoparticles Doped Conducting Polymer Nanorod Electrodes: Ferrocene Catalyzed Aptamer-Based Thrombin Immunosensor*. Analytical Chemistry, 2009. **81**(16): p. 6604-6611.
166. Murphy, C.J., L.B. Thompson, A.M. Alkilany, P.N. Sisco, S.P. Boulos, S.T. Sivapalan, J.A. Yang, D.J. Chernak, and J.Y. Huang, *The Many Faces of Gold Nanorods*. Journal of Physical Chemistry Letters, 2010. **1**(19): p. 2867-2875.
167. Hubert, F., F. Testard, and O. Spalla, *Cetyltrimethylammonium bromide silver bromide complex as the capping agent of gold nanorods*. Langmuir, 2008. **24**(17): p. 9219-9222.
168. Wagner, C.D., *X-Ray Photoelectron-Spectroscopy with X-Ray Photons of Higher Energy*. Journal of Vacuum Science & Technology, 1978. **15**(2): p. 518-523.

169. Guzenko, A.F., A.L. Yudin, N.A. Yatsyna, and L.V. Kolesnikov, *Interaction of thiocarbocyanine polymethine dyes with the surface of silver bromide sols*. High Energy Chemistry, 2005. **39**(5): p. 318-323.
170. Baio, J.E., T. Weidner, J. Brison, D.J. Graham, L.J. Gamble, and D.G. Castner, *Amine terminated SAMs: Investigating why oxygen is present in these films*. Journal of Electron Spectroscopy and Related Phenomena, 2009. **172**(1-3): p. 2-8.
171. Liu, X.H., X.H. Luo, S.X. Lu, J.C. Zhang, and W.L. Cao, *A novel cetyltrimethyl ammonium silver bromide complex and silver bromide nanoparticles obtained by the surfactant counterion*. Journal of Colloid and Interface Science, 2007. **307**(1): p. 94-100.
172. Duwez, A.S., *Exploiting electron spectroscopies to probe the structure and organization of self-assembled monolayers: a review*. Journal of Electron Spectroscopy and Related Phenomena, 2004. **134**(2-3): p. 97-138.
173. Ahren, M., L. Selegard, A. Klasson, F. Soderlind, N. Abrikossova, C. Skoglund, T. Bengtsson, M. Engstrom, P.O. Kall, and K. Uvdal, *Synthesis and Characterization of PEGylated Gd<sub>2</sub>O<sub>3</sub> Nanoparticles for MRI Contrast Enhancement*. Langmuir, 2010. **26**(8): p. 5753-5762.
174. Castner, D.G., K. Hinds, and D.W. Grainger, *X-ray photoelectron spectroscopy sulfur 2p study of organic thiol and disulfide binding interactions with gold surfaces*. Langmuir, 1996. **12**(21): p. 5083-5086.

175. Bain, C.D., J. Evall, and G.M. Whitesides, *Formation of Monolayers by the Coadsorption of Thiols on Gold - Variation in the Head Group, Tail Group, and Solvent*. Journal of the American Chemical Society, 1989. **111**(18): p. 7155-7164.
176. Gole, A. and C.J. Murphy, *Biotin-streptavidin-induced aggregation of gold nanorods: Tuning rod-rod orientation*. Langmuir, 2005. **21**(23): p. 10756-10762.
177. Weisbecker, C.S., M.V. Merritt, and G.M. Whitesides, *Molecular self-assembly of aliphatic thiols on gold colloids*. Langmuir, 1996. **12**(16): p. 3763-3772.
178. Nikoobakht, B. and M.A. El-Sayed, *Evidence for bilayer assembly of cationic surfactants on the surface of gold nanorods*. Langmuir, 2001. **17**(20): p. 6368-6374.
179. Gole, A., C.J. Orendorff, and C.J. Murphy, *Immobilization of gold nanorods onto acid-terminated self-assembled monolayers via electrostatic interactions*. Langmuir, 2004. **20**(17): p. 7117-7122.
180. Gomez-Grana, S., F. Hubert, F. Testard, A. Guerrero-Martinez, I. Grillo, L.M. Liz-Marzan, and O. Spalla, *Surfactant (Bi)Layers on Gold Nanorods*. Langmuir, 2012. **28**(2): p. 1453-1459.
181. Meldrum, F.C., J. Flath, and W. Knoll, *Chemical deposition of PbS on self-assembled monolayers of 16-mercaptohexadecanoic acid*. Langmuir, 1997. **13**(7): p. 2033-2049.
182. Schreiber, F., *Structure and growth of self-assembling monolayers*. Progress in Surface Science, 2000. **65**(5-8): p. 151-256.

183. Gai, P.L. and M.A. Harmer, *Surface atomic defect structures and growth of gold nanorods*. Nano Letters, 2002. **2**(7): p. 771-774.
184. Badia, A., W. Gao, S. Singh, L. Demers, L. Cuccia, and L. Reven, *Structure and chain dynamics of alkanethiol-capped gold colloids*. Langmuir, 1996. **12**(5): p. 1262-1269.
185. Camillone, N., C.E.D. Chidsey, G.Y. Liu, T.M. Putvinski, and G. Scoles, *Surface-Structure and Thermal Motion of Normal-Alkane Thiols Self-Assembled on Au(111) Studied by Low-Energy Helium Diffraction*. Journal of Chemical Physics, 1991. **94**(12): p. 8493-8502.
186. Jain, P.K., K.S. Lee, I.H. El-Sayed, and M.A. El-Sayed, *Calculated absorption and scattering properties of gold nanoparticles of different size, shape, and composition: Applications in biological imaging and biomedicine*. Journal of Physical Chemistry B, 2006. **110**(14): p. 7238-7248.
187. Lee, K.S. and M.A. El-Sayed, *Dependence of the enhanced optical scattering efficiency relative to that of absorption for gold metal nanorods on aspect ratio, size, end-cap shape, and medium refractive index*. Journal of Physical Chemistry B, 2005. **109**(43): p. 20331-20338.
188. Malinsky, M.D., K.L. Kelly, G.C. Schatz, and R.P. Van Duyne, *Chain length dependence and sensing capabilities of the localized surface plasmon resonance of silver nanoparticles chemically modified with alkanethiol self-assembled monolayers*. Journal of the American Chemical Society, 2001. **123**(7): p. 1471-1482.

189. Ohki, S., *Dielectric Constant and Refractive Index of Lipid Bilayers*. Journal of Theoretical Biology, 1968. **19**(1): p. 97-105.
190. Jakubowicz, A., H. Jia, R.M. Wallace, and B.E. Gnade, *Adsorption kinetics of p-nitrobenzenethiol self-assembled monolayers on a gold surface*. Langmuir, 2005. **21**(3): p. 950-955.
191. Mandal, M., S. Kundu, T.K. Sau, S.M. Yusuf, and T. Pal, *Synthesis and characterization of superparamagnetic Ni-Pt nanoalloy*. Chemistry of Materials, 2003. **15**(19): p. 3710-3715.
192. Contreras-Caceres, R., C. Dawson, P. Formanek, D. Fischer, F. Simon, A. Janke, P. Uhlmann, and M. Stamm, *Polymers as Templates for Au and Au@Ag Bimetallic Nanorods: UV-Vis and Surface Enhanced Raman Spectroscopy*. Chemistry of Materials, 2013. **25**(2): p. 158-169.
193. Lu, G.W., C. Li, and G.Q. Shi, *Synthesis and characterization of 3D dendritic gold nanostructures and their use as substrates for surface-enhanced raman scattering*. Chemistry of Materials, 2007. **19**(14): p. 3433-3440.
194. Nikoobakht, B., Z.L. Wang, and M.A. El-Sayed, *Self-assembly of gold nanorods*. Journal of Physical Chemistry B, 2000. **104**(36): p. 8635-8640.
195. Kawamura, G., Y. Yang, and M. Nogami, *Facile assembling of gold nanorods with large aspect ratio and their surface-enhanced Raman scattering properties*. Applied Physics Letters, 2007. **90**(26): P. 30-38.

196. Wang, Y., A.E. DePrince, S.K. Gray, X.M. Lin, and M. Pelton, *Solvent-Mediated End-to-End Assembly of Gold Nanorods*. Journal of Physical Chemistry Letters, 2010. **1**(18): p. 2692-2698.
197. Jana, N.R., L.A. Gearheart, S.O. Obare, C.J. Johnson, K.J. Edler, S. Mann, and C.J. Murphy, *Liquid crystalline assemblies of ordered gold nanorods*. Journal of Materials Chemistry, 2002. **12**(10): p. 2909-2912.
198. Boca, S.C. and S. Astilean, *Detoxification of gold nanorods by conjugation with thiolated poly(ethylene glycol) and their assessment as SERS-active carriers of Raman tags*. Nanotechnology, 2010. **21**(23): p. 80-89.
199. Koglin, E., A. Tarazona, S. Kreisig, and M.J. Schwuger, *In-situ investigations of coadsorbed cationic surfactants on charged surfaces: A SERS microprobe study*. Colloids and Surfaces a-Physicochemical and Engineering Aspects, 1997. **123**: p. 523-542.
200. Griffith, W.P. and T.Y. Koh, *Vibrational-Spectra of 1,2-Benzenedithiol, 2-Aminothiophenol and 2-Aminophenol and Their Ser Spectra*. Spectrochimica Acta Part a-Molecular and Biomolecular Spectroscopy, 1995. **51**(2): p. 253-267.
201. varsanyl, G., *assignment for vibrational spectra of seven hundred benzene derivatives*. 1974, Newyork: John wiley and sons.
202. Skadtchenko, B.O. and R. Aroca, *Surface-enhanced Raman scattering of p-nitrothiophenol - Molecular vibrations of its silver salt and the surface complex formed on silver islands and colloids*. Spectrochimica Acta Part a-Molecular and Biomolecular Spectroscopy, 2001. **57**(5): p. 1009-1016.

203. Narayanan, R., R.J. Lipert, and M.D. Porter, *Cetyltrimethylammonium bromide-modified spherical and cube-like gold nanoparticles as extrinsic Raman labels in surface-enhanced Raman spectroscopy based heterogeneous immunoassays*. Analytical Chemistry, 2008. **80**(6): p. 2265-2271.
204. Zong, S.F., Z.Y. Wang, J. Yang, and Y.P. Cui, *Intracellular pH Sensing Using p-Aminothiophenol Functionalized Gold Nanorods with Low Cytotoxicity*. Analytical Chemistry, 2011. **83**(11): p. 4178-4183.
205. Cai, H.X., J. Zhu, G. Chen, L.W. Liu, G.S. He, and X.H. Zhang, *Surface-enhanced Raman scattering and DFT calculations studies of 3,3'-diethylthiatricarbocyanine iodide*. Journal of Raman Spectroscopy, 2011. **42**(9): p. 1722-1727.
206. Jokerst, J.V., A.J. Cole, D. Van de Sompel, and S.S. Gambhir, *Gold Nanorods for Ovarian Cancer Detection with Photoacoustic Imaging and Resection Guidance via Raman Imaging in Living Mice*. ACS Nano, 2012. **6**(11): p. 10366-10377.
207. Creighton, J.A. and D.G. Eadon, *Ultraviolet Visible Absorption-Spectra of the Colloidal Metallic Elements*. Journal of the Chemical Society-Faraday Transactions, 1991. **87**(24): p. 3881-3891.
208. Link, S., M.B. Mohamed, and M.A. El-Sayed, *Simulation of the optical absorption spectra of gold nanorods as a function of their aspect ratio and the effect of the medium dielectric constant*. Journal of Physical Chemistry B, 1999. **103**(16): p. 3073-3077.

209. Bright, R.M., M.D. Musick, and M.J. Natan, *Preparation and characterization of Ag colloid monolayers*. Langmuir, 1998. **14**(20): p. 5695-5701.
210. Weimer, W.A. and M.J. Dyer, *Tunable surface plasmon resonance silver films*. Applied Physics Letters, 2001. **79**(19): p. 3164-3166.
211. Haynes, C.L. and R.P. Van Duyne, *Plasmon-sampled surface-enhanced Raman excitation spectroscopy*. Journal of Physical Chemistry B, 2003. **107**(30): p. 7426-7433.
212. McFarland, A.D., M.A. Young, J.A. Dieringer, and R.P. Van Duyne, *Wavelength-scanned surface-enhanced Raman excitation spectroscopy*. Journal of Physical Chemistry B, 2005. **109**(22): p. 11279-11285.
213. Mahmoud, M.A., R. Narayanan, and M.A. El-Sayed, *Enhancing Colloidal Metallic Nanocatalysis: Sharp Edges and Corners for Solid Nanoparticles and Cage Effect for Hollow Ones*. Accounts of Chemical Research, 2013. **46**(8): p. 1795-1805.
214. Zhu, J. and F.K. Li, *Effect of aspect ratio on the inter-surface plasmonic coupling of tubular gold nanoparticle*. European Physical Journal B, 2011. **80**(1): p. 83-87.
215. McPhillips, J., A. Murphy, M.P. Jonsson, W.R. Hendren, R. Atkinson, F. Hook, A.V. Zayats, and R.J. Pollard, *High-Performance Biosensing Using Arrays of Plasmonic Nanotubes*. Acs Nano, 2010. **4**(4): p. 2210-2216.
216. Near, R.D., S.C. Hayden, R.E. Hunter, D. Thackston, and M.A. El-Sayed, *Rapid and Efficient Prediction of Optical Extinction Coefficients for Gold Nanospheres*

- and Gold Nanorods*. Journal of Physical Chemistry C, 2013. **117**(45): p. 23950-23955.
217. Orendorff, C.J., L. Gearheart, N.R. Jana, and C.J. Murphy, *Aspect ratio dependence on surface enhanced Raman scattering using silver and gold nanorod substrates*. Physical Chemistry Chemical Physics, 2006. **8**(1): p. 165-170.
218. Zavaleta, C.L., B.R. Smith, I. Walton, W. Doering, G. Davis, B. Shojaei, M.J. Natan, and S.S. Gambhir, *Multiplexed imaging of surface enhanced Raman scattering nanotags in living mice using noninvasive Raman spectroscopy*. Proceedings of the National Academy of Sciences of the United States of America, 2009. **106**(32): p. 13511-13516.
219. Sivapalan, S.T., B.M. DeVetter, T.K. Yang, M.V. Schulmerich, R. Bhargava, and C.J. Murphy, *Surface-Enhanced Raman Spectroscopy of Polyelectrolyte-Wrapped Gold Nanoparticles in Colloidal Suspension*. Journal of Physical Chemistry C, 2013. **117**(20): p. 10677-10682.
220. Kennedy, B.J., S. Spaeth, M. Dickey, and K.T. Carron, *Determination of the distance dependence and experimental effects for modified SERS substrates based on self-assembled monolayers formed using alkanethiols*. Journal of Physical Chemistry B, 1999. **103**(18): p. 3640-3646.
221. Xu, H.X., E.J. Bjerneld, M. Kall, and L. Borjesson, *Spectroscopy of single hemoglobin molecules by surface enhanced Raman scattering*. Physical Review Letters, 1999. **83**(21): p. 4357-4360.

222. Jiang, J., K. Bosnick, M. Maillard, and L. Brus, *Single molecule Raman spectroscopy at the junctions of large Ag nanocrystals*. Journal of Physical Chemistry B, 2003. **107**(37): p. 9964-9972.
223. Tabor, C., R. Murali, M. Mahmoud, and M.A. El-Sayed, *On the Use of Plasmonic Nanoparticle Pairs As a Plasmon Ruler: The Dependence of the Near-Field Dipole Plasmon Coupling on Nanoparticle Size and Shape*. Journal of Physical Chemistry A, 2009. **113**(10): p. 1946-1953.
224. Jain, P.K., S. Eustis, and M.A. El-Sayed, *Plasmon coupling in nanorod assemblies: Optical absorption, discrete dipole approximation simulation, and exciton-coupling model*. Journal of Physical Chemistry B, 2006. **110**(37): p. 18243-18253.
225. Li, L., C.K. Tsung, T. Ming, Z.H. Sun, W.H. Ni, Q.H. Shi, G.D. Stucky, and J.F. Wang, *Multifunctional Mesoporous Silica Microspheres from an Ultrasonic Aerosol Spray*. Advanced Functional Materials, 2008. **18**(19): p. 2956-2962.
226. Xu, H.X., J. Aizpurua, M. Kall, and P. Apell, *Electromagnetic contributions to single-molecule sensitivity in surface-enhanced Raman scattering*. Physical Review E, 2000. **62**(3): p. 4318-4324.
227. Blatchford, C.G., J.R. Campbell, and J.A. Creighton, *Plasma Resonance Enhanced Raman-Scattering by Adsorbates on Gold Colloids - the Effects of Aggregation*. Surface Science, 1982. **120**(2): p. 435-455.
228. Orendorff, C.J., A.M. Gole, T.K. Sau, and C.J. Murphy, *Sandwich architecture for surface enhanced Raman spectroscopy of self-assembled monolayers and*

- dependence on nanoparticle shape*. Abstracts of Papers of the American Chemical Society, 2005. **230**: p. U1090-U1090.
229. Guo, H.Y., F.X. Ruan, L.H. Lu, J.W. Hu, J.A. Pan, Z.L. Yang, and B. Ren, *Correlating the Shape, Surface Plasmon Resonance, and Surface-Enhanced Raman Scattering of Gold Nanorods*. Journal of Physical Chemistry C, 2009. **113**(24): p. 10459-10464.
230. Mahmoud, M.A. and M.A. El-Sayed, *Different Plasmon Sensing Behavior of Silver and Gold Nanorods*. Journal of Physical Chemistry Letters, 2013. **4**(9): p. 1541-1545.
231. Yuen, C., W. Zheng, and Z.W. Huang, *Optimization of extinction efficiency of gold-coated polystyrene bead substrates improves surface-enhanced Raman scattering effects by post-growth microwave heating treatment*. Journal of Raman Spectroscopy, 2010. **41**(4): p. 374-380.
232. Mirkin, C.A., *The Polyvalent Gold Nanoparticle Conjugate-Materials Synthesis, Biodiagnostics, and Intracellular Gene Regulation*. Mrs Bulletin, 2010. **35**(7): p. 532-539.
233. Jans, H. and Q. Huo, *Gold nanoparticle-enabled biological and chemical detection and analysis*. Chemical Society Reviews, 2012. **41**(7): p. 2849-2866.
234. Woo, J.R., D.K. Lim, and J.M. Nam, *Minimally Stable Nanoparticle-Based Colorimetric Assay for Simple, Rapid, and Sensitive Antibody Structure and Activity Evaluation*. Small, 2011. **7**(5): p. 648-655.

235. Wang, Y., S. Astilean, G. Haran, and A. Warshawsky, *Microenvironmental investigation of polymer-bound fluorescent chelator by fluorescence microscopy and optical spectroscopy*. Analytical Chemistry, 2001. **73**(17): p. 4096-4103.
236. Li, C., C.L. Wu, J.S. Zheng, J.P. Lai, C.L. Zhang, and Y.B. Zhao, *LSPR Sensing of Molecular Biothiols Based on Noncoupled Gold Nanorods*. Langmuir, 2010. **26**(11): p. 9130-9135.
237. Morsin, M., A.A. Umar, M.M. Salleh, and B.Y. Majlis, *High Sensitivity Localized Surface Plasmon Resonance Sensor of Gold Nanoparticles : Surface Density Effect for Detection of Boric Acid*. 2012 10th IEEE International Conference on Semiconductor Electronics (Icse), 2012: p. 352-356.
238. Olofsson, L., T. Rindzevicius, I. Pfeiffer, M. Kall, and F. Hook, *Surface-based gold-nanoparticle sensor for specific and quantitative DNA hybridization detection*. Langmuir, 2003. **19**(24): p. 10414-10419.
239. Zhang, L.D. and M. Fang, *Nanomaterials in pollution trace detection and environmental improvement*. Nano Today, 2010. **5**(2): p. 128-142.
240. Kim, S., J. Lee, S.J. Lee, and H.J. Lee, *Ultra-sensitive detection of IgE using biofunctionalized nanoparticle-enhanced SPR*. Talanta, 2010. **81**(4-5): p. 1755-1759.
241. Frederix, F., J.M. Friedt, K.H. Choi, W. Laureyn, A. Campitelli, D. Mondelaers, G. Maes, and G. Borghs, *Biosensing based on light absorption of nanoscaled gold and silver particles*. Analytical Chemistry, 2003. **75**(24): p. 6894-6900.

242. Rohr, T.E., T. Cotton, N. Fan, and P.J. Tarcha, *Immunoassay Employing Surface-Enhanced Raman-Spectroscopy*. Analytical Biochemistry, 1989. **182**(2): p. 388-398.
243. Graham, D., B.J. Mallinder, D. Whitcombe, N.D. Watson, and W.E. Smith, *Simple multiplex genotyping by surface-enhanced resonance Raman scattering*. Analytical Chemistry, 2002. **74**(5): p. 1069-1075.
244. Driskell, J.D., K.M. Kwarta, R.J. Lipert, M.D. Porter, J.D. Neill, and J.F. Ridpath, *Low-level detection of viral pathogens by a surface-enhanced Raman scattering based immunoassay*. Analytical Chemistry, 2005. **77**(19): p. 6147-6154.
245. Yakes, B.J., R.J. Lipert, J.P. Bannantine, and M.D. Porter, *Detection of Mycobacterium avium subsp paratuberculosis by a sonicate immunoassay based on surface-enhanced Raman scattering*. Clinical and Vaccine Immunology, 2008. **15**(2): p. 227-234.
246. Dufek, E.J., B. Ehlert, M.C. Granger, T.M. Sandrock, S.L. Legge, M.G. Herrmann, A.W. Meikle, and M.D. Porter, *Competitive surface-enhanced Raman scattering assay for the 1,25-dihydroxy metabolite of vitamin D-3*. Analyst, 2010. **135**(11): p. 2811-2817.
247. He, Y. and G.Q. Shi, *Surface plasmon resonances of silver triangle nanoplates: Graphic assignments of resonance modes and linear fittings of resonance peaks*. Journal of Physical Chemistry B, 2005. **109**(37): p. 17503-17511.

248. Zhang, Z.S., X.R. Su, J.B. Li, Z.H. Hao, and L. Zhou, *Localized Surface Plasmon of Thin Gold Film with Periodic Arrays of Nanoholes*. *Modern Physics Letters B*, 2009. **23**(2): p. 147-153.
249. McFarland, A.D. and R.P. Van Duyne, *Single silver nanoparticles as real-time optical sensors with zeptomole sensitivity*. *Nano Letters*, 2003. **3**(8): p. 1057-1062.
250. Tang, X.L., P. Jiang, G.L. Ge, M. Tsuji, S.S. Xie, and Y.J. Guo, *Poly(N-vinyl-2-pyrrolidone) (PVP)-capped dendritic gold nanoparticles by a one-step hydrothermal route and their high SERS effect*. *Langmuir*, 2008. **24**(5): p. 1763-1768.
251. McLellan, J.M., A. Siekkinen, J.Y. Chen, and Y.N. Xia, *Comparison of the surface-enhanced Raman scattering on sharp and truncated silver nanocubes*. *Chemical Physics Letters*, 2006. **427**(1-3): p. 122-126.
252. Evanoff, D.D. and G. Chumanov, *Synthesis and optical properties of silver nanoparticles and arrays*. *Chemphyschem*, 2005. **6**(7): p. 1221-1231.
253. Hall, W.P., S.N. Ngatia, and R.P. Van Duyne, *LSPR Biosensor Signal Enhancement Using Nanoparticle-Antibody Conjugates*. *Journal of Physical Chemistry C*, 2011. **115**(5): p. 1410-1414.
254. Chen, Y.L., S.C. Kung, D.K. Taggart, A.R. Halpern, R.M. Penner, and R.M. Corn, *Fabricating Nanoscale DNA Patterns with Gold Nanowires*. *Analytical Chemistry*, 2010. **82**(8): p. 3365-3370.

255. Liang, K.Z., J.S. Qi, W.J. Mu, and Z.G. Chen, *Biomolecules/gold nanowires-doped sol-gel film for label-free electrochemical immunoassay of testosterone*. Journal of Biochemical and Biophysical Methods, 2008. **70**(6): p. 1156-1162.
256. Gao, J.X., C.M. Bender, and C.J. Murphy, *Dependence of the gold nanorod aspect ratio on the nature of the directing surfactant in aqueous solution*. Langmuir, 2003. **19**(21): p. 9065-9070.
257. Liao, H.W. and J.H. Hafner, *Gold nanorod bioconjugates*. Chemistry of Materials, 2005. **17**(18): p. 4636-4641.
258. Gole, A.M. and C.J. Murphy, *Biotin-Streptavidin directed side to side assembly of gold nanorods*. Abstracts of Papers of the American Chemical Society, 2005. **230**: p. U1237-U1237.
259. Durr, N.J., T. Larson, D.K. Smith, B.A. Korgel, K. Sokolov, and A. Ben-Yakar, *Two-photon luminescence imaging of cancer cells using molecularly targeted gold nanorods*. Nano Letters, 2007. **7**(4): p. 941-945.
260. Huang, X.H., I.H. El-Sayed, W. Qian, and M.A. El-Sayed, *Cancer cell imaging and photothermal therapy in the near-infrared region by using gold nanorods*. Journal of the American Chemical Society, 2006. **128**(6): p. 2115-2120.
261. Chen, C.D., S.F. Cheng, L.K. Chau, and C.R.C. Wang, *Sensing capability of the localized surface plasmon resonance of gold nanorods*. Biosensors & Bioelectronics, 2007. **22**(6): p. 926-932.

262. Wang, C.G., Y. Chen, T.T. Wang, Z.F. Ma, and Z.M. Su, *Biorecognition-driven self-assembly of gold nanorods: A rapid and sensitive approach toward antibody sensing*. Chemistry of Materials, 2007. **19**(24): p. 5809-5811.
263. Wang, L.B., Y.Y. Zhu, L.G. Xu, W. Chen, H. Kuang, L.Q. Liu, A. Agarwal, C.L. Xu, and N.A. Kotov, *Side-by-Side and End-to-End Gold Nanorod Assemblies for Environmental Toxin Sensing*. Angewandte Chemie-International Edition, 2010. **49**(32): p. 5472-5475.
264. Chen, R.J., Y.G. Zhang, D.W. Wang, and H.J. Dai, *Noncovalent sidewall functionalization of single-walled carbon nanotubes for protein immobilization*. Journal of the American Chemical Society, 2001. **123**(16): p. 3838-3839.
265. Kamogawa, M., J. Shimanuki, T. Azuma, A. Murakami, and T. Ishiguro, *Transmission Electron Microscopy Observation of Antibody*. Iumrs International Conference in Asia 2011, 2012. **36**: p. 150-153.
266. Kanda, V., J.K. Kariuki, D.J. Harrison, and M.T. McDermott, *Label-free reading of microarray-based immunoassays with surface plasmon resonance imaging*. Analytical Chemistry, 2004. **76**(24): p. 7257-7262.
267. Zalipsky, S. and J.M. Harris, *Introduction to chemistry and biological applications of poly(ethylene glycol)*. Poly(Ethylene Glycol), 1997. **680**: p. 1-13.
268. Deible, C.R., P. Petrosko, P.C. Johnson, E.J. Beckman, A.J. Russell, and W.R. Wagner, *Molecular barriers to biomaterial thrombosis by modification of surface proteins with polyethylene glycol*. Biomaterials, 1998. **19**(20): p. 1885-1893.

269. Zheng, M., Z.G. Li, and X.Y. Huang, *Ethylene glycol monolayer protected nanoparticles: Synthesis, characterization, and interactions with biological molecules*. Langmuir, 2004. **20**(10): p. 4226-4235.
270. Luan, Q.F., K.B. Zhou, H.N. Tan, D. Yang, and X. Yao, *Au-NPs enhanced SPR biosensor based on hairpin DNA without the effect of nonspecific adsorption*. Biosensors & Bioelectronics, 2011. **26**(5): p. 2473-2477.
271. Wang, G.F., H.Y. Park, and R.J. Lipert, *Mixed Monolayers on Gold Nanoparticle Labels for Multiplexed Surface-Enhanced Raman Scattering Based Immunoassays*. Analytical Chemistry, 2009. **81**(23): p. 9643-9650.
272. Grant, C., *Development and characterization of interfacial chemistry for biomolecule immobilization in surface plasmon resonance (SPR) imaging studies*. University of Alberta, Edmonton, Alberta. 2009.
273. Costa, J.C.S., R.A. Ando, A.C. Sant'Ana, L.M. Rossi, P.S. Santos, M.L.A. Temperini, and P. Corio, *High performance gold nanorods and silver nanocubes in surface-enhanced Raman spectroscopy of pesticides*. Physical Chemistry Chemical Physics, 2009. **11**(34): p. 7491-7498.
274. Markel, V.A., V.M. Shalaev, P. Zhang, W. Huynh, L. Tay, T.L. Haslett, and M. Moskovits, *Near-field optical spectroscopy of individual surface-plasmon modes in colloid clusters*. Physical Review B, 1999. **59**(16): p. 10903-10909.
275. Utiger, R.D., *Serum Triiodoth Ronine in Man*. Annual Review of Medicine, 1974. **25**: p. 289-302.

276. Ekins, R., *Analytic Measurements of Free-Thyroxine*. Clinics in Laboratory Medicine, 1993. **13**(3): p. 599-630.
277. Bouknight, A.L., *Thyroid physiology and thyroid function testing*. Otolaryngologic Clinics of North America, 2003. **36**(1): p. 9-16.
278. Ekins, R., *One-Step, Labeled-Antibody Assay for Measuring Free-Thyroxine .I. Assay Development and Validation*. Clinical Chemistry, 1992. **38**(11): p. 2355-2357.
279. Robbins, J., *Thyroxine Transport and the Free Hormone Hypothesis*. Endocrinology, 1992. **131**(2): p. 546-547.
280. Ekins, R., *The Free Hormone Hypothesis and Measurement of Free Hormones*. Clinical Chemistry, 1992. **38**(7): p. 1289-1293.
281. Papadoyannis, I.N., V.F. Samanidou, and L.A. Kovatsi, *A rapid high performance liquid chromatographic (HPLC) assay for the determination of oxytetracycline in commercial pharmaceuticals*. Journal of Pharmaceutical and Biomedical Analysis, 2000. **23**(2-3): p. 275-280.
282. Nair, N., M.R.A. Pillai, R.S. Mani, S. Naik, M. Desai, P. Upadhye, and M.P. Colaco, *A Single Reagent Radioimmunoassay for Thyroxine in Blood-Samples Absorbed on Filter-Paper for Mass-Screening of Neonatal-Hypothyroidism*. Journal of Radioanalytical and Nuclear Chemistry-Articles, 1988. **122**(1): p. 129-135.
283. Tagliaro, F., M. Camilot, R. Valentini, F. Mengarda, F. Antoniazzi, and L. Tato, *Determination of thyroxine in the hair of newborns by radioimmunoassay with*

- high-performance liquid chromatographic confirmation.* Journal of Chromatography B, 1998. **716**(1-2): p. 77-82.
284. Wu, F.B., Y.Y. Xu, T. Xu, Y.Z. Wang, and S.Q. Han, *Time-resolved fluorescence immunoassay of thyroxine in serum: Immobilized antigen approach.* Analytical Biochemistry, 1999. **276**(2): p. 171-176.
285. Luppá, P.B., S. Reutemann, U. Huber, R. Hoermann, S. Poertl, S. Kraiss, S. von Bulow, and D. Neumeier, *Pre-evaluation and system optimization of the Elecsys (R) thyroid electrochemiluminescence immunoassays.* Clinical Chemistry and Laboratory Medicine, 1998. **36**(10): p. 789-796.
286. Sanchez-Carbayo, M., M. Mauri, R. Alfayate, C. Miralles, and F. Soria, *Analytical and clinical evaluation of TSH and thyroid hormones by electrochemiluminescent immunoassays.* Clinical Biochemistry, 1999. **32**(6): p. 395-403.
287. Soldin, S.J., N. Soukhova, N. Janicic, J. Jonklaas, and O.P. Soldin, *The measurement of free thyroxine by isotope dilution tandem mass spectrometry.* Clinica Chimica Acta, 2005. **358**(1-2): p. 113-118.
288. Ullman, E.F., J. Blakemore, R.K. Leute, W. Eimstad, and A. Jaklitsch, *Homogeneous Enzyme Immunoassay for Thyroxine.* Clinical Chemistry, 1975. **21**(7): p. 1011-1011.
289. Monji, N., H. Malkus, and A. Castro, *Maleimide Derivative of Hapten for Coupling to Enzyme - New Method in Enzyme Immunoassay.* Biochemical and Biophysical Research Communications, 1978. **85**(2): p. 671-677.

290. Schroeder, H.R., F.M. Yeager, R.C. Boguslaski, and P.O. Vogelhut, *Immunoassay for Serum Thyroxine Monitored by Chemi-Luminescence*. Journal of Immunological Methods, 1979. **25**(3): p. 275-282.
291. Finley, P.R., R.J. Williams, F. Griffith, and D.A. Lichti, *Adaptation of the Enzyme-Multiplied Immunoassay for Methotrexate to the Centrifugal Analyzer*. Clinical Chemistry, 1980. **26**(2): p. 341-343.
292. Arakawa, H., M. Maeda, and A. Tsuji, *Chemi-Luminescence Enzyme-Immunoassay for Thyroxine with Use of Glucose-Oxidase and a Bis(2,4,6-Trichlorophenyl)Oxalate Fluorescent Dye System*. Clinical Chemistry, 1985. **31**(3): p. 430-434.
293. Aboul-Enein, H.Y., R.I. Stefan, S. Litescu, and G.L. Radu, *Biosensor for the enantioselective analysis of the thyroid hormones (+)-3,3',5-triiodo-L-thyronine (T-3) and (+)-3,3',5,5'-tetraiodo-L-thyronine (T-4)*. Journal of Immunoassay & Immunochemistry, 2002. **23**(2): p. 181-190.
294. Stefan, R.I., J.F. van Staden, L.V. Mulaudzi, and H.Y. Aboul-Enein, *On-line simultaneous determination of S- and R-perindopril using amperometric biosensors as detectors in flow systems*. Analytica Chimica Acta, 2002. **467**(1-2): p. 189-195.
295. Driskell, J.D., J.M. Uhlenkamp, R.J. Lipert, and M.D. Porter, *Surface-enhanced Raman scattering immunoassays using a rotated capture substrate*. Analytical Chemistry, 2007. **79**(11): p. 4141-4148.

296. Jun, B.H., J.H. Kim, H. Park, J.S. Kim, K.N. Yu, S.M. Lee, H. Choi, S.Y. Kwak, Y.K. Kim, D.H. Jeong, M.H. Cho, and Y.S. Lee, *Surface-enhanced Raman spectroscopic-encoded beads for multiplex immunoassay*. *Journal of Combinatorial Chemistry*, 2007. **9**(2): p. 237-244.
297. Yakes, B.J., R.J. Lipert, J.P. Bannantine, and M.D. Porter, *Impact of protein shedding on detection of Mycobacterium avium subsp paratuberculosis by a whole-cell immunoassay incorporating surface-enhanced Raman scattering*. *Clinical and Vaccine Immunology*, 2008. **15**(2): p. 235-242.
298. Campbell, F.M., A. Ingram, P. Monaghan, J. Cooper, N. Sattar, P.D. Eckersall, and D. Graham, *SERRS immunoassay for quantitative human CRP analysis*. *Analyst*, 2008. **133**(10): p. 1355-1357.
299. He, L., M.J. Natan, and C.D. Keating, *Surface-enhanced Raman scattering: A structure specific detection method for capillary electrophoresis*. *Analytical Chemistry*, 2000. **72**(21): p. 5348-5355.
300. Driskell, J.D., S. Shanmukh, Y. Liu, S.B. Chaney, X.J. Tang, Y.P. Zhao, and R.A. Dluhy, *The use of aligned silver nanorod Arrays prepared by oblique angle deposition as surface enhanced Raman scattering substrates*. *Journal of Physical Chemistry C*, 2008. **112**(4): p. 895-901.
301. Faulds, K., W.E. Smith, D. Graham, and R.J. Lacey, *Assessment of silver and gold substrates for the detection of amphetamine sulfate by surface enhanced Raman scattering (SERS)*. *Analyst*, 2002. **127**(2): p. 282-286.

302. Stuart, D.A., C.R. Yonzon, X.Y. Zhang, O. Lyandres, N.C. Shah, M.R. Glucksberg, J.T. Walsh, and R.P. Van Duyne, *Glucose sensing using near-infrared surface-enhanced Raman spectroscopy: Gold surfaces, 10-day stability, and improved accuracy*. Analytical Chemistry, 2005. **77**(13): p. 4013-4019.
303. Trachta, G., B. Schwarze, B. Sagmuller, G. Brehm, and S. Schneider, *Combination of high-performance liquid chromatography and SERS detection applied to the analysis of drugs in human blood and urine*. Journal of Molecular Structure, 2004. **693**(1-3): p. 175-185.
304. Alvarez-Puebla, R.A., D.S. Dos Santos, and R.F. Aroca, *SERS detection of environmental pollutants in humic acid-gold nanoparticle composite materials*. Analyst, 2007. **132**(12): p. 1210-1214.
305. Zhang, X.Y., J. Zhao, A.V. Whitney, J.W. Elam, and R.P. Van Duyne, *Ultrastable substrates for surface-enhanced Raman spectroscopy: Al<sub>2</sub>O<sub>3</sub> overlayers fabricated by atomic layer deposition yield improved anthrax biomarker detection*. Journal of the American Chemical Society, 2006. **128**(31): p. 10304-10309.
306. Cabalin, L.M., A. Ruperez, and J.J. Laserna, *Flow-injection analysis and liquid chromatography: Surface-enhanced Raman spectrometry detection by using a windowless flow cell*. Analytica Chimica Acta, 1996. **318**(2): p. 203-210.
307. Graham, D., Mallinder, B. J., Smith, W. E., Angew. Chem., Int. Ed., 2000.

308. Emory, S.R. and S. Nie, *Screening and enrichment of metal nanoparticles with novel optical properties*. Journal of Physical Chemistry B, 1998. **102**(3): p. 493-497.
309. Keating, C.D., K.M. Kovalski, and M.J. Natan, *Protein : colloid conjugates for surface enhanced Raman scattering: Stability and control of protein orientation*. Journal of Physical Chemistry B, 1998. **102**(47): p. 9404-9413.
310. Zhong, C.J. and M.D. Porter, *Designing Interfaces at the Molecular-Level*. Analytical Chemistry, 1995. **67**(23): p. A709-A715.
311. Park, H.Y., R.J. Lipert, and M.D. Porter, *Single-particle Raman measurements of gold nanoparticles used in surface-enhanced Raman scattering (SERS)-based sandwich immunoassays*. Nanosensing: Materials and Devices, 2004. **5593**: p. 464-477.
312. Park, H.Y.L., R. J.; Porter, M. D., Proc. SPIE-Nanosensing: Mater. Devices, 2004. **5593**: p. 464-465.
313. Davies, C., in *The Immunoassay Handbook*, ed. D. Wild, Elsevier, San Diego, CA, 2005: p. 3-40.
314. Dong, Y.Z. and C. Shannon, *Heterogeneous immunosensing using antigen and antibody monolayers on gold surfaces with electrochemical and scanning probe detection*. Analytical Chemistry, 2000. **72**(11): p. 2371-2376.
315. Fang, F. and I. Szleifer, *Kinetics and thermodynamics of protein adsorption: A generalized molecular theoretical approach*. Biophysical Journal, 2001. **80**(6): p. 2568-2589.

316. Lu, B., M.R. Smyth, and R. OKennedy, *Oriented immobilization of antibodies and its applications in immunoassays and immunosensors*. *Analyst*, 1996. **121**(3): p. R29-R32.
317. Sakai, G., Ogata, K., Uda, T., Yamazoe, N., *A Surface Plasmon Resonance-based Immunosensor for A Highly Sensitive detection of Morphine*. *Sens. Actuators, B*, 1998. **49**: p. 5-12.
318. Henry, C.S., Dandy, D., Murphy, B.M., *Competitive Immunoassay for Simultaneous Detection of Metabolites and Proteins Using Micromosaic Patterning*. *Anal. Chem*, 2008. **80**: p. 444-450.
319. Kou, X.S., S.Z. Zhang, Z. Yang, C.K. Tsung, G.D. Stucky, L.D. Sun, J.F. Wang, and C.H. Yan, *Glutathione- and cysteine-induced transverse overgrowth on gold nanorods*. *Journal of the American Chemical Society*, 2007. **129**(20): p. 6402-6408.
320. Decher, G., *Fuzzy nanoassemblies: Toward layered polymeric multicomposites*. *Science*, 1997. **277**(5330): p. 1232-1237.
321. Khlebtsov, N.G., L.A. Trachuk, and A.G. Mel'nikov, *The effect of the size, shape, and structure of metal nanoparticles on the dependence of their optical properties on the refractive index of a disperse medium*. *Optics and Spectroscopy*, 2005. **98**(1): p. 77-83.
322. Zhao, Y.P., S. Shanmukh, Y.J. Liu, S.B. Chaney, L. Jones, R.A. Dluhy, and R.A. Tripp, *Silver nanorod arrays as high sensitive SERS substrates for viral detection*

- *art. no. 63240M*. Plasmonics: Nanoimaging, Nanofabrication, and their Applications II, 2006. **6324**: p. M3240-M3240.